Dublin City University

Doctoral Thesis

Transient Phenomena in the High Energy Sky

Author:
Carlo Romoli, M. Sc.

Supervisors:
Prof. Felix Aharonian (DIAS/MPI-K)
Dr. Andrew M. Taylor (DIAS)
Dr. Maria Chernyakova (DCU/DIAS)

A thesis submitted in fulfilment of the requirements
for the degree of Doctor of Philosophy

in the

School of Physical Sciences

September 2018

Declaration of Authorship

I hereby certify that this material, which I now submit for assessment on the programme of study leading to the award of Ph. D. is entirely my own work, that I have exercised reasonable care to ensure that the work is original, and does not to the best of my knowledge breach any law of copyright, and has not been taken from the work of others save and to the extent that such work has been cited and acknowledged within the text of my work.

Signed: _____

(Candidate) ID No.: _____

Date: _____

"E quindi uscimmo a riveder le stelle."

Dante Alighieri

Acknowledgements

Reaching the end of this journey that brought me to write this thesis, there are so many people I need to thank. First of all, I would like to thank my supervisors: Prof. Felix Aharonian for his volcanic enthusiasm and passion for gamma-ray astrophysics, Dr. Andrew Taylor for the inspiration and the incredible help he gave me, this thesis would not be here without him, Dr. Maria Chernyakova as the internal supervisor in DCU, who helped me so much in the connection with the university.

In addition I would like to thank all the members of the H.E.S.S. experiment (included former ones), in particular Dan Parsons, Dmitry Zaborov, David Sanchez, Jean-Philippe Lenain, Pol Bordas, Christian Mariaud, Thomas Murach, Nachiketa Chakraborty, Michael Zacharias, for the work done together during these years.

A big thank goes also to the high energy astrophysics group members, past and present, at the MPIK in Heidelberg for the hospitality during my frequent visits. I want to mention especially Ervin Kafexhiu for his contribution to this thesis.

These years in Dublin would not have been the same without all the people I had around me in DIAS who helped me in my professional and personal growth. Thanks to Prof. Luke Drury (also for reviewing parts of the thesis) and all the other staff members, from the professors, to the administrative and IT personnel, to the fellow students. Thanks in particular to Hillary for welcoming me on my first arrival in Dublin and for involving me in the outreach activities at the Dunsink Observatory. A warm thank you goes to all my friends inside and outside the various schools of DIAS, past and present: Martin, Rachael, Donna, Thomas, Olaf, Joan, Ruymán, Maria, Rubén, Elisa, Rui ... this list could be so long! Thanks also to my friends from my home-town and from the university years in Padova for making me feel your closeness. Thanks to Diana for her love, support and patience, especially in the last year of work.

Lastly I would like to thank my family, for their extraordinary love and support I felt in all these years. This thesis is dedicated to you.

Dublin, 30/06/2017

Edit: I add a big thank to the examiners of this thesis, whose comments improved the quality of this manuscript.

Contents

List of Figures

List of Tables

Abbreviations

AGN	**A**ctive **G**alactic **N**ucleus
CTA	**C**herenkov **T**elescope **A**rray
DSA	**D**iffusive **S**hock **A**cceleration
EBL	**E**xtragalactic **B**ackground **L**ight
EM	**E**lectro**M**agnetic
GBM	**G**amma-ray **B**urst **M**onitor
GRB	**G**amma **R**ay **B**urst
HAWC	**H**igh **A**ltitude **W**ater **C**herenkov
HESS	**H**igh **E**nergy **S**tereoscopic **S**ystem
IACT	**I**maging **A**tmospheric **C**herenkov **T**elescope
IRF	**I**nstrument **R**esponse **F**unction
LAT	**L**arge **A**rea **T**elescope
LLRT	**L**og **L**ikelihood **R**atio **T**est
MAGIC	**M**ajor **A**tmospheric **G**amma **I**maging **C**herenkov
MCMC	**M**arkov **C**hain **M**onte **C**arlo
MJD	**M**odified **J**ulian **D**ate
PSF	**P**oint **S**pread **F**unction
QED	**Q**uantum **E**lectro **D**ynamic
SED	**S**pectral **E**nergy **D**istribution
SMBH	**S**uper **M**assive **B**lack **H**ole
VHE	**V**ery **H**igh **E**nergy
VERITAS	**V**ery **E**nergetic **R**adiation **I**maging **T**elescope **A**rray **S**ystem

Alla mia famiglia

DUBLIN CITY UNIVERSITY

Abstract

Faculty of Science and Health
School of Physical Sciences

Doctor of Philosophy

Transient Phenomena in the High Energy Sky

by Carlo Romoli, M. Sc.

In this thesis I explore some of the brightest transient phenomena we observe in the high energy sky. I consider some of the observational difficulties we encounter in studying these highly variable sources, in particular the importance of the level of photon statistics, especially in the difficult region that sits between 10 and 100 GeV, where we have the overlap between the energy domain of space telescopes and the energy range more suited to ground-based Cherenkov telescopes. The specific sources I study here belong to various classes of gamma-ray emitters: Active Galactic Nuclei (AGN), compact binaries, and powerful flare events in the Sun's magnetosphere.

The first chapter provides an introduction to the field of high energy gamma-ray astronomy. There, I cover the basic gamma-ray emission mechanisms and give an overview of the sources that I have investigated as well as a description of the telescopes and instruments involved in my gamma-ray observations of these sources. The second and third chapters discuss the work I have done together with colleagues in the H.E.S.S. Collaboration to enable the delivery of the first results from phase II of H.E.S.S. for two bright AGNs and the gamma-ray binary PSR B1259-63. The fourth chapter covers my work on analysing the gamma-ray emission from solar flares in order to put constraints on hadronic models of the flare emission. The fifth chapter discusses the evidence for multiple components in the high energy spectrum of the blazar AGN called Mrk 501. The sixth chapter highlights the importance of the study of the cut-off region in bright gamma-ray sources detected by the Fermi- LAT, investigating also the possible improvements that will be brought about by the next generation of ground-based gamma-ray telescopes. Finally, the conclusions summarise my findings and explore future perspectives in the field.

Chapter 1

Introduction

In this chapter I go through the definitions and the most important concepts that served as a base for my study of high energy processes in astrophysics. I also give an overview of the field of gamma-ray astronomy, describe the type of transient sources I have focused on, and introduce the observational techniques used.

1.1 Gamma rays and cosmic rays

In the study of high energy astrophysics, gamma-ray quanta at high energies are often produced through the interaction of relativistic particles with surrounding matter or electromagnetic fields[1]. This production, therefore, first requires the acceleration of charged particles to relativistic energies. The first direct proof of the presence of cosmic particle acceleration came from the detection of high-energy ionizing particles whose intensity increased as one went up in the atmosphere. The energy spectrum of these so-called *Cosmic Rays* is shown in Figure 1.1, where we see the contributions from the various species of cosmic rays reaching the Earth. The extreme energies to which these particles can be accelerated is striking. All these relativistic particles, in the interaction with magnetic fields or interstellar material, undergo processes that involve the production of gamma rays that we can eventually observe at Earth. Furthermore, because gamma rays travel in straight lines and their direction is not influenced by magnetic fields, unlike the charged particles that make up almost all the cosmic ray flux, they can be robust probes of the sources in the cosmos where some of this acceleration takes place, offering a way to understand the "origin of the cosmic rays". This was the

[1] other possible channels can be related to dark matter, while for lower energies, there are channels related to radioactive decay

initial drive that lead to the development of gamma-ray astronomy in the 1960s, pushed forward by the prediction of detections in the late 1950s [1].

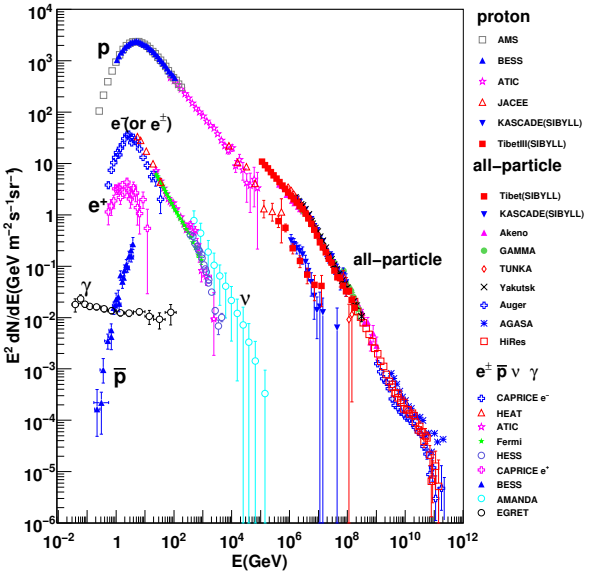

FIGURE 1.1: Cosmic ray spectrum with its components as measured at Earth. From [2] (see original for the references of the original experimental data points).

1.2 Acceleration of cosmic rays

Before talking about the characteristics of the cosmic gamma-ray radiation that can be detected on Earth, it is important to talk about how such energetic photons can be produced, stressing the point that, as will become clearer in the following sections, to produce high energy gamma rays, we first need to produce high energy cosmic rays. In this section, we thus explore our current understanding of the processes responsible for accelerating cosmic rays to the energies we see.

1.2.1 Direct acceleration

In this acceleration mechanism the particles are accelerated by extended electric fields produced in environments with rapidly rotating magnetized neutron stars or other supermassive objects [3]. While this can be a viable process to produce extremely energetic cosmic rays, either in jets of active galaxies or in the vicinity of neutron stars and black holes [e.g. 4, and references therein], the requirement of having such an extended ordered

field is a stringent one. In most of the potential cosmic ray sources, the magnetic field is more turbulent or chaotic (e.g. supernova remnants, galaxy clusters) and a different mechanism is needed to allow particles to reach very high energies. Furthermore, the direct acceleration does not seem to offer a clear explanation for observed cosmic ray spectral shape [3]. Because of these difficulties, the popularity of *Fermi* acceleration models has arisen.

1.2.2 Fermi processes

A first explanation of how it could be possible to accelerate particles in the interstellar space was put forward by Enrico Fermi in 1949 [5]. In his idea, a relativistic particle with energy E could increase its energy via scattering with massive magnetized clouds that move with speed $\sim V$ in random directions. In the limit of relativistic particles, there will be an average increase in energy given by: $\left\langle \frac{\Delta E}{E} \right\rangle = \frac{8}{3}\left(\frac{V}{c}\right)^2$ (see e.g. [6, ch. 17] for the full derivation). This type of acceleration, the *second-order* Fermi process is a case of *stochastic acceleration* and it is now one of the possibilities to explain particle acceleration in astrophysical contexts, having the advantage of being able to naturally produce a distribution of particles that would have a power-law energy spectrum like $\frac{dN}{dE} \propto E^{-\alpha}$, where the index α is related to the acceleration time scale ($\tau_{acc} = E\,dt/dE$) and the time needed to escape from the accelerating region (τ_{esc}) as $\alpha = 1 + (\tau_{acc}/\tau_{esc})$. This original idea by Enrico Fermi has now evolved. The scattering centres are no longer clouds in the interstellar medium, but turbulence in magnetic fields, which leads to *diffusion* in momentum space (some more details on the diffusion of charged particles and stochastic acceleration are given in Appendix A).

To be more effective, the acceleration process would need to be a first order mechanism in $\frac{V}{c}$. This could be achieved if the collisions with Fermi's "magnetic mirrors" could be head-on only. In the *Diffusive Shock Acceleration* (DSA) theory [7–10], the effect of diffusion in presence of strong, supersonic shocks is able to produce a change in energy proportional to $\frac{V}{c}$ (where V is the shock speed), giving rise to the *first order* Fermi acceleration. Furthermore, the final particle spectrum that can be produced by this mechanism, approaches a power-law with an index $\alpha = 2$. While this final result makes it possible for the DSA theory to explain quite well the cosmic ray spectrum [11], this model is challenged by the observation of photon spectra harder than 1.5 (as we shall see in Chapter 5). DSA is expected to be more relevant in the case of strong shocks, like the ones found in young supernovae, while a Fermi-II type acceleration is believed to be favoured in highly turbulent environments like solar flares and galaxy clusters [12, 13].

1.3 Electromagnetic interactions relevant for gamma-ray astrophysics

The energy losses, due to the various interactions cosmic rays sustain as they propagate through the Universe, are important aspects to take into account. This point is particularly relevant for the study of gamma ray emission, given that gamma rays are often emitted through these interactions. In this section I will illustrate briefly some of the most important processes related to gamma ray emission, starting with the ones tied to electromagnetic interactions. The next section will cover briefly the hadronic processes which involve the production of gamma rays.

For the production of gamma rays it is not enough to just have highly energetic particles, it is fundamental to also have a target. I will first start by describing inverse Compton scattering where a highly energetic particle interacts with a photon field. The discussion will then go through other electromagnetic emission processes like bremsstrahlung radiation, synchrotron emission and pair production. While only inverse Compton and synchrotron radiation are directly involved in the production of high and very high energy gamma rays, the other processes are still very relevant for the detection of these photons.[2]

It is important to introduce here the general notion of a *cross section*. This quantity is given by the ratio of the rate of interactions and the incoming flux of interacting particles. The comparison between the product of the cross section times the target density gives a measure of the relative importance between the various emission and absorption processes.

1.3.1 Inverse Compton

The Inverse Compton process is the "inverse" of the scattering interaction described by Compton where he observed high energy photons that scatter off low energy electrons, giving up a fraction of their energy to the recoiling electrons. In the inverse process (which in fact is the same quantum mechanical process observed by Compton), the electron instead initially carries the bulk of the energy and gives up a fraction of its energy as it "upscatters" a low energy photon[3] The final results in terms of cross section, electron

[2] In the following discussion, *cgs* units are used due to the simplification they bring when dealing with electromagnetic processes

[3] From a mathematical and physical point of view, the distinction between Compton and inverse Compton scattering is slightly artificial: in the rest-frame of the electron, the scattering is always a direct Compton scattering with the same cross section. However, to avoid confusion, the cross section is indicated with the subscript IC.

energy losses and final spectrum of the emitted radiation can be found in different textbooks and fundamental papers [see e.g. 6, 14, 15] and are derived considering the scattering in the rest frame of the charged particle and then transformed back to the laboratory rest frame. Depending on the squared centre of mass energy of the scattering[4], denoted by $x = E_{ph}E_e/(m_ec^2)^2$, we can identify two regimes: the *Thomson regime* and the *Klein-Nishina regime*. The general total interaction cross section is shown in Figure 1.2. For values of $x \ll 1$, the interaction is simply the Thomson elastic scattering between the electron and the photon with cross section: $\sigma_T = \frac{8\pi}{3}\left(\alpha_F \frac{\hbar c}{m_e c^2}\right)^2 = 6.65 \times 10^{-25}$ cm^2 (or 665 mb)[5], where α_F is the fine structure constant[6]. When the energy of the photon in the centre of mass frame starts to be comparable to the rest mass energy of the electron, so $x \gtrsim 1$, the Inverse Compton process cannot be assumed anymore to be elastic and we enter the so-called *Klein-Nishina regime* (KN). In this regime, the cross section diminishes with the squared centre of mass energy, approaching

$$\sigma_{KN} \approx \frac{3}{8}\frac{1}{x}\left(\ln 2x + \frac{1}{2}\right)\sigma_T \tag{1.1}$$

(see e.g. [17] for a full approximated expression).

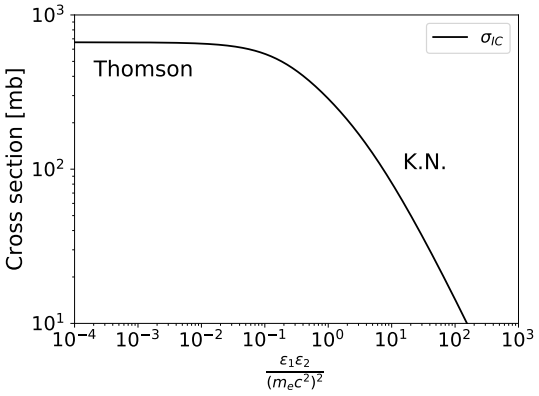

FIGURE 1.2: Total Inverse Compton cross section as a function of the product of the energy of the two particles divided by $\left(m_ec^2\right)^2$. At low energies, the value tends to the Thomson cross section, while for higher interaction energies, we enter the Klein-Nishina regime.

Due to relativistic kinematic arguments (see e.g. [14] for more details on the following paragraph), the energy of the scattered photon E_{ph_1} will take values between the initial

[4]The square of the centre of mass energy is identified with the Lorentz invariant Mandelstam variable s which corresponds to the square of the invariant mass of the initial or final particles $s = (p_1 + p_2)^2$ in case of two initial particles, where p is the four-momentum of the particle. When the electron rest mass can be neglected $p_1 = E_1$ and $p_2 = E_2$ so $s = 2E_1E_2(1 - \cos\theta)$, where θ is the scattering angle (see e.g. [16, ch. 1]).

[5]The barn (b) and its multiple are units often used to measure cross sections in particle physics: 1 b=10^{-24} cm^2

[6]The fine structure constant can be written as $\alpha_F = e^2/(\hbar c) \sim 1/137$

energy of the photon E_{ph_0} and the maximum allowed energy by the interaction, that is $\frac{b}{b+1}E_{e_0}$ where $E_{e_0} = \gamma m_e c^2$ is the initial energy of the electron and $b = 4E_{ph_0}E_{e_0}/(m_e c^2)^2$ is related to the squared centre of mass energy if collisions are head-on (the maximum amount of energy available for the system). So we can write:

$$E_{ph_0} \leq E_{ph_1} \leq \frac{b}{b+1}E_{e_0} \tag{1.2}$$

Now, the Thomson regime can be identified as the one where $b \ll 1$, while the extreme KN regime is for $b \gg 1$. In the first case, the expression (1.2) reduces to $E_{ph_0} \leq E_{ph_1} \leq bE_{e_0}$ obtaining a maximum energy $E_{ph_{max}} = 4\gamma_e^2 E_{ph_0}$ with an average energy $\langle E_{ph_1} \rangle \approx \frac{1}{3}E_{ph_{max}} = \frac{4}{3}\gamma_e^2 E_{ph_0}$. From this, it follows that:

$$\left(-\frac{dE}{dt}\right)_{IC} = \frac{dN_{ph}}{dt}\langle E_{ph_1}\rangle = \frac{4}{3}\gamma_e^2 \sigma_T c U_{rad} \tag{1.3}$$

taking into account the definition of the cross section, $dN_{ph}/dt = c\sigma_T U_{rad}/E_{ph_0}$ (assuming a monochromatic photon field with energy E_{ph_0})[7] where U_{rad} is the energy density of the target radiation field. This argument can be extended further and it can be shown that if we start with a power-law distribution of electrons following $E_e dN_e/dE_e = N_0 \left(E_e/E_{0_e}\right)^{-p+1}$, the resulting spectrum of the emitted photons will be "stretched" by the presence of the γ_e^2 factor in the energy of the upscattered photon expression, so that the final number of photon distribution at energy E_{ph} will follow $E_{ph}dN_{ph}/dE_{ph} = N_{0_{ph}}\left(E_{ph}/E_{0_{ph}}\right)^{\frac{-p+1}{2}}$ [6, ch. 9].

In the KN case, the photon comes away with an increasing fraction of the electron's energy and $b/(b+1) \to 1$ as $s \to \infty$. As visible from the spectrum of the scattered photons in Figure 1.3 (from the formulae in [18]), the peak is close to the maximum allowed energy. Assuming again a monochromatic photon field, because of the immediate transfer of almost all the energy of the particle to the photon during a single interaction and the dependence of the cross section on the energy of the electron, the emitted power becomes almost independent of the energy of the incoming high-energy electron[8]. Thus, if the distribution of electrons is a power-law, the spectrum of the photons will also be a power-law with the same index [18]. Note that when the electron-photon scattering is in the KN regime, the change in electron energy after a scattering is not small. Treating the energy loss of the electron as a continuous process, e.g. as in a Kompaneets equation treatment, is thus *not* a good approximation.

[7] The expression in equation (1.3) is valid only in the ultra-relativistic case, the proper expression has a factor β_e that has been neglected here [6, ch. 9]

[8] Given (1.1), the actual dependence is logarithmic in the energy of the particle.

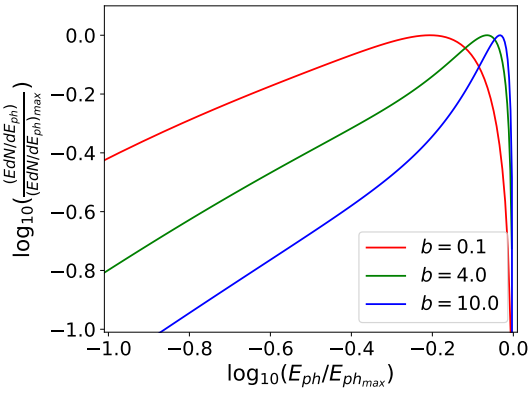

FIGURE 1.3: IC scattered photon distribution (as EdN/dE) with the energy of the scattered photon normalized to its maximum value. Different curves are for different values of b, where $b = (4E_{ph_0}\gamma_e)/(m_e c^2)$ relates to the maximum energy available in the centre of mass reference frame. For high values of b the spectrum of the scattered photons peaks close to the maximum allowed energy.

1.3.2 Bremsstrahlung

Bremsstrahlung ("braking") radiation relates to the emission of low energy gamma-rays (below 100 MeV) and is a fundamental process for the detection of gamma-ray photons as well as an energy loss process for energetic particles. The radiation is produced by the interaction between a charged particle and the Coulomb field of a target nucleus with charge Ze. For the derivation of the interaction cross section and the spectrum of the emitted radiation, the process can be seen as the scattering between the charged particles and a distribution of virtual photons associated with the other charged particle, in the so called *Weizsäcker-Williams* approximation [19, 20]. The expressions for the full differential cross section can be found in [21, section 15.4], [14], with more details in [22, ch. 25] and it diverges as $1/E_{ph}$ for low energy photons. However, if we limit ourselves to the emission of photons with at least half of the energy of the electron (the ones that contribute most to the energy losses [23]), the total cross section can be seen as in Figure 1.4, represented in units of $Z^2\alpha_F\sigma_T$.

The distribution of the emitted photons, especially for primary high energy electrons, is found to be $dN_{ph}/dE_{ph} \propto E_{ph}^{-1}$ (flat if represented in EdN/dE) with a cut-off at $E_{ph} = \gamma m_e c^2$, as shown in Figure 1.5. Using this result, as demonstrated in [24, sect. 18.3], it can easily be shown that the photon spectrum obtained from a power-law distribution of electrons, defined by the index p (as $dN_e/dE \propto E^{-p}$), will have the same index p, so the slope of the Bremsstrahlung emission spectrum tells us the slope of the underlying electron energy distribution.

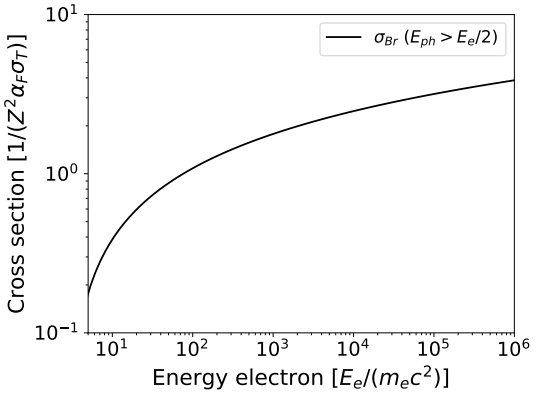

FIGURE 1.4: Total Bremsstrahlung cross section for the emission of photons with energy $E_{ph} > E_e$. The cross-section is shown in units of $Z^2\alpha_F\sigma_T$.

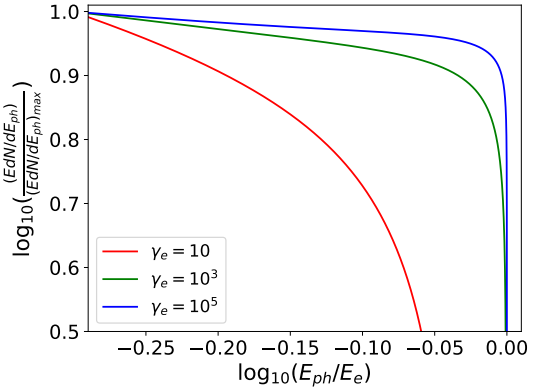

FIGURE 1.5: Spectrum of Bremsstrahlung emission for different energies of the primary electron, shown as EdN/dE as a function of the ratio between the energy of the emitted photon and the energy of the primary electron.

From the integral of the energy emission spectrum ($E_{ph}\frac{dN_{ph}}{dE_{ph}}$), we obtain the result that the radiative loss rate of the electron via Bremsstrahlung is proportional to the electron's energy. This result is important because it implies that the cooling time is a constant and depends only on the density of the target material. The expression for the energy losses of the electron also implies that, when the particle moves through a medium, $\frac{dE}{dx} \propto E$ so it is possible to define X_0 as the distance over which the electron energy becomes $\frac{1}{e}$ of its initial energy. Because of the dependence on the target, X_0 is usually given in units of [g cm^{-2}] so that the actual distance can be obtained by dividing by the density of the material.

1.3.3 Magnetic bremsstrahlung - Synchrotron radiation

Synchrotron radiation is emitted when charged particles interact with a magnetic field of intensity B. The net effect is a change in the trajectory of the particle, which will radiate in response. A full description of the process can be found for example in [6, ch. 8] or [15, ch. 6] and here only the main points are highlighted. On a general level, the results depend on the energy of the charged particle, the intensity of the magnetic field and the *pitch angle* between the trajectory of the particle and the direction of the magnetic field. Taking the example of a single electron gyrating in magnetic field, it can be shown that the radiated power is:

$$\left(\frac{dE_e}{dt}\right)_{syn} = 2\sigma_T c \beta_e^2 \gamma_e^2 U_B \sin^2\vartheta \tag{1.4}$$

where U_B is the energy density of the magnetic field and ϑ the pitch angle. (1.4) can be easily integrated over ϑ obtaining:

$$\left(\frac{dE_e}{dt}\right)_{syn} = \frac{4}{3}\sigma_T c \beta_e^2 \gamma_e^2 U_B \tag{1.5}$$

It is worth noting the similarities between the emitted power by synchrotron radiation in (1.5) and by Inverse Compton processes (in the Thomson regime expressed by (1.3)). This argument is however valid only when the synchrotron radiation can be treated in the "classical" regime. To be able to neglect quantum effects, the energy of the particle and the magnetic field must satisfy $\frac{E_e}{m_e c^2}\frac{B}{B_{cr}} \ll 1$ [25], where $B_{cr} = \frac{m_e^2 c^3}{e\hbar} = 4.4 \times 10^{13}$ Gauss[9].

The fundamental quantity, which dictates the shape of the spectrum is the so called *characteristic energy* E_C expressed as [15, ch. 6][10]

$$E_C = \frac{3}{2}\gamma_e^2 \frac{eB\hbar}{m_e c}\sin\vartheta = \frac{3}{2}\gamma_e^2 \hbar\omega_B \sin\vartheta \tag{1.6}$$

where $\omega_B = \frac{eB}{m_e c}$ is the gyro-frequency. The derivation of the actual spectrum of the synchrotron radiation can be obtained through a complete solution of the electrodynamic equations [15, ch. 6], but the general energy dependency of the spectrum can also be obtained using the Weizsäcker-Williams approximation as described in [27] where,

[9] Synchrotron emission could be seen as IC emission in Thomson regime if we think of the magnetic filed as a virtual photon field where photons have energy $E_{ph} = m_e c^2 \left(\frac{B}{B_{cr}}\right)$. For a description of the effect in strong magnetic fields, when $\frac{B}{B_{cr}} \gtrsim 1$, refer to [26]

[10] In [15] the expression is given in terms of angular frequency, here to maintain a consistent notation, I have multiplied by $\hbar$ to present Eq. 1.6 in terms of energy.

considering again the electron surrounded by the cloud of virtual photons, they will be emitted in the form of radiation when the projected distance on the line of sight between the electron and the photon becomes greater than a wavelength λ. The path covered by the electron while this happens is called *formation length*. In the case of synchrotron emission, the electron proceeds along a circular path with velocity v, so the formation length L_0 is $R\theta_0 = vt_0$, where θ_0 is the angle subtended by the arc. The virtual photon travels instead on a straight line such that $ct_0 = 2R\sin(\theta_0/2) + \lambda$ with $2R\sin(\theta_0/2)$ being the length of the chord (the virtual photon path). With these considerations, the final spectrum above and below the characteristic energy can be expressed as [27]:

$$E_{ph}\frac{dN}{dE_{ph}}(E_{ph}) \propto \frac{e^2}{\gamma_e^2}\begin{cases} E_{ph}^{1/3} & E \ll E_C \\ E_{ph}^{1/2}\exp\left(-\frac{E_{ph}}{E_C}\right) & E \gtrsim E_C \end{cases} \tag{1.7}$$

The actual expression is indeed more complex and requires the use of Bessel functions. Following [14], it can be written as:

$$E_{ph}\frac{dN}{dE_{ph}}(E_{ph}) = \frac{\sqrt{3}e^2B}{m_ec^2}\frac{E_{ph}}{E_C}\int_{\frac{E_{ph}}{E_C}}^{\infty} d\xi K_{5/3}(\xi) \tag{1.8}$$

where the last part is often shown as $F(x) = x\int_x^\infty d\xi K_{5/3}(\xi)$. The pitch-angle averaged expression for (1.8) involves the use of the function $G(x) = x\int_x^\infty d\xi\sqrt{1-\frac{x^2}{\xi^2}}K_{5/3}(\xi)$ [28, Appendix D] instead of $F(x)$. Because of the similarities with the Inverse Compton process in the Thomson regime, the same arguments regarding the energy dependence for the cooling time and energy losses hold for synchrotron radiation.

In the astrophysical context, synchrotron radiation and inverse Compton emission can go hand-in-hand through the process called *Synchrotron Self Compton* (SSC). In this scenario, the same population of electrons responsible for the synchrotron photons also Compton upscatters the synchrotron photons towards gamma-ray energies. This scenario has been commonly used to explain the TeV emission from blazar active galactic nuclei (see section 1.5.2).

1.3.4 Pair production

The pair production process is an important absorption phenomenon, not only for its role in the detection of gamma rays, but also for the part it plays in reducing the flux of very high energy gamma rays from astrophysical sources. In this process, a photon is converted into an electron-positron pair. Depending on the actual constituents of the interaction, we can have: pair production in matter, pair production in a photon field

and pair production in a magnetic field[11] (see [23] for an overview of all the processes). A key feature is that this process has a natural threshold and can only happen if the centre of mass energy of the interaction is large enough to produce a pair of particles (so $E_{th} = 1.022$ MeV). Pair production in matter and photon fields is described briefly below.

In matter, the total cross section of the process depends on the atomic number Z of the material and for high energies saturates to σ_{pair} [23]:

$$\sigma_{pair} = \frac{7}{9} \times \frac{3}{2\pi} \sigma_T \alpha_F Z \left(Z+1\right) \frac{\ln\left(183 Z^{1/3}\right)}{1 + 0.12 \left(Z/82\right)^2} \tag{1.9}$$

The actual shape of the cross section can be seen in Figure 1.12. The expression for the cross section is similar to that of Bremsstrahlung. This aspect is important for the development of electromagnetic showers of particles in materials (see section 1.7.1), where Bremsstrahlung and pair production processes run in parallel to sustain the shower[12].

The cross section for the photon-photon pair production process $\gamma\gamma \rightarrow e^+e^-$ can be written, for the case of an isotropic photon field, as [25]:

$$\begin{aligned} \sigma_{\gamma\gamma} = \frac{3}{2s_0^2} \sigma_T \Bigg[\left(s_0 + \frac{1}{2} \ln s_0 - \frac{1}{6} + \frac{1}{2s_0} \right) \ln\left(\sqrt{s_0} + \sqrt{s_0 - 1}\right) \\ - \left(s_0 + \frac{4}{9} - \frac{1}{9s_0} \right) \sqrt{1 - \frac{1}{s_0}} \Bigg] \end{aligned} \tag{1.10}$$

where s_0 represents the product of the energy of the two colliding photons in units of $m_e c^2$. This function starts to rise after the threshold of the process and peaks at a value of s_0 close to 4, where it reaches a value 20% of the Thomson cross section. At higher energies, the relative importance of the finite electron mass decreases, and both Inverse Compton and pair production cross sections behave in similar way (see Figure 1.6). Given the large peak cross section value of this last process, in the presence of dense photon fields, like those found in the vicinity of the central engines of AGN or around massive stars in gamma-ray binaries, it can strongly reduce the flux of high energy gamma rays that are able to escape from the source to propagate through the Universe. The general case of photon pair production has an obvious dependence on $(1 - \cos\theta)$, where θ is the scattering angle between the photons (more details can be found in e.g. [29]) and this effect can become particularly important in presence of highly anisotropic environments.

[11] the last two processes can only be allowed through the interaction of virtual leptons and require higher order QED

[12] There is slight difference of a factor $\frac{9}{7}$ in the interaction length. The interaction length λ can be found as the reciprocal of the product of the cross section and the number density n of targets, so $\lambda = \frac{1}{\sigma n}$

1.3.5 Summary of interaction cross sections

To summarize the main concepts regarding the electromagnetic interaction processes, Table 1.1 lists characteristic quantities for the photon scattering and emission processes discussed above, while Table 1.2 compares the cross sections of the two photon pair production (absorption) processes. In Figure 1.6, we show the angle-averaged cross section for Compton scattering and photon-photon pair production $\gamma\gamma \to e^+e^-$ assuming isotropic incoming particle distributions. These two cross sections are a reference for the other values reported in Tables 1.1 and 1.2

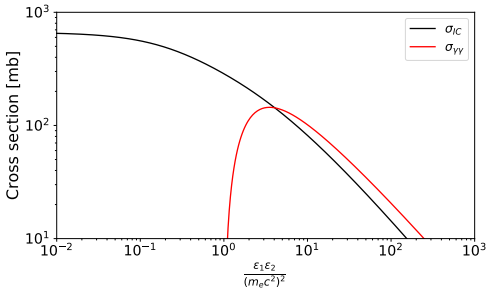

FIGURE 1.6: Cross section for Inverse Compton scattering (as in Figure 1.2) and isotropic $\gamma\gamma$ pair production as a function of the product of the energy of the two interacting particles (in units of m_ec^2).

TABLE 1.1: Summary table for Electromagnetic emission processes. For the Compton cross section expression in the K.N. regime, $x = \frac{E_{ph}E_e}{(m_ec^2)^2} \gg 1$. The synchrotron radiation entries are valid only in the limit $\gamma_e \frac{B}{B_{cr}} \ll 1$.

Process	Cross section	Characteristic Energy	Target density	dE/dt
Th. IC	σ_T	$\sim \gamma_e^2 E_{ph}$	$\frac{U_{rad}}{E_{ph}}$	$\propto E_e^2$
K.N. IC	$\sim \frac{3}{8}\frac{1}{x}(\ln 4x)\,\sigma_T$	$\sim \gamma_e m_e c^2$	$\frac{U_{rad}}{E_{ph}}$	$\sim$ const.
Bremss.	$\propto Z^2\alpha_F\sigma_T$	$\sim \gamma_e m_e c^2$	n	$\propto E_e$
Synch.	σ_T	$\sim \gamma_e^2 m_e c^2 \frac{B}{B_{cr}}$	$\frac{U_B}{m_ec^2 B/B_{cr}}$	$\propto E_e^2$

TABLE 1.2: Cross sections for the photon pair production processes γN and isotropic (angle-averaged) $\gamma\gamma$.

Process	Cross section
$\gamma N \to e^+e^-$	$\propto \frac{7}{9} Z^2\alpha_F\sigma_T$
$\gamma\gamma \to e^+e^-$	$\sim 0.2\sigma_T$ (at peak)

1.4 Hadronic interactions relevant for gamma-ray astrophysics

Charged hadrons are also subject to the previously described electromagnetic interactions but, due to the proportionality of the cross sections with the inverse of the square of the mass of the particle, in the same conditions, their contribution through these channels is much lower[13]. However, hadrons also have an internal structure that opens other emission channels through strong interactions [see e.g. 6, 25].

The main hadronic processes that can lead to the production of high energy photons are pp or $p\gamma$ interactions (with p standing for proton). The total cross sections for these interactions are shown in Figure 1.7 as a function of the invariant mass $\sqrt{s}$.[14] One of the most probable results of this type of interactions is the production of the various flavours of pions (π mesons: $\pi^{\pm}$ and π^0). While the charged ones decay through weak interactions $\pi^+ \rightarrow \mu^+\nu_\mu$ and $\pi^- \rightarrow \mu^-\bar{\nu}_\mu$ into muons (that subsequently will decay into $e^{\pm}$) and neutrinos, the neutral pion decays electromagnetically into two photons[15]: $\pi^0 \rightarrow 2\gamma$.

It is also worth mentioning the hadronic processes involving neutrons. While these might not be important for the detection of gamma rays, they can be fundamental in the physical environment of the source and in the cosmic ray production. Photo-hadronic interaction can have the effect of charge exchange with transformation of protons in neutrons and vice-versa via the channels $p\gamma \rightarrow n + e^+ + \nu_e$ and $n\gamma \rightarrow p + e^- + \bar{\nu}_e$. In sources like blazars (see subsection 1.5.2), highly energetic neutrons could escape the acceleration site with negligible losses and decay into ultra-high energy protons only in the intergalactic medium [30]. In neutron star physics, *urca*-processes [31] are particularly relevant where a nucleus with mass A and atomic number Z can capture an electron in the process $(A, Z) + e^- \rightarrow (A, Z-1) + \nu_e$, or beta-decay as $(A, Z-1) \rightarrow (A, Z) + e^- + \bar{\nu}_e$. Neutrinos are produced in each of these exchanges and they can leave the source making *urca*-processes an effective way to cool neutron stars [see e.g. 32].

The production of π particles is a threshold process that requires the proton to have a kinetic energy of at least the pion mass[16], for the $p\gamma$ process, while for a pp interaction, the threshold kinetic energy increases to around two pion masses [25]. Once the neutral

[13] as an example the mass of the proton $m_p = 1836 m_e$, so its inverse Compton cross section will be $\sim 3 \times 10^6$ times lower than that of an electron

[14] The variable s is the Mandelstam variable, the square of the centre of mass energy used before for the other interactions.

[15] with a branching ratio of $\sim 99\%$. The second most probable decay channel is $\pi^0 \rightarrow \gamma e^+ e^-$.

[16] The mass of the charged pion is ~ 140 MeV, while the neutral pion mass is ~ 135 MeV. The actual value of the energy threshold is $E_{th} \approx 145$ MeV [25]

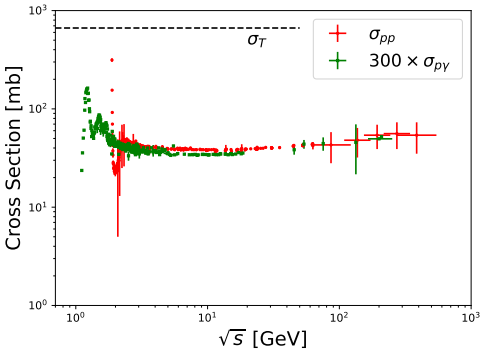

FIGURE 1.7: Experimental pp and pγ interaction cross sections as a function of $\sqrt{s}$. The pγ cross section has been multiplied by 300 for visibility purposes. The black dashed horizontal line indicates the value of the Thomson cross section. The experimental data are from [33].

pions are produced, their decay time is 10^{-17} seconds and the resulting gamma ray spectrum results in a broad bump centred at energy $E \sim 70$ MeV (half the rest mass of the pion). The cross section for this type of process is not an easy analytical expression and it is often presented as a parametrization of experimental data, e.g., as done by Kafexhiu et al. [34] for the gamma ray production cross section from pion decay in pp interactions using the most recent data. Another way is to use numerical codes like PYTHIA [35].

1.5 Variable astrophysical gamma-ray emitters

After this description of some of the principal mechanisms for the production of gamma rays, it is now time to look at some of the astrophysical sources where these mechanisms are in operation. The discussion here will start with those furthest away and then move to more nearby ones.

1.5.1 Gamma-ray bursts

Gamma-ray bursts (GRBs) are high energy transients lasting up to $\sim$ 100 seconds, placed at cosmological distances in the Universe. Their name relates to the fact that the peak of their SED sits in the energy range between 100 keV and 1 MeV. Their discovery dates back to the late 1960s thanks to the Vela satellites. The Vela satellites were developed for the detection of gamma ray emission from nuclear tests during the Cold War, but found signals of extraterrestrial origin. However their existence was only made public at the beginning of the 1970s [36, 37]. A big leap forward came in the

1990s, especially with the gamma-ray observations of the *Burst And Transient Source Experiment* (BATSE) onboard the *Compton Gamma Ray Observatory* (CGRO), and *BeppoSAX*, an X-ray satellite named in honour of the Italian astrophysicist Giuseppe Occhialini.

Through the BATSE observations, it was possible to determine the isotropic distribution of GRBs in the sky while BeppoSAX gave the high localization accuracy needed to start follow-up observations with optical telescopes [38] and finally prove the cosmological origin of GRBs [36]. In addition, an important result obtained by BATSE was the discovery of a bimodality in the distribution of the burst durations, which lead to the division of the population of GRBs into two classes: *short* (with duration < 2 seconds) and *long* bursts (with duration > 2 seconds) [39].

Since GRBs are at cosmological distances, if they were to emit isotropically, the inferred amount of energy released by these events is large, as high as 10^{51-54} erg [40]. The bimodality in the duration distribution has been explained by the presence of two classes of progenitors: short bursts as the result of the merging process of 2 neutron stars collapsing into a black hole; long bursts associated to the direct collapse of a massive star into a black hole [40] [17].

Even though some of these sources have been detected by the *Fermi*-LAT with photons at energies above 10 GeV, we are still lacking a detection from ground based gamma-ray experiments.

1.5.2 Active Galactic Nuclei

As the name suggests, Active Galactic Nuclei[18] are a class of galaxies characterized by a very intense luminosity from their central region which cannot be explained only by the presence of standard stellar processes. Historically, these objects have been subdivided in a multitude of different classes according to their appearance [see e.g. 6, ch. 18].

At optical wavelengths, the brightest AGNs were misidentified as stars because of their point-like appearance. Later on, with the development of radio astronomy, they started to be called *Quasar* (for *Quasi-stellar radio source*). These radio observations also discriminated between radio quiet and radio loud active galaxies, with the radio loud ones being only $\sim 10\%$ as abundant as the radio quiet ones and the distinction between

[17] During the revision of this manuscript, the LIGO Collaboration announced the gravitational wave detection of the inspiral and merger of two neutron stars which appeared to coincide with a short GRB event, supporting our current understanding of the short GRB class [41].

[18] using the acronym, the plural often becomes AGNs

these two classes is still under debate [42]. However, in this thesis I will focus more on the radio loud population. For this type of source (but more generally for radio galaxies), there is now an established *Unified Model* [43]. This paradigm, illustrated in Figure 1.8a, explains the general idea that we have for the mechanism powering the emission of these AGNs and the different phenomenological sub-classes that arise from the different angles between the line of sight and the axis of the system. Similar non-symmetric models have also been proposed for radio-quiet AGNs, with obscuring material that can prevent the direct observation of the central regions for edge-on observers [44]. In the following paragraphs I go through the basic points of this unified model.

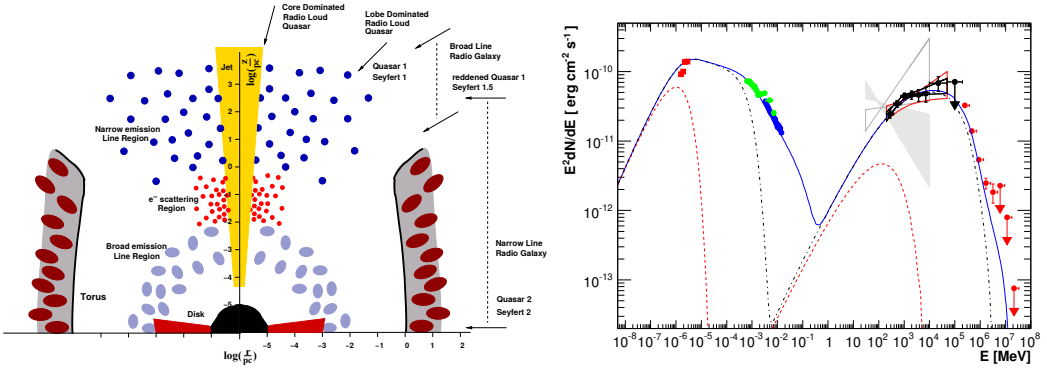

(A) Sketch of the central engine of an AGN

(B) Broad-band SED of the blazar PKS 2155−304

FIGURE 1.8: The *left* panel shows a schematic representation of the unified model for radio loud AGNs (from [45]). At the centre there is the SMBH with its accretion disc. Within the first parsec there is also the so called *Broad Line Region*. Further out, the *Narrow Line Region* and the dusty obscuring torus. Along the axis of the system, $\sim 10\%$ of the time we have a powerful relativistic jet that can reach scales $\sim 10^5$ pc. The *right* panel shows the broadband SED of the blazar object PKS 2155−304 (taken from [46]), where we can see the characteristic double-peaked multi-wavelength spectrum of radio loud sources.

The current explanation for the extreme power emitted by these sources (which, in the assumption of isotropic emission, can reach values up to 10^{49} erg/s) is that it comes from the accretion onto the super-massive black hole (SMBH) at the centre of the galaxy. The accretion process leads to the conversion of gravitational energy to radiation. The masses of these black holes can range from 10^6 to 10^9 $M_\odot$. Within the first parsec from the central black hole would reside i) the accretion disc which is typically bright at ultraviolet wavelengths, ii) a corona of hot electrons that emit hard X-rays, and iii) clouds of dense gas (n up to 10^{10} cm^{-3}), responsible for broad line emission (Doppler broadening with speeds of 10^4 km/s), hence called the *Broad Line Region*. Outside this zone, extending for $\sim$ 100 pc, the gas clouds are less dense and slower (typically $n \sim 10^4$ cm^{-3} with speeds lower than 10^3 km/s) forming the so called *Narrow Line*

Region. The view of the inner region of the system is blocked for an edge-on observer by a "dusty torus" (or a similar type of structure luminous at infrared wavelengths) which occupies radii between ∼1 and 10 pc. The accretion process leads also to the formation of a jet that can extend up to Mpc scales. Further details on the unified model can be found in e.g. [43, 47] while [48] offers a critical view on the open questions regarding the inner structure of AGNs.

The obscuring material from the torus is "optically thick" to optical, ultraviolet, and even sometimes X-ray radiation, effectively blocking our view of the inner (< 100 pc) region of the AGN system if oriented in such a way that the observer's line of sight passes through the torus. We call "Type 2" AGN those which only show narrow emission lines from the NLR in the optical and usually with evidence of significant X-ray absorption in X-rays. If the torus does not block our line of sight to the black hole, then we see a "Type 1" AGN, where in the optical we see a higher ionization state, significantly Doppler broadened line emission plus the continuum emission from the accretion disk, and in X-rays, we often see relativistically broadened X-ray iron emission lines (which in principle can be used to probe the space-time geometry near the black hole) [see e.g. 6, ch. 18]. Specifically for radio loud sources, the relation between the jet Doppler boosting factor and the angle between the jet axis and the observer's line of sight (which we call θ_{view}) gives a further angular dependence. Radio loud AGNs seen along the jet axis show compact, relativistically boosted "core dominated" emission, while those seen at larger angles are dominated by the unbeamed radio lobe emission which comes from the termination shock of the jet outflow as it hits the intergalactic medium (see [43, App. A] for more details on the angular dependence of the relativistic beaming). This last point can be expressed using the core-dominance parameter $R(\theta_{view}) = L_{radio,core}/L_{radio,lobe}$) [49, 50] which is a continuous quantity, in contrast to the changes in optical AGN properties with viewing angle, which typically behave much more like a step-function: there is not much change in the optical properties until the view of the central region is blocked by the dusty torus which is typically transparent at radio wavelengths.

To summarize, "Type 1" sources are those that offer a direct view of the central region, with the characteristic signature of broad lines in the optical spectrum, coming from the BLR. "Type 2" AGNs are instead those where the view of the central engine is obscured and only the emission from the NLR is detectable. According to the unified model, the geometrical effect of the orientation of the system with respect to the line of sight of the observer is the explanation of this distinction.

A further, more physically motivated classification is found instead for the radio loud

class of AGNs. Radio galaxies are believed to be fundamentally divided in two populations, the Fanaroff-Riley galaxies of the first (FR I) and second (FR II) type[19]. FR Is are typically less luminous and their radio morphology show a bright central core from which jets depart in opposite directions, ending in faint radio lobes. FR IIs are instead typically more powerful and have bright radio lobes with hotspots, connected to the central region by bright, collimated jets. Furthermore, FR II galaxies present a stronger line emission at optical and infrared wavelengths, pointing toward the presence of more material near the central engine. More details on this classification can be found in e.g. [43, 52].

1.5.2.1 Blazars

The class of objects more relevant for gamma-ray astrophysics (roughly 70% of the high galactic-latitude sources in the latest *Fermi*-LAT catalogue) is the *blazar* class [53]. In the paradigm of the unified model, these are the AGNs where the relativistic jet forms a small angle with the line of sight. Because of relativistic beaming, their jet luminosity is highly boosted [43, appendix A]. Figure 1.8b shows the SED of the object PKS 2155−304 highlighting the intense non-thermal radiation we detect in these objects. The first peak of the spectrum is believed to be due to synchrotron emission from relativistic electrons, while the nature of the high-energy peak is still debated: leptonic models explain it as inverse Compton upscattering of either the synchrotron photon field produced by the jet electrons (SSC, Synchrotron Self Compton) or of the ambient, "external" photon field (EC, External Compton) produced by sources outside the jet; hadronic models point instead towards a proton synchrotron scenario (see e.g. [54]). Two distinct sub-classes can be identified in the blazar group: the *BL Lac*[20] and the *FSRQ* class[21]. The main differences between the two is that BL Lacs tend to have a featureless optical spectrum[22] and are considered to be the aligned version of FR I radio galaxies (the ones with low power and compact central region). The FSRQs are instead typically brighter objects, with a more structured optical spectrum and are believed to be the beamed version of FR II radio galaxies [43].

[19] From the name of the scientists that proposed this classification [51]. The denomination FR I and FR II is not related to Type 1 and Type 2 AGNs and should not be confused with each other. As initially defined, both classes of FR galaxies are Type 2 AGNs, given that their jets are lying almost perpendicular to the line of sight [43]

[20] from the archetypal source BL Lacertae

[21] FSRQ stands for *Flat Spectrum Radio Quasars*.

[22] A lack of emission or absorption lines in the spectrum that in most cases also prevents a redshift determination.

1.5.2.2 Extragalactic Background Light

An important process that affects cosmologically distant sources is the absorption of gamma rays via gamma-gamma pair production (see section 1.3.4). The presence of UV, optical and infrared photons coming from starlight and dust emission pervades the Universe and can start pair-production processes via the interaction with the high energy photons coming from cosmologically distant sources. This generates an absorption feature in the spectrum that depends on the energy E of the photon and on the redshift z, so that:

$$I(E) = I_0 \exp\left(-\tau(E, z)\right)$$

where I_0 is the intrinsic emission and τ is the absorption parameter. In Figure 1.9, τ is given for different redshift values, with its energy dependence following the model of Franceschini et al. [55]. From these considerations we can see the detection of these sources over a large energy range and at different redshifts is fundamental to improve our knowledge of the EBL through studying the intrinsic spectra of blazars [56]. See e.g. [57] for a review.

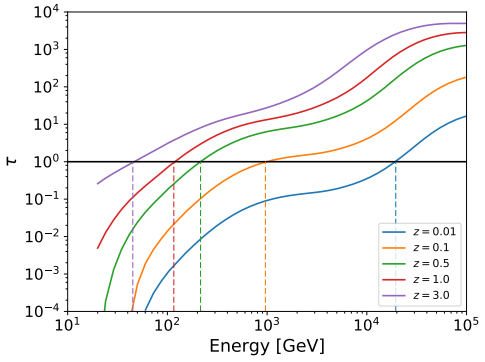

FIGURE 1.9: Value of the absorption parameter τ due photon-photon pair production on the EBL, according to the model of Franceschini et al. [55]. The black horizontal line highlights the value of $\tau = 1$, while the coloured dashed lines show the energy at which the absorption parameter has the value of 1 for each of the redshifts shown.

1.5.3 Binaries

Moving from extra-galactic objects to something more local, I now consider those objects that can be grouped under the name of (high mass) gamma-ray binaries. These are binary systems that have a massive star as one element of the couple and that are peculiar in the sense that they emit most of their energy as gamma rays (E $>$ 1 MeV) (see e.g. [58] for a review). At the time of writing, the number of gamma-ray binaries

that have been detected at very high energy by ground based telescopes is 7 (5 canonical ones plus 2 recent discoveries) and all are reported in Table 1.3[23].

TABLE 1.3: Known gamma-ray binaries as of April 2017. Data taken from [59–61]. The source HESS J1832−093 is still a tentative association [60]. All the objects are galactic, except the binary LMC P3 that was found in the Large Magellanic Cloud [61].

Name	Components	Orbital Period	Distance periastron and apoastron
PSR B1259−63	O9.5Ve + pulsar	3.4 years	$d_p = 0.9$ AU; $d_a = 13.4$ AU
LS 5039	O6.5V + ?	3.9 days	$d_p = 0.09$ AU; $d_a = 0.19$ AU
LS I +61°303	B0Ve + ?	26.5 days	$d_p = 0.19$ AU; $d_a = 0.64$ AU
HESS J0632+057	B0Vpe + ?	315 days	$d_p = 0.40$ AU; $d_a = 4.35$ AU
1FGL J1018.6−5856	O6V + ?	16.6 days	$d_p = (0.35)$ AU; $d_a = (0.35)$ AU
? HESS J1832−093	NA	NA	NA
LMC P3	O5III + pulsar?	10.3 days	NA

Together with the massive star, the companion of these binary systems is a compact object (neutron star or black hole). The illustration shown in Figure 1.10 gives an idea of the two possible scenarios behind the gamma-ray emission from high-mass compact binaries: the *pulsar wind-stellar wind* interaction and the *micro-quasar* model. In the first case the very high energy emission is due to the interaction between the two winds, while in the latter there is an accretion process (analoguous to the process in AGNs) that leads to the formation of a jet and then the emission of gamma rays from the jet.

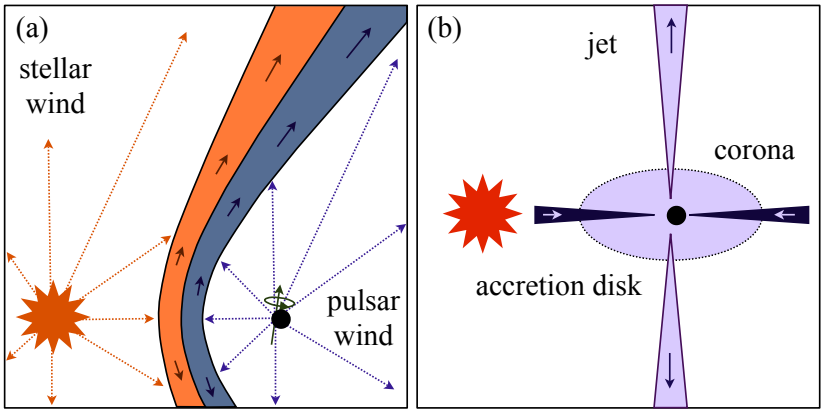

FIGURE 1.10: Main classes for the high-mass gamma-ray binaries. The left panel (a), represents the model of collision between pulsar and stellar winds, while the right panel (b) represents the micro-quasar scenario. The image has been adapted from [58]

A characteristic of these objects is their variability modulated by the orbital period of the system (which can range from years to days) with cases in which we can recognize very regular patterns (like PSR B1259−63 and LS 5039)[62]. However, of these 7 binaries

[23]The TeV detection of LMC P3 by the H.E.S.S. Collaboration was just recently announced at the conference *SN 1987A, 30 years later* by N. Komin `https://iaus331.lupm.in2p3.fr/programme/scientific-programme/` (url accessed on the 6/6/2017)

that have been detected so far at energies above 100 GeV, only PSR B1259−63 has a clear identification of the compact object (being a millisecond pulsar). For the other members of this class, it is still under debate whether we are dealing with a black hole or a pulsar and there is still not enough evidence to discriminate between the two cases [58].

In Chapter 3, I will focus on the recent developments on the study of PSR B1259−63, through the observation of the source during the 2014 periastron passage.

1.5.4 Solar Flares

Moving closer to our planet, our star is also a gamma ray emitter. It is a modest one, but due to its proximity, it delivers some of the brightest events in the gamma-ray sky. During the impulsive phase of major solar flares, it is able to release up to 10^{32} erg on time-scales of the order of hundreds of seconds[24]. This energy is believed to be coming from events involving magnetic reconnection in the solar corona and involves various channels with the production of both thermal and non-thermal radiation, indicating the presence of particle acceleration during these events [63, 64, for a review]. The time evolution of a solar flare can be divided into four phases, starting with an initial pre-flare phase, where we see a build-up of the emission seen in soft X-rays and extreme ultra-violet. After the pre-flare, there is the so-called impulsive phase: a sudden release of most of the energy, associated with a brightening in the hard X-rays component of the spectrum (linked to the emission from a non-thermal population of electrons). This is followed by a flash phase in which also the thermal component associated with the emission in the soft X-rays peaks, and finally a decay phase, where the overall emission brightness declines at all energies [64]. The gamma-ray emission is found to be highly correlated with the hard X-ray component in the impulsive phase, but has the characteristic of being more extended in time, lasting up to several hours after the end of the first energy release and showing an exponentially decaying light-curve [e.g. 65, 66]. This long-lasting high-energy emission could be explained by high energy particles accelerated in the corona that move down into the denser chromosphere emitting gamma rays, or with the presence of continuous acceleration due to other mechanisms like shocks associated with coronal mass ejections and stochastic acceleration in closed loops by the effect of plasma turbulences [67, 68].

[24] for reference the solar luminosity is $L_\odot = 4 \times 10^{33}$ erg/s

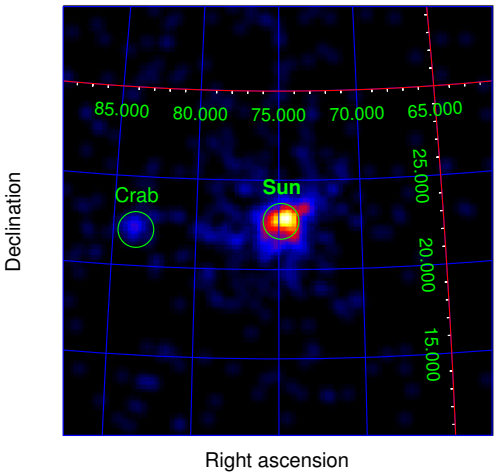

FIGURE 1.11: Solar flare SF20110607 seen by the *Fermi*-LAT with $E > 60$ MeV over an integration time of 36 minutes (count map smoothed with a 3°-gaussian filter). The average position of the Sun is indicated by a green circle with radius of 1 degree. On the left side is visible the faint emission from the Crab pulsar (whose position is also indicated by a green circle of 1-degree radius), which is one of the brightest persistent sources in the gamma-ray sky. This event is one of the flares re-analysed in Chapter 4 using the new *Fermi*-LAT analysis tools.

The observation of the Sun in gamma rays shows a spectrum with various components [see e.g. 69, table 3.1]: gamma-ray lines due to the de-excitation of atomic nuclei dominant in an energy range between 100 keV and 10 MeV, lines from the annihilation of positrons (at 511 keV) and the neutron capture line (at 2.223 MeV); continuous emission from relativistic bremsstrahlung of electrons and positrons, accelerated in the plasma or produced in hadronic processes like the decay of charged pions; and a broad peak due to the decay of neutral pions more important for energies ≥ 100 MeV. In Figure 1.11 an image of the solar flare SF20110607 is shown as seen by *Fermi*-LAT at energies above 60 MeV.

One interesting aspect in the observation of the Sun's gamma-ray emission is that with the Sun being so close, it is possible to detect not only the photon emission from a flare event, but also the associated generation of cosmic rays by using other instruments located near the Earth. These results show that the primary spectrum, for kinetic energies greater than ~ 10 MeV per nucleon is a soft power-law with index $\alpha \sim 4$ [70].

A deeper look into the analysis of bright solar flares is reported in Chapter 4, where updated cross sections for hadronic processes are used to infer the original spectrum of the particles accelerated in a sample of recent Solar Flares.

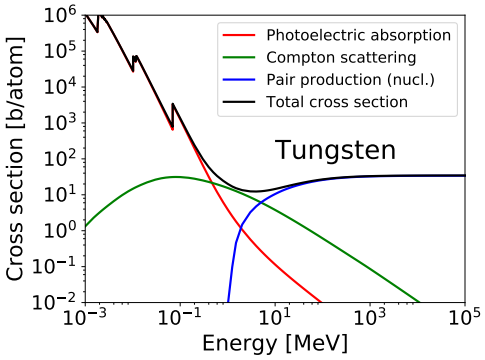

FIGURE 1.12: Cross section for the photoelectric, Compton and pair production processes between gamma-ray photons and Tungsten, in units of barns per atom. The curves were obtained using the NIST online database [71].

1.6 The detection of gamma rays from space

Gamma-ray photons have three fundamental ways of interacting with matter. As shown in Figure 1.12, at the lowest energy, the dominant process is the photoelectric effect in which the photon energy is absorbed by the atom and it is used to free electrons from the material. The second process, which becomes important at energies around 100 keV and remains relevant up to $\sim$ 10 MeV, is Compton scattering (the regular version of the process presented in 1.3.1). In this case the photon and electron scatter in the material with an exchange of energy and momentum between the two particles so that the photon is re-emitted with a lower energy and a different direction with respect to the original one. As soon as the energy of the photon becomes greater than the 1.022 MeV (twice the electron rest-mass energy), the photon, in the Coulomb field of the atom, can transform into a pair electron-positron. The last two processes are the most relevant when dealing with the detection of gamma rays above the MeV scale. While Compton scattering has little dependence on the atomic number of the element, both the photoelectric and the pair production depend strongly on the atomic number of the element the photon is interacting with: the dependence of the photoelectric effect cross section with the atomic number of the material Z can be roughly expressed as $\sigma \propto \frac{Z^n}{E^3}$ where n has a value between 4 and 5 and E is the photon energy [see e.g. 22, ch. 21]; the pair production process depends instead on Z^2 (as seen in 1.3.4) and it is particularly relevant for space missions dedicated to the detection of gamma rays. Because the atmosphere is opaque to gamma rays, the detection must happen in space[25].

[25]In the following section it is shown how this is not entirely true and it is still possible to build ground based gamma-ray telescopes.

1.6.1 The *Fermi* satellite

The state of the art in terms of space gamma-ray telescopes is represented by the *Fermi* satellite (known as GLAST before launch and renamed in honour of Enrico Fermi afterwards). It was launched in June, 2008 becoming fully operational at the beginning of August, 2008 after a calibration period. It operates in a low orbit, at a height of $\sim$ 560 km above the surface of the planet. The scientific operations are carried out by two instruments: the GBM (*Gamma-ray Burst Monitor*) and the LAT (*Large Area Telescope*). The structure of the satellite is shown in Figure 1.13.

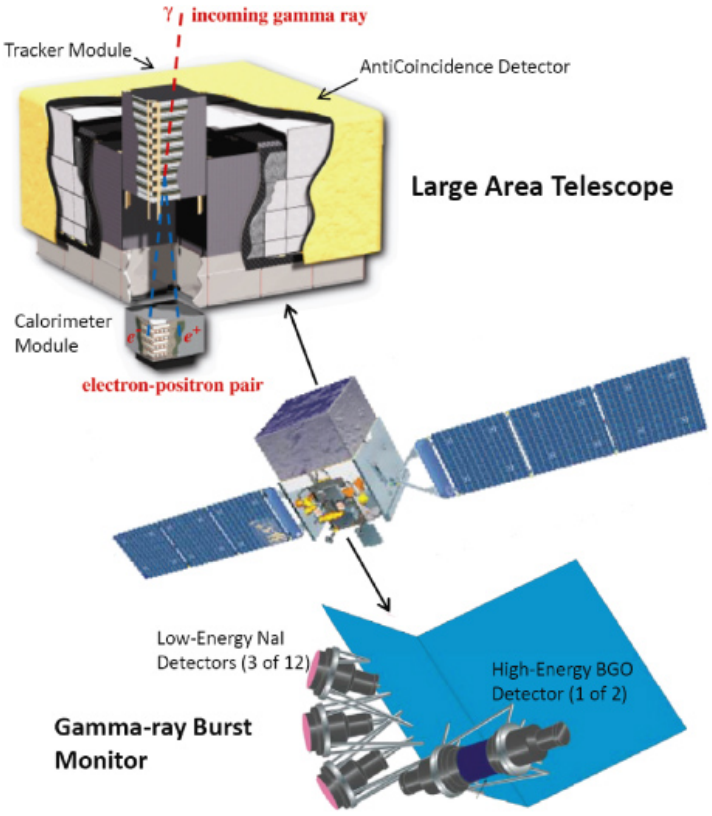

FIGURE 1.13: Schematic view of the *Fermi* satellite illustrating the position and structure of the two instrument on-board the spacecraft. The *top* half of the figure shows the Large Area Telescope with an open view of all its parts. The *bottom* half shows the position and the arrangement of the two types of scintillators making the Gamma-ray Burst Monitor. Illustration taken from [72].

The GBM is a set of two types of scintillation detectors in which the entire energy of the photon is absorbed by the material producing a characteristic scintillation light that can be read by photomultipliers. As the name of the instrument implies, the GBM was born to detect and characterize Gamma-Ray Bursts, with a fast response and a final accuracy in the location of the burst of roughly 3 degrees[26].

[26] `https://fermi.gsfc.nasa.gov/science/instruments/table1-2.html` accessed on 2017-06-12

The main instrument on-board the *Fermi* satellite is however the Large Area Telescope. The nominal energy range covers several orders of magnitude, from 20 MeV to several hundreds of GeV, where its sensitivity is affected more by the low photon fluxes at these energies than by the detection difficulties[27].

The LAT has a large field of view of roughly 2.4 sr. In standard operation conditions, it is able to scan almost the entire sky in within 2 orbits ($\sim$ 3 hours). The instrument structure is illustrated in detail in the top corner of Figure 1.13 and described in [73, 74]. The core of the detector is the tracking mechanism, composed of a 4×4 matrix of towers. Each tower is made of layers of Silicon strip detectors and Tungsten. The operating principle of the instrument is based on the pair production mechanisms: the Tungsten foils facilitate the conversion of the gamma-ray photon into an electron-positron pair which can then be easily tracked by the Silicon strip detector [75, for the technical description].

At the bottom of the instrument there is a segmented calorimeter of crystals of CsI, a dense material whose role is to measure the total energy of the detected photon via the full absorption of the resulting pair [76, for the technical description]. To this structure is associated a segmented anti-coincidence shield (or anti-coincidence detector - ACD), a layer of plastic scintillator which screens the instrument from the huge cosmic ray background, whose flux is several thousands of times higher than the gamma-ray flux at these energies [77, for the technical description].

Since the launch of the satellite, advancements in the reconstruction techniques have enables several LAT performance improvements over the years, embodied by the latest set of *Instrument Response Functions* (IRFs), which give the tools required to translate the data collected by the satellite into meaningful physical quantities. At the time of writing, the latest IRFs are coded in the *Pass 8 Release 2* (P8R2) version, released in June 2015[28]. The graphs in Figure 1.14 summarise the basic characteristics of the LAT instrument, showing the effective area, the point spread function and the energy resolution. Because of the way the instrument is constructed, with vertical tracking towers, the optimal reconstruction is achieved in the case where the angle between the incoming photon and the axis of the instrument is at the minimum (Fig. 1.14b). As visible from the plots in Figure 1.14a, the instrument can count on an effective area of roughly 1 m^2. An important aspect that strongly affects the Point Spread Function (PSF) shown in Figure 1.14c, is the multiple scattering of the particles within the tracker,

[27] For general analysis purposes the recommended energy range goes from 100 MeV to 500 GeV, where the systematic issues in the reconstruction of the photon parameters are better constrained.

[28] `https://fermi.gsfc.nasa.gov/ssc/data/analysis/documentation/Pass8_usage.html` accessed on 14-06-2017

especially at lower energies. This effect degrades the accuracy in the reconstruction of the incoming direction of the photon, leading to an uncertainty of up to 6° for a 100 MeV photon. At the highest energies, multiple scattering is not an issue and the angular uncertainty in the reconstruction approaches $\sim 0.1°$. The energy resolution (in Fig. 1.14d) is instead one of the strong points of the instrument, with the best performance around 10 GeV with a value close to 5%.

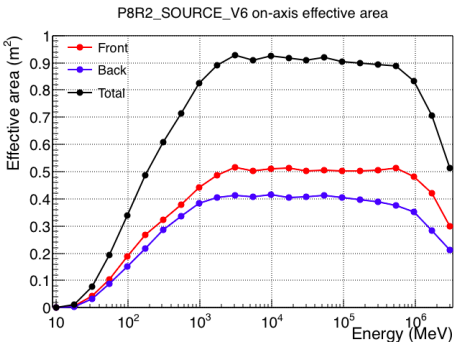

(A) On axis effective area

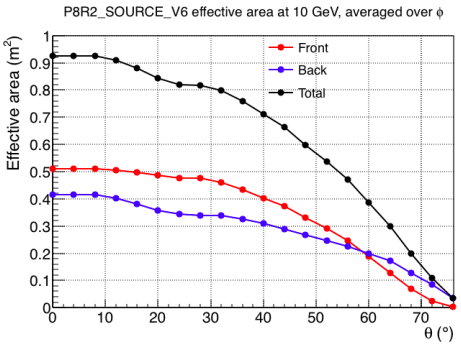

(B) Dependence of effective area at 10 GeV with incident angle

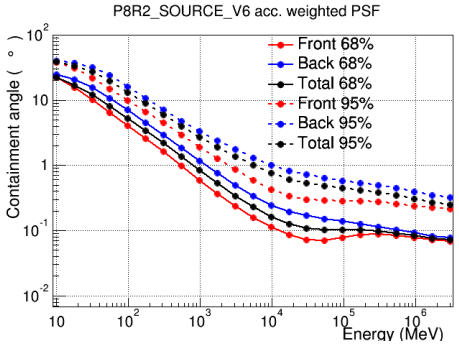

(C) On axis point spread function

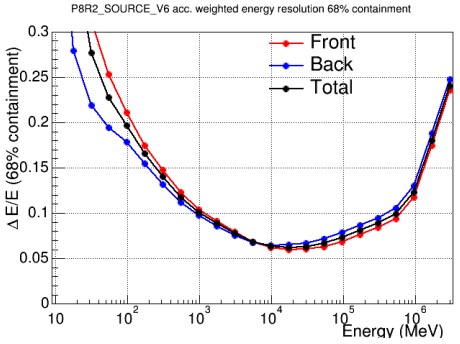

(D) On axis energy resolution

FIGURE 1.14: LAT Instrument Response Functions

1.6.2 The future of gamma-ray astronomy from space

The future for the detection of gamma rays from space is still not well defined. The *Fermi* satellite will remain in operation at least until 2018, but there is not yet a clear successor to carry out observations in the GeV range. However, there are several relevant projects in the study phase [78].

One of the most relevant is *e-ASTROGAM*[29] (enhanced ASTROGAM) described in [79], which is a project proposed for the M5 call of the European Space Agency. Its role would be to cover the almost unexplored energy range between 300 keV and 3 GeV with

[29] `http://eastrogam.iaps.inaf.it/index.html` accessed 14-07-2017

a much better sensitivity compared to what was achieved by COMPTEL. If accepted, it will become operational some time in the 2030s. Another interesting instrument, that would be the successor of the *Fermi*-LAT in terms of energy range, is *GAMMA-400*[30] [80], a Russian-led project to build an instrument sensitive to gamma rays in the range 0.1 GeV - 3 TeV. The launch would happen in 2021 or later.

In the light of what will be described in the next subsection regarding ground based observatories, it will be important to maintain a gamma-ray telescope with a wide field of view in order to carry out monitoring over a wide energy range.

1.7 Detection of gamma rays from ground

At higher gamma-ray energies, it is possible to use the atmosphere itself as a detector and build ground based gamma-ray telescopes. In general, the interaction of a high-energy particle with the atmosphere generates a shower of particles: when the secondary particles produced in the first interaction have enough energy to interact again with the atmosphere material. This process is sustained until the average energy per particle is below the threshold to produce new ones. Depending on the nature of the primary particle, two types of shower can be generated: *electromagnetic* ones, if the primary is a photon or a lepton, driven only by electromagnetic interactions, and *hadronic* showers if the primary particle is a proton or an atomic nucleus. This last type of shower also involves strong and weak interactions.

1.7.1 Electromagnetic and Hadronic showers

For electromagnetic showers, the two most relevant processes are the pair-production interaction of the photon, and bremsstrahlung radiation from electrons (or positrons). A schematic view of the process is illustrated in Figure 1.15, taken from [81][31]. The figure shows the basic principles of the development of the shower and its longitudinal evolution. The key point to understand is that the generation of new particles proceeds up to the point where the amount of energy in each particle falls below the threshold where the amount of energy lost by the electrons via ionization equals the one that is radiated away via bremsstrahlung, the so called *critical energy* E_c (for electrons in air $E_c = 86$ MeV) [82]. At this point the number of particles in the shower decreases and

[30] `http://gamma400.lebedev.ru/indexeng.html` accessed 14-07-2017

[31] As highlighted by the author of [81], the scheme in Figure 1.15a does not take into account the slight difference between the radiation length of the electron (X_0) and the mean free path for pair production of the photon which is $\frac{9}{7}X_0$, and assumes an equal repartition of the energy to all particles.

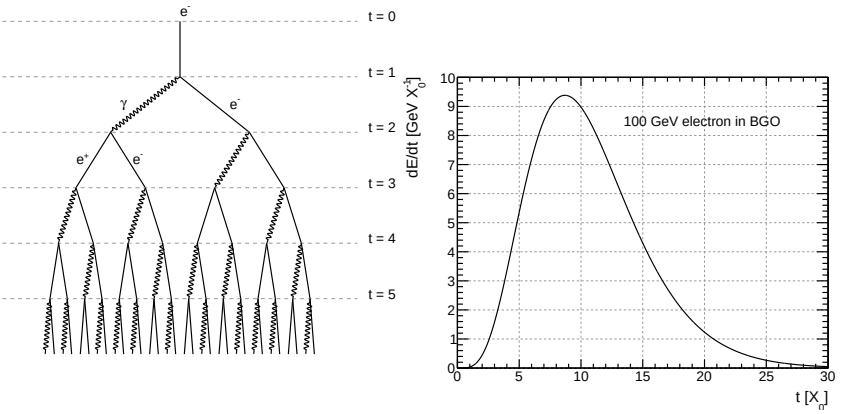

(A) Schematic view of an electromagnetic shower

(B) Longitudinal shower development

FIGURE 1.15: Schematic view of an electromagnetic shower and its longitudinal development. Using a simplified approach, the right panel shows the increase in the number of particles at each interaction. The left panel is instead an illustration of the number of particles per interaction length of a shower initiated by a 100 GeV electron passing through a crystal of BGO. The images are taken from [81].

the shower dies off as illustrated by the plot in Figure 1.15b. The position of the shower maximum scales logarithmically with the initial energy E_0 of the primary particle and is located approximately at [81, 82]:

$$X_{max} = X_0 \ln\left(\frac{E_0}{E_c}\right) \pm \frac{1}{2}$$

where X_0 is the radiation length of the electron (introduced in section 1.3.2). The position is in terms of radiation lengths and the last sign is $+$ for photons and $-$ for electrons. As an example, a 1 TeV photon will have its shower maximum after roughly 10 radiation lengths.

When the primary particle is a hadron, together with the electromagnetic component, strong and weak interactions come into play. For this reason, the study of this type of shower is much more complicated and relies heavily on numerical simulations. One important point is that hadronic showers tend to be broader and more structured, showing signatures of multiple components, like showers that end up with the decays of charged pions and consequent production of muons, and pure electromagnetic components from the decay of neutral pions. This difference in shape and structure is what is generally used to recognize the primary particle associated with a determined shower [see e.g. 82, for a review].

1.7.2 Cherenkov radiation

Together with the production of showers, there is another ingredient that makes the detection of gamma-rays possible in some types of ground based telescopes. This ingredient is the production of *Cherenkov radiation*. This phenomenon is linked to the type of electromagnetic radiation that is emitted when a particle crosses a medium with a speed that is greater than the speed of the light in that material, given by $v = c/n$ where n is the refraction index. Because the light cannot keep up with the speed of the particle, a conical wavefront is produced, the direction of which has an angle θ_c relative the direction of the particle, where $\cos(\theta_c) = \frac{c}{vn}$ as shown in Figure 1.16.

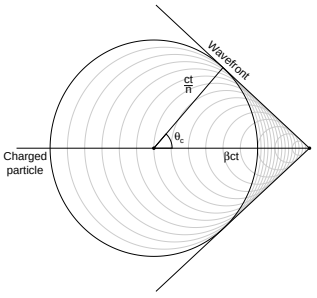

FIGURE 1.16: Cherenkov radiation pattern, taken from [81].

This radiation is emitted in a pulse that lasts a few nanoseconds and results in a spectrum that peaks at blue wavelengths. Even though the amount of energy radiated by this mechanism is not very significant in terms of the total energy budget of the radiating particle, it is this radiation that offers another possibility of detecting gamma rays from ground based telescopes. To provide an example of this last point (taken from [83, ch. 7]), a 300 GeV photon produces a shower maximum at a height of $\sim$ 10 km. The Cherenkov photons produced will propagate downwards in a cone with an opening angle of $\sim 2^\circ$ degrees which results in a *light pool* of $\sim 10^2$ m in radius. The size of the light pool on the ground is very relevant because this is what makes it possible for ground based telescopes to reach the very high collection areas (of the order of 10^5 - 10^6 m^2) required to overcome the low photon number fluxes at very high energies. The possibility to detect the light from the showers depends as well on the amount of atmosphere they have to cross: for a source viewed at a large zenith angle (the angle between the sky vertical and the pointing position of the telescope) the Cherenkov photons are subject to more atmospheric absorption and this effect hinders the detection of fainter showers from low-energy photons, increasing the energy threshold of the telescope.

Depending on the exact technique that is used, we can divide the ground based gamma-ray telescopes into two main families: non-imaging (or air shower) detectors and imaging

telescopes. The first type directly detects the shower particles arriving on ground, while the second type detects the Cherenkov light produced by the particles in the atmosphere.

1.7.3 Non-imaging telescopes

This type of instrument bases its detection technique on counting the shower particles that reach the ground. For this reason, even if they are positioned at high altitude, their low energy threshold is at few TeVs because they can only detect secondary particles from showers that are energetic enough to leave a reasonable signal on the ground. The actual detection can be done either with scintillator plates placed on the ground that directly detect the shower particles or with water tanks equipped with photomultipliers that detect the Cherenkov radiation produced by the particles as they move through the water. An example of this latter type of telescope is the *High Altitude Water Cherenkov* (HAWC) Gamma-Ray Observatory[32] shown in Figure 1.17a. This is a non-imaging system made up of an array of 300 water tanks situated at an altitude of 4100 m above the sea level [see e.g. 84]. The discrimination between the overwhelming hadronic cosmic ray flux and gamma rays is done by looking at the shower "deposition pattern" in the array, which is more irregular for hadrons due to the presence of muon signals in the detector [84]. The sensitivity of the HAWC array is shown in Figure 1.17b. It has a high energy threshold and reaches its best performances at $E \sim 10$ TeV. However, it has a large field of view (~ 2 sr) and a duty cycle close to 100%, which makes it a perfect instrument for the monitoring of bright Very High Energy emitters, especially transients such as nearby GRBs.

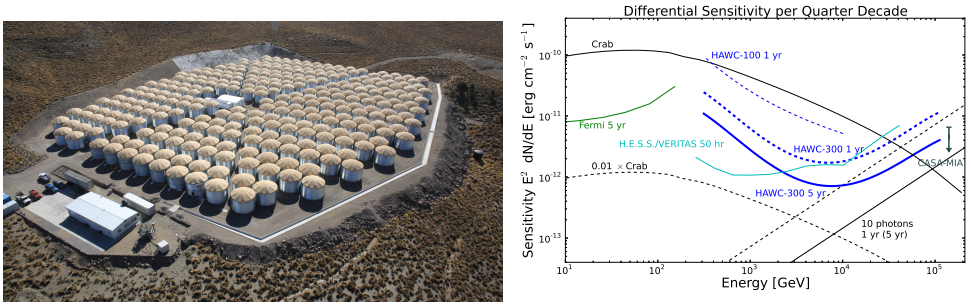

(A) HAWC Observatory (B) HAWC Sensitivity

FIGURE 1.17: The water tanks that make up the HAWC telescope in Mexico (left panel, Credits: the HAWC Observatory) and the official sensitivity for the HAWC telescope compared with other existing gamma-ray telescopes (right panel) from [85].

[32] `http://www.hawc-observatory.org/` accessed on 14-04-2017

1.7.4 Imaging telescopes, the case of H.E.S.S.

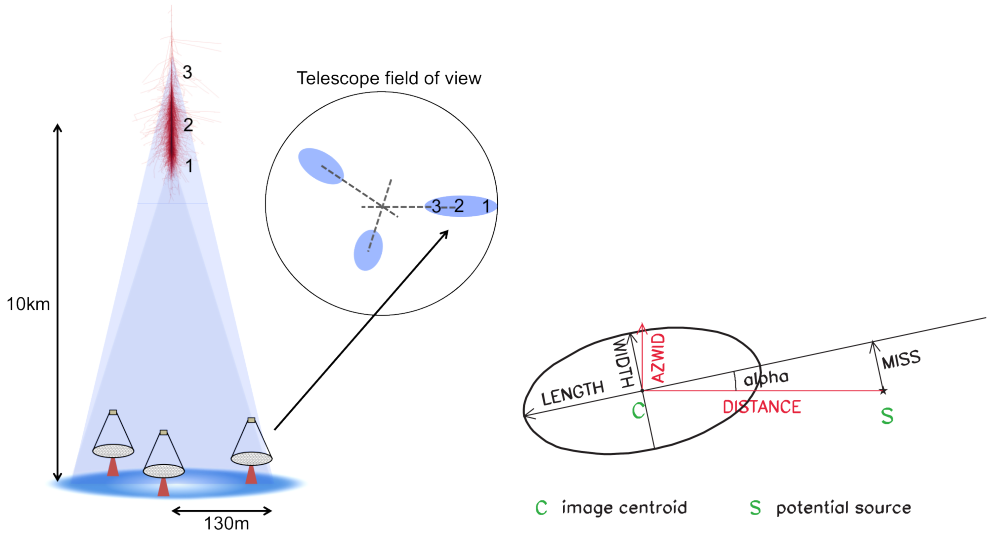

(A) Detection of Cherenkov showers (B) Hillas parameters

FIGURE 1.18: *Left* panel: Schematic view of the detection of a Cherenkov shower (from [86]). *Right* panel: Hillas parameters to characterize Cherenkov shower images (from [87]).

This class of detectors, called *Imaging Atmospheric Cherenkov Telescopes* (IACTs), is based on the detection of the Cherenkov light produced in the atmosphere by the relativistic particles produced in an air shower. A schematic view of the process is shown in Figure 1.18. The Cherenkov photons are collected by the large reflective surfaces and focused on a fine-pixellated camera where the shower image is reconstructed. The first very successful method to derive the characteristics of the incoming photon is to parametrize the elliptical images on the telescope camera through the so-called *Hillas parameters*, shown in Figure 1.18b [88]. From numerical simulations it is possible to derive the range of values that the image of gamma rays showers can have. Applying cuts on these parameters allows the rejection of showers produced by hadrons (see e.g. [87] for a good review of instruments and methods in Very High Energy astrophysics).

One of the most successful, currently operating IACT systems is the H.E.S.S. array[33]. The instrument is illustrated in Figure 1.19. It is built at an altitude of 1800 metres above the sea level in the Khomas Highlands in Namibia. It consists of 4 telescopes with a diameter of $\sim$ 12 m positioned at the vertex of a square with the side of 120 m, while in the centre, since 2012, there is a much larger telescope ($\sim$ 28 m diameter) to lower the energy threshold of the array[34].

[33]The other two main imaging arrays are the MAGIC telescope, made of two 17 m mirrors in the Canary Islands and the VERITAS array composed of four 12 m telescopes in the Arizona desert.

[34]These small telescopes are called CT1,CT2,CT3, and CT4 and they constituted the H.E.S.S. phase I array. The central telescope is known as CT5 and its installation started the phase II of the experiment.

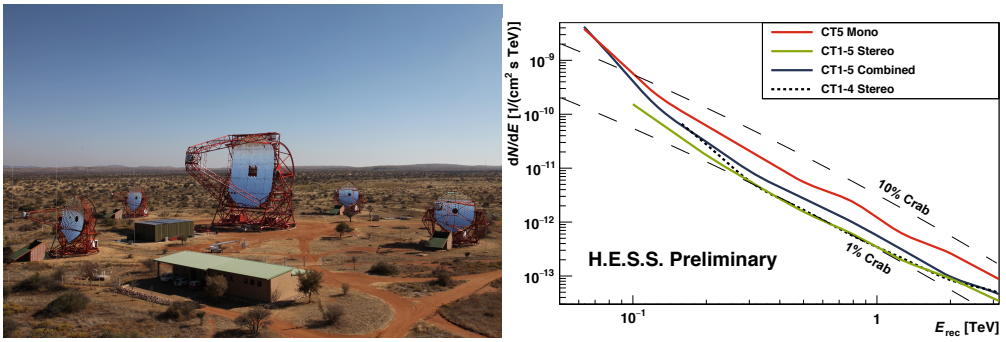

(A) H.E.S.S. array (B) H.E.S.S. Sensitivity

FIGURE 1.19: On the left panel, the H.E.S.S. Array with the four 12-meter reflectors on the corners and the 28-meter telescope in the centre (Credits: H.E.S.S. Collaboration, Clementina Medina). The right panel shows the sensitivity curves below 1 TeV for the various configurations of the H.E.S.S. array in its phase II set-up after 50 hours of observation, from [89].

Because of the hybrid composition of the array, there are four possible ways of analysing the data:

- H.E.S.S. phase I - This operation mode involves only the original 4 small telescopes, disregarding the CT5 triggers.
- MONO - using only triggers from the central telescope (CT5). This mode allows one to reach the lowest energy threshold thanks to the large area of the reflective surface that enables the collection of the weak signal from low energy Cherenkov showers. While the MONO operation mode has been successful in having an energy threshold below 100 GeV (especially for transient sources like AGN flares as shown at the end of Chapter 6), its performance has been limited by systematic effects due to the large impact of the Night Sky Background (NSB) and the lack of stereoscopic information to suppress the background signal coming mostly from muons.
- STEREO - using triggers from any two telescope in the array. In this operation mode, the energy threshold is slightly higher than for MONO, due to the fact that the small telescopes cannot detect the light from the low energy showers. However, there is still an improvement compared to the old phase I configuration because with the help of CT5 faint signals from the small telescopes at low energies can be used. This consequently leads to an improvement in the sensitivity of the array at $\sim$ 100 GeV energies, as shown from Figure 1.19b.
- COMBINED - this mode combines the MONO reconstruction (for photons detected only by CT5) and the STEREO reconstruction as soon as there are a

coincidence trigger in the array. The advantage of this mode is that provides an analysis of the entire energy range within a single reconstruction chain.

Technical characteristics of the two types of telescopes are reported in Table 1.4.

TABLE 1.4: Technical specifications for the two types of telescopes in the H.E.S.S. array. The values of angular and energy resolutions are for reconstruction methods more advanced than the basic Hillas analysis (see e.g. [90, 91] and their updated versions for H.E.S.S. II [89, 92]).

	H.E.S.S. I	H.E.S.S. II (CT5)
Mirror size [m^2]	108	614
Camera pixels	960	2048
Pixel size [°]	0.16	0.067
Field of view [°]	5	3.2
Angular resolution [°]	~ 0.06	~ 0.15
Energy resolution	$\sim 10\%$	$\sim 25\%$

1.7.5 The future of ground-based gamma-ray astronomy

Ground based gamma-ray astronomy is about to enter an exciting phase brought about by powerful new telescopes already under construction or in program. On the side of the imaging technique, the biggest project in the near future is undoubtedly the *Cherenkov Telescope Array* (discussed in more detail in Appendix B). It consists of two sites: one in the Canary Islands and one in the Atacama desert of Chile. Each site will have a variety of telescopes to cover an energy range going from ~ 20 GeV up to hundreds of TeV with a sensitivity 10 times better than present instruments. One of the goals of the future ground based instruments is to reduce the energy threshold. Beside CTA, we will also have the MACE (*Major Atmospheric Cherenkov Experiment*) telescope, currently under construction in Northern India, in the Ladakh region, at an altitude of 4270 m above sea level. (When finished, it will become the highest altitude imaging Cherenkov telescope). With a mirror diameter of 21 m, it is envisaged to have an energy threshold of ~ 38 GeV [93]. However, given the lesson learnt with H.E.S.S. and CT5, the presence of a single reflector might be a limiting factor for this instrument.

On the air shower side, some of the main projects are HiSCORE (*Hundred Square km Cosmic ORigin Explorer*) and LHAASO (*Large High Altitude Air Shower Observatory*) [78]. The first is an air shower detector aiming for the highest energies, from tens of TeVs to the PeV scale. The detection technique will use the precise timing of the Cherenkov light from the shower (see e.g. [94] for details). LHAASO will be built in the Sichuan region in China at an altitude of 4410 metres above sea level. It will be a hybrid, wide

aperture observatory, in the energy range between sub-TeV and hundreds of TeV (see e.g. [95] for details).

These future instruments will significantly enhance our sensitivity to gamma-ray phenomena over a very extended energy range, going from tens of GeV to the PeV energy.

Chapter 2

A lower threshold for existing observatories

In this chapter, I illustrate the work I have done in a team within the H.E.S.S. Collaboration. I focus on the challenges and the benefits that came from the installation of a 28-m telescope in the middle of the previous H.E.S.S. array. With the installation of this telescope, the H.E.S.S. experiment was able to lower its energy threshold below 100 GeV. Here I am reporting the first results on AGNs using only data from CT5, published in [96]. For the material presented here, for which I was responsible for the cross-check analysis of the H.E.S.S. and (partially) the Fermi-LAT results, I would like to thank in particular D. Zaborov (the lead author of [96] and main analyst) as well as the other corresponding authors for this publication: A. Taylor (task leader and EBL studies), J.-P. Lenain (HESS-I analysis), D. Sanchez (Fermi-LAT analysis and multi-wavelength fits). These results show the improvement that CT5 brings to H.E.S.S. measurements of two AGNs, highlighting the benefits of a lower energy threshold for the study of Active Galactic Nuclei.

2.1 Bigger dish, lower threshold for the observation of H.E.S.S. blazars

When going to lower energies, the density of Cherenkov light decreases and it is vital to have a bigger mirror to be able to collect enough Cherenkov photons to trigger the cameras of an IACT. For this purpose, the H.E.S.S. Collaboration in 2012 installed a new telescope (CT5) in the middle of the original 4-telescope array (CT1-4, see section 1.7.4).

The analysis of the MONO data (where data only from CT5 is used) is quite challenging and involves rigorous checks to estimate systematic errors, but it has made possible the observation, and the study of, the gamma-ray sky below 100 GeV in the Southern hemisphere.

One of the first works that has used CT5 data is the study of two bright blazars, PKS 2155−304 and PG 1553+113 reported in [96]. These two sources were targets of observing campaigns in 2013 and 2014 and were analysed using H.E.S.S. analysis software adapted for data taken by the single CT5 telescope. The choice of these sources was driven by their characteristics in terms of energy spectrum and their position in the sky for the H.E.S.S. array. Both sources belong to the HBL class[1] and are well known TeV emitters. PKS 2155−304 is found at a redshift $z = 0.116$ [97] and it has been well studied by the H.E.S.S. Collaboration since the beginning of its construction [98], after the first discovery claims by the Durham Mark 6 Telescope [99]. From the position of the H.E.S.S. array, this blazar is observable at very small zenith angles and even the phase I of the experiment was able to reconstruct the spectrum down to an energy of 160 GeV [100]. The spectral behaviour of the source depends strongly on its flux level and while during quiescent periods, the photon distribution follows a power-law with index $\Gamma = 3.53 \pm 0.06_{\mathrm{stat}} \pm 0.10_{\mathrm{syst}}$, in higher flux states, the photon spectrum shows indications of curvature [101]. Due to its brightness and its optimal visibility from the H.E.S.S. site, this source has become a reference for the instrument and a natural candidate to test the performance of the latest telescope of the array on an extragalactic source.

PG 1553+113 was instead first announced as a very high energy emitter by the H.E.S.S. Collaboration in 2006 [102] and soon after confirmed by the MAGIC Collaboration [103]. The redshift of this source has not been clearly measured spectroscopically, but indirect measurements based on the EBL absorption of gamma ray photons, give a value $z = 0.49 \pm 0.04$ [104], compatible with the redshift interval obtained via UV observations of $0.43 \leq z \leq 0.58$ [105]. Due to this source's Northern declination, the H.E.S.S. array can observe this source only with a rather large zenith angle and consequently, a high energy threshold. Early observations reported a spectrum well fitted by simple a power-law function with index $\Gamma = 4.5 \pm 0.3_{stat} \pm 0.1_{syst}$ down to 225 GeV [102]. Because of the very steep spectrum, this blazar is a clear example of a source that could gain a massive amount of photon statistics even for a small lowering of the energy threshold: a

[1] HBL stands for *High Peaked BL Lacs*, a sub-class of BL Lac objects characterized by a synchrotron peak situated at X-ray energies.

decrease in the energy threshold by a only a factor 2 would allow the detection of more than 10 times more photons[2].

These two sources are well detected also by the *Fermi*-LAT. According to the 3FGL catalogue [106], which reports the average of their emission between the years 2008 and 2012, in the energy range 100 MeV - 300 GeV, their spectra are hard, with the index of a fitting power-law function smaller than 2. However, the averaged emission in the HE range (100 MeV $< E <$ 300 GeV), over this long integration time, is better described by a log-parabola function in the form:

$$\frac{dN}{dE} = N_0 \left(\frac{E}{E_0}\right)^{-\left[\alpha+\beta \ln\left(\left(\frac{E}{E_0}\right)\right)\right]} \tag{2.1}$$

which indicates an intrinsic curvature of the spectrum over the *Fermi*-LAT energy range.

The datasets were processed with the standard H.E.S.S. analysis software making use of the Model reconstruction [90], adapted after the year 2012 for the analysis of the data coming from the new inhomogeneous array [89]. Different sets of selection cuts were developed to deal with different type of sources and in this chapter we made use of *standard* and *loose* cuts which differ in terms of the likelihood of triggering on the night sky background. *Standard* cuts are more strict, thus have a higher low-energy threshold, but give a better sensitivity for sources with photon indices lower than 3.0[3]. On the other end *loose* cuts have a lower energy threshold and are best suited for sources with steep spectra, but might be more affected by systematic effects. Background subtraction is performed using the standard algorithms used in H.E.S.S.: the ring background method (for sky maps) and the reflected-region background method (with multiple off-source regions, for spectral measurements, see Appendix D) [107].

2.1.1 PKS 2155−304

Due to the early stage of CT5 functionality, the campaign on PKS 2155−304 in 2013 and 2014 made use of observation runs of various types, to test the performance of the instrument in different conditions. The distribution of the zenith angles of the observation runs in the dataset goes from 7 to 60 degrees with a median of 16°, and the

[2]This "back-of-the-envelope" calculation is based on the fact that the energy dependence of the number of particles goes as $E^{-\Gamma+1}$ and relies on the fact that the photon index would remain constant, which might not be the case due to intrinsic spectral curvature or in the presence of other phenomena that would induce a change in the photon index, like the variable absorption by the EBL as a function of the photon energy.

[3]Generally, small absolute values of the photon index are called *hard*, while large absolute values are called *soft*.

offset between the source and the pointing position of the camera ranges from 0.45 to 1.2 degrees. After the selection of good runs, the final live time of the observation is 56 hours, 43.7 taken in 2013 and 12.3 in 2014 yielding an overall detection significance of 42 σ through more than 4000 excess events. To demonstrate the results achieved below the symbolic limit of 100 GeV, Figure 2.1 shows the results of the analysis with *standard cuts* only for events with a reconstructed energy lower than this threshold.

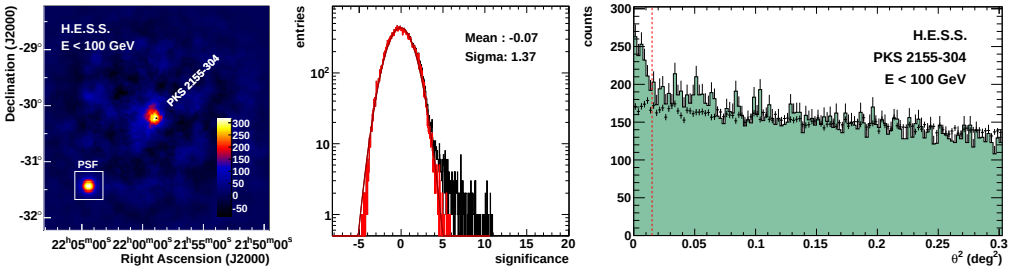

(A) Excess map (B) Significance Distribution (C) θ^2 distribution

FIGURE 2.1: Plots showing the detection of the source PKS 2155−304 using MONO data below 100 GeV. The *left* panel reports the excess map with the inset illustrating the size of the PSF of the instrument. A black dot shows the catalogue position of the source. The *middle* panel shows the significance distribution of the corresponding excess map, where the red histogram is the significance distribution obtained after the exclusion of a circle with radius 0.3° centred in the source position. Also shown in this panel is the best fit of this last histogram with a Gaussian function. The *right* panel shows instead the distribution of gamma-like events as a function of the squared angular distance from the source (green histogram), compared with the distribution coming from the off-source regions (black points). The red vertical dashed line represents the size of the on-source region.

In optimal conditions, assuming a perfect background estimation, the significance distribution of the background shown in red in Figure 2.1b would be centred on 0, with a width of exactly 1 (being the result of random noise). The presence of errors in the background estimation and subtraction are responsible for the widening of the significance distribution we observe in our dataset. If we take into account a systematic contribution to the total error and assume it can be summed in quadrature with the statistical one, it is possible to estimate the fraction of the widening related to this systematic effect in the background subtraction:

$$\sigma_{tot} = \sqrt{\sigma_{stat}^2 + \sigma_{syst}^2} = \sqrt{1 + \sigma_{syst}^2}$$

for events below 100 GeV, this gives a value of 0.94 for the ratio between the systematic and the statistical error.

The full spectrum of the source is reconstructed for the full 2013+2014 dataset and for the data collected in each year separately, to identify possible large source variations on a year time-scale. The SED for the 2013 dataset is shown in Figure 2.2a, while the separate results for each year of data taking, are represented in Figure 2.2b. When fitting the full dataset, the best fit function is found to be a log-parabola, which is preferred over a simple power-law at a $\sim 5\,\sigma$ confidence level (statistical significance determined through a Log Likelihood Ratio Test - LLRT). The fit results are summarized in Table 2.1. For the full dataset, we obtain, above a threshold of 80 GeV, a flux normalization $\Phi_0 = (5.11 \pm 0.15) \times 10^{-10}\,\mathrm{cm}^{-2}\,\mathrm{s}^{-1}\,\mathrm{TeV}^{-1}$ at a decorrelation energy[4] $E_0 = 156$ GeV, with a photon index $\Gamma = 2.63 \pm 0.07$ and a curvature parameter $\beta = 0.24 \pm 0.06$.

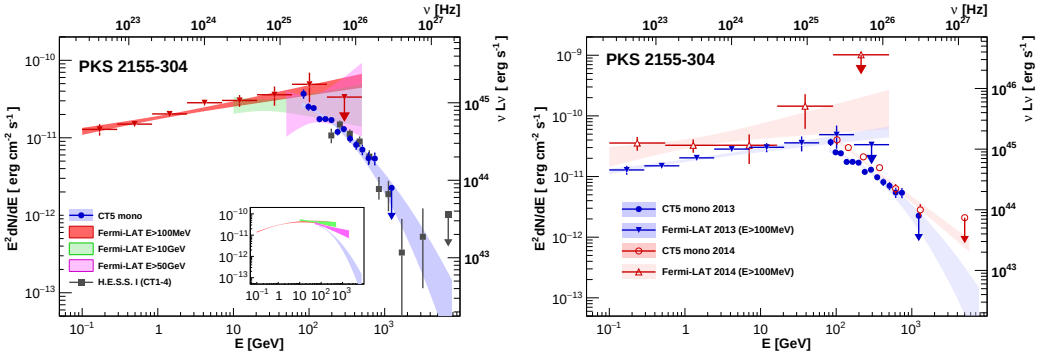

(A) SED of PKS 2155−304 for the 2013 dataset compared with *Fermi*-LAT spectrum.

(B) SED of PKS 2155−304 for the 2013 and 2014 dataset compared with *Fermi*-LAT spectrum.

FIGURE 2.2: In the *left* panel: the energy spectrum of PKS 2155−304 obtained from the H.E.S.S. II MONO analysis (2013 data, shown by blue circles with confidence band) is compared to: contemporaneous *Fermi*-LAT data with an energy threshold of 0.1 GeV (red triangles and confidence band), 10 GeV (green band), and 50 GeV (purple band) and contemporaneous CT1–4 data (grey squares). In all cases the confidence bands represent the 1 σ region. The right-hand y-axis shows the equivalent isotropic luminosity (not corrected for beaming or EBL absorption). The inset compares the H.E.S.S. confidence band with the *Fermi*-LAT catalogue data (3FGL, 1FHL and 2FHL, see Sect. 2.2). The *right* panel instead shows a comparison between the spectra measured in 2013 by H.E.S.S. and *Fermi*-LAT (blue spectra) and in 2014 (red spectra).

From Figure 2.2b, we see evidence for variability in the emission of the source, with 2014 dataset being a factor 1.6 ± 0.1, brighter than the 2013 dataset, but without a significant change in the spectral shape of the source. This change in the luminosity of the source is reflected also in the *Fermi*-LAT data, which show a similar flux increase in the 2014 dataset compared to the 2013 dataset.

[4]The decorrelation energy is the energy where the error on the differential flux is the smallest, i.e. where the confidence band butterfly is the narrowest in the graphical representation.

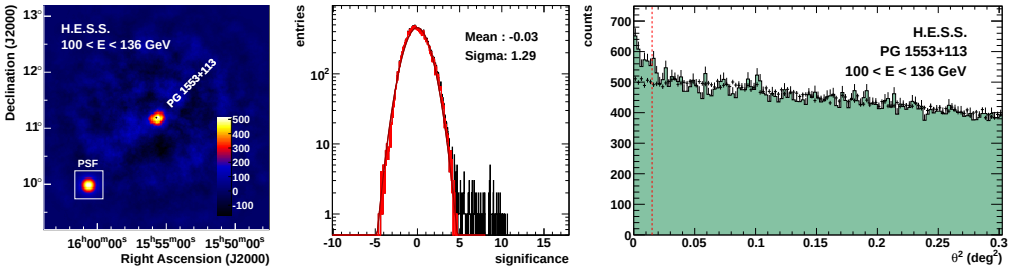

(A) Excess map (B) Significance Distribution (C) θ^2 distribution

FIGURE 2.3: *Left* panel: The PG 1553+113 excess map. *Middle* panel: significance distribution for events with reconstructed energy between 100 GeV and 136 GeV (H.E.S.S. II MONO analysis). *Right* panel: The distribution of θ^2 (squared angular distance to PKS 2155−304) for gamma-like events. The explanation of the colours in the graphs is the same as in Figure 2.1.

2.1.2 PG 1553+113

The dataset of PG 1553+113 is shorter, taken over a 3-month observation campaign in 2013. The number of runs that survive the selection cuts is 39, for a total livetime of 16.8 hours. Due to the softer spectrum, this dataset is analysed with *loose* cuts to maximise the gain due to a lower energy threshold. Compared to the PKS 2155−304 dataset, this dataset is more homogeneous, with zenith angles ranging between 33° and 40°, with a mean value of 35°. The source is detected with a confidence level of 27 σ, with ≈ 2500 excess events. Because of the larger zenith angle, for this source it is not possible to reach energies below 100 GeV, but the results for an energy bin between 100 GeV and 136 GeV demonstrate the goodness of the reconstruction at the lowest energies accessible for this blazar with a detection in this energy range at a 10 σ level, shown in Figure 2.3. In this case the width of the significance of the background distribution is $\sigma = 1.288 \pm 0.005$ for this low energy bin, indicating a level of systematic effect in the background subtraction $\sigma_{sys} = 0.8\sigma_{stat}$.

The reconstructed spectrum, with a threshold of 108 GeV, is found to be well-fit by a log-parabola (with a Log Likelihood Ratio Test - LLRT of 20 over the power-law model, indicating a preference for the curved function with a significance level between 4 and 5 σ). The SED obtained from the dataset is shown in Figure 2.4. The best fit results are reported together with those of PKS 2155−304 in Table 2.1: a differential flux $\Phi_0 = (1.48 \pm 0.07) \times 10^{-9}\,\mathrm{cm}^{-2}\,\mathrm{s}^{-1}\,\mathrm{TeV}^{-1}$ at a decorrelation energy $E_0 = 141$ GeV, an index $\Gamma = 2.95 \pm 0.23$ and a curvature parameter $\beta = 1.04 \pm 0.31$.

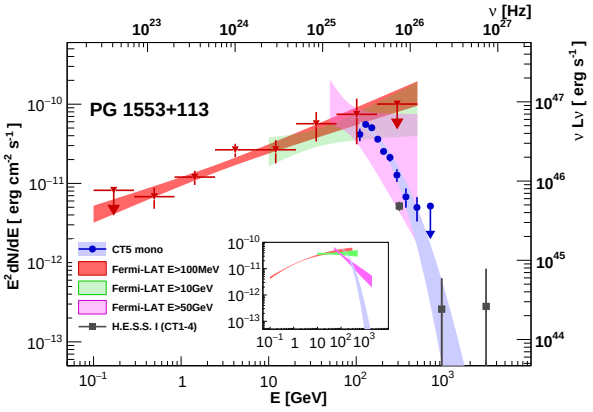

FIGURE 2.4: The energy spectrum of PG 1553+113 obtained from the H.E.S.S. II MONO analysis (blue) in comparison to the contemporaneous *Fermi*-LAT data with an energy threshold of 0.1 GeV (red triangles and confidence band), 10 GeV (green band), and 50 GeV (purple band) and contemporaneous CT1–4 data (grey squares). In all cases the bands shown represent the 1 σ confidence region. The right-hand y-axis shows the equivalent isotropic luminosity (not corrected for beaming or EBL absorption) assuming redshift $z = 0.49$. The inset compares the H.E.S.S. confidence band with the *Fermi*-LAT catalogue data (3FGL, 1FHL and 2FHL, see Sect. 2.2).

2.1.3 Cross check analysis and systematic assessment

To ensure the robustness of this new H.E.S.S. II analysis of MONO data, I performed a cross check of all the results through an independent pipeline based on the Image Pixel-wise fit for Atmospheric Cherenkov Telescopes (ImPACT) method described in Parsons and Hinton [91], which was adapted by the H.E.S.S. Collaboration for use on data taken during the H.E.S.S. II phase [92]. The run-list I use for these tests is extracted taking the intersection of the available runs within the independent pipelines. Given the lack of variability within the yearly time intervals, this selection effect does not affect the comparison between the reconstructed fluxes[5].

This independent analysis is able to detect PKS 2155−304 below 100 GeV equally well, and all the results are in good agreement with those shown in the previous subsections. In addition, we use the differences found between the values of the fitted parameters of the spectra using the two different reconstruction methods, to estimate the systematic effects due to the calibration of the data, the reconstruction, and the analysis techniques. These are reported in Table 2.3, which summarises all the systematic uncertainties.

The comparison between the ImPACT spectral reconstruction and the Model one is illustrated in Figure 2.5. From these plots it is possible to see in which conditions the

[5]Even though there is an increase in brightness for PKS 2155−304 in 2014 with respect to the measurements taken in 2013, we find no evidence of flux variability within the 2013 and 2014 data analysed separately.

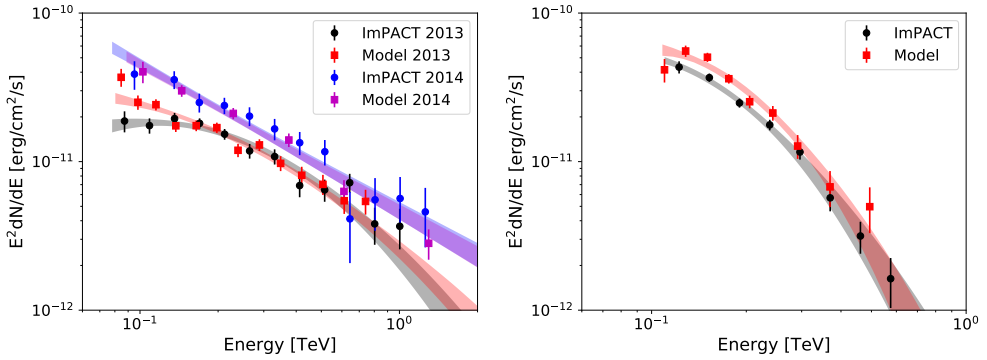

(A) PKS 2155−304 (B) PG 1553+113

FIGURE 2.5: Comparison between the analysis made with the ImPACT reconstruction and with the Model one. The *left* panel compares results for PKS 2155−304, separated for the two datasets (black and blue circles for the ImPACT method and red and magenta squares for the Model analysis). The *right* panel shows the same but for the 2013 PG 1553+113 dataset.

systematic effects are stronger. In Figure 2.5a the disagreement between the two analyses is more evident at the lowest energies, below 150 GeV. Because the systematic uncertainties on background subtraction increase with the length of the observations, however, when we use the shorter dataset from 2014, the agreement improves significantly. In the case of PG 1553+113, we find somewhat larger systematics because the larger zenith angle of these observations does not provide conditions as optimal as those for PKS 2155−304.

As this is the first in-depth analysis on astrophysical sources using H.E.S.S. II MONO data, the cross checks I did on the analysis made possible the improvement of the reconstruction chain. This led to the identification of several bugs in the code with the effect of an improvement in the background rejection power of the ImPACT analysis method. This is an ongoing effort to provide the H.E.S.S. Community with two fully functional, independent analysis chains to analyse Cherenkov data and ensure the robustness of the published results.

Figures 2.2a and 2.4 show also the H.E.S.S. I data collected simultaneously with the MONO data and analysed with the Model analysis technique [90] using the *loose cuts* [108] to ensure a low energy threshold. For PKS 2155−304 we have 27.2 hr of good H.E.S.S. I data, while for PG 1553+113, we have 9.0 hr. The significances of the H.E.S.S. I detections are 45.9σ and 9.0σ respectively. The difference in the amount of live time compared to the MONO datasets is due to the fact that for the H.E.S.S. I analysis, the run list is different because of the different selection criteria and operation

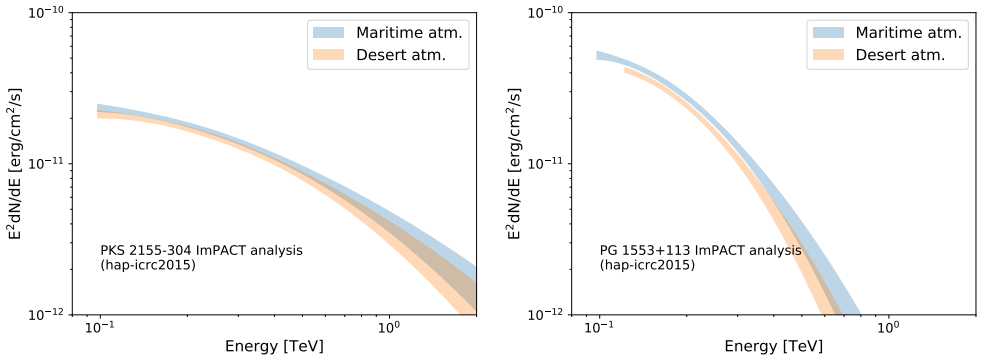

(A) PKS 2155−304 (B) PG 1553+113

FIGURE 2.6: Comparison between the reconstructed spectra using *maritime* (light-blue) and *desert* (orange) atmospheric configurations for PKS 2155−304 (*left* panel) and PG 1553+113 (*right* panel).

modes of the array. Within the quoted systematics, the H.E.S.S. I results show a good agreement with the H.E.S.S. II MONO data.

Table 2.3, reports all the different contributions to the total systematic uncertainty of various aspect of the analysis. The uncertainty on the energy scale is dominated by the reconstruction and selection cuts, contributing 15%, for a total uncertainty of 19%, with the rest of the uncertainty coming from the simulation of the variation in the atmospheric response (7%) and from instrument calibration (10%). Regarding the systematic uncertainty on the flux normalization, the major contribution is coming from the reconstruction side of the analysis, with comparable contributions from the various steps in the instrument calibration and background subtraction. A point worth highlighting is the fact that the systematics related to the presence of background are actually energy dependent, with a stronger effect as one approaches the threshold.

For the ImPACT analysis[6], the effect of the atmospheric model adopted in the Monte Carlo simulations is shown in Figure 2.6. In the plots, the effect of using two different models for the atmospheric transparency (available in the SIM_TELARRAY software used to simulate the array response [109, and ref. therein]) are compared. The model called *maritime* was the one wrongly adopted for the first sets of simulations for CT5 run by the H.E.S.S. Collaboration and it is based on the transmission coefficient at seaside regions at 0 m a.s.l.. This model was subsequently substituted with the model in use for the other telescopes (labelled with *desert*).

[6]The comparison reported here refers to a software version available during the data analysis. This version was then substituted with a different one right before the publication of the final results.

The atmospheric transparency directly affects the energy reconstruction of the gamma-ray photon due to the absorption of Cherenkov photons produced by the incoming shower. As visible from Figure 2.6, the effect of shifting the energy scale has an impact on the spectral parameters of the sources. Fitting the spectra with a log-parabola function (see Equation 2.1) with normalization energy $E_0 = 0.19$ TeV, for PKS 2155−304, the difference in flux normalization level was −6%, the effect on the parameter α was below 1% while the parameter β increased by 16%. For PG 1553+113, the flux normalization went down by 11%, while α increased by 2% and β increased by 27%. The fact that the change in the spectral parameters is more prominent for PG 1553+113, can be easily explained by the larger zenith angle of the observation and hence the larger distance that the Cherenkov photons have to travel to reach the telescope. These atmospheric effects were then incorporated in the total systematic uncertainties on the final results.

2.2 PKS 2155−304 and PG 1553+113 observed by *Fermi*-LAT

One of the main goals of this study was to bridge the gap present in the quality of the data between *Fermi*-LAT and H.E.S.S. through the use of the CT5 telescope. For this reason, we analyse also the *Fermi*-LAT data collected in time intervals coincident with those of the H.E.S.S. observations for the two sources. The *Fermi*-LAT analysis performed for the study involves the use of data collected by the satellite above 100 MeV and within 15° from the position of the source of interest. The data are analysed using the publicly available Science Tools `v10r0p5`[7] and the `P8R2` instrument response functions, event class 128, event type 3 with a zenith angle cut of 90° (see details in Appendix C). This particular analysis is performed using the `Enrico` Python package [110] adapted for standard `PASS8` analysis. To model the emission of all the sources in the field of view and the contribution from the diffuse emission, a sky model was prepared based on the 3FGL catalogue [106] and the Galactic diffuse background `gll_iem_v06.fits` [111] and the isotropic background `iso_P8R2_SOURCE_V6_v06.txt`.

The analysis is performed in three different energy ranges: 0.1 GeV–500 GeV, 10 GeV–500 GeV and 50 GeV–500 GeV and the results are summarized in Table 2.2. For the full energy range, using contemporaneous data, there are not enough statistics to prefer the fit with a log-parabola with respect to a simple power-law function. However, signs of intrinsic curvature can be observed through the analysis of the other energy ranges, which show indications of a steepening of the spectrum at higher energies as visible in

[7] `http://fermi.gsfc.nasa.gov/ssc/data/analysis/documentation/`.

Figures 2.2a and 2.4 and from the photon indices reported in Table 2.2. This effect is more evident when comparing the catalogue data extracted from the 3FGL [106], the 1FHL [112] and the 2FHL [113]. These are obtained through the integration of the signal over a much longer time period (4 years for the 3FGL and 3 years for the 1FHL and 80 months for the 2FHL) and they probe different energy ranges: 100 MeV - 300 GeV; 10 GeV - 500 GeV and 50 GeV - 2 TeV respectively. The catalogue values are shown in the insets of Figure 2.2a and 2.4. Interestingly, the down-turn feature appears exactly in the overlapping range of the two instruments. The H.E.S.S. data bring high precision measurements in an energy range that can only be explored in an averaged way by the less sensitive *Fermi*-LAT, requiring very long integration time to get useful constraints on the emission.

2.3 Results from *Fermi*-LAT and H.E.S.S.

From Figures 2.2a and 2.4, we can see that the new data collected with H.E.S.S. II are able to cover, with a much greater precision, the point where the spectral down-turn kicks in. A further deconvolution of the EBL effect allows the study of the intrinsic spectrum of the sources.

The first step in this direction is to fit the H.E.S.S. data so as to take into account the EBL (as in the model of Franceschini et al. [55]) effect. For the 2013 dataset of PKS 2155−304, the best fit intrinsic (unabsorbed) power-law index is $\Gamma_{int} = 2.49 \pm 0.05$, which is much softer than the index obtained from the *Fermi*-LAT data, which are not affected by EBL absorption ($\Gamma_{LAT} = 1.82 \pm 0.03$). This fact already indicates the presence of an intrinsic curvature in the spectrum of this source. Because of the lack of a clear spectroscopic red-shift measurement, a similar procedure for PG 1553+113 requires an assumption on z, which is set to the value of 0.49 (motivated by [104]). For this source, the intrinsic photon index is then found to be $\Gamma_{int} = 1.91 \pm 0.13$, which again seems to point towards a curvature effect in the intrinsic spectrum of the source when compared with the harder value of $\Gamma_{LAT} = 1.59 \pm 0.07$ from *Fermi*-LAT. A statistically significant presence of intrinsic curvature can be tested through a joint fit of the *Fermi*-LAT and H.E.S.S. datasets. For the case of PKS 2155−304, when using only the statistical errors associated to both datasets, significant curvature is found in the data, with a log-parabola significantly ($> 5\ \sigma$) preferred to a power-law function to fit both datasets. The peak of the SED is found to lie at an energy of ~ 10 GeV. In the case of PG 1553+113 instead, the presence of an intrinsic curvature in the spectrum is only marginally significant, with a preference over a power-law function of only 2.2 σ.

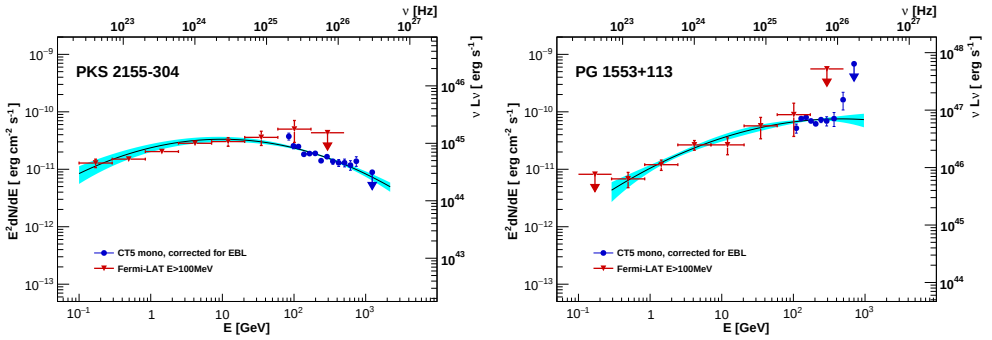

(A) PKS 2155−304 (B) PG 1553+113

FIGURE 2.7: Energy spectrum for 2013 PKS 2155−304 (*left* panel) and PG 1553+113 (*right* panel) with *Fermi*-LAT data (in red) and the EBL de-absorbed H.E.S.S. points (in blue) with the best fit log-parabola superimposed. The black line is the best-fit log-parabola model to the points, and the cyan butterfly indicates the 1 σ region using only the statistical errors in the combined data set analysis. The right-hand y-axis shows the equivalent isotropic luminosity (not beam corrected).

This result puts the possible intrinsic peak of the SED at an energy of 0.6 TeV, but with correspondingly large uncertainties. The results of these fits are shown graphically in Figure 2.7 and reported in Table 2.4.

The uncertainties in the intrinsic spectrum increase when the systematic errors are taking into account. The main contributor is found to be the determination of the true de-absorbed H.E.S.S. spectrum due to the uncertainty on the energy scale. The uncertainty in the real energy of the photons propagates into an uncertainty on the actual EBL effect that needs to be removed to obtain the intrinsic spectrum. The correct way to take this effect into account is to apply an energy shift of the spectral bins before applying the EBL deconvolution. This shift has to be implemented in the representation EdN/dE to conserve the number of photons in each energy bin. From Table 2.3, this uncertainty is estimated to be 19%. The fit to the shifted data is then used to quantify the effect of the systematics on the original intrinsic spectrum, reported in Table 2.4. As we can see, for PG 1553+113, the final effect is to make the curvature parameter β of the log-parabola completely compatible with 0, i.e., turning the log-parabola into a simple power-law function.

2.4 Conclusions

The results shown in this chapter (with more details in [96]) assess the improvements obtained using the new H.E.S.S. reflector over the *Fermi*-LAT capabilities when we deal with energies above tens of GeV and on shorter integration times.

What I have presented here is the successful detection of the two extragalactic sources, PKS 2155−304 and PG 1553+113, using data obtained with H.E.S.S. II MONO. This has finally opened the energy window below 100 GeV in the Southern Hemisphere. The data are found to be in very good agreement with those collected by the *Fermi*-LAT on contemporaneous time intervals. Furthermore, the synergy between *Fermi*-LAT and H.E.S.S. allows a good characterization of the intrinsic spectrum of the sources, obtained after the deconvolution of the EBL effect on the measured fluxes. This step has allowed us to determine the curvature parameter of the spectrum, under the assumption that the spectrum of the two sources can be described via a log-parabola function and also identify the position of the high energy peak of the SED. In the case of PKS 2155−304, this is located around $\sim$ 10 GeV. For PG 1553+113, which has a barely significant intrinsic curvature in its spectrum (assuming a redshift $z = 0.49$), the peak could be positioned at an energy of $\sim$ 600 GeV, outside the range of the measurements that we obtain.

The performance of the CT5 MONO analysis were carefully tested for systematic errors and cross checked with an independent analysis pipeline. They were also compared to the results that can be obtained through the analysis of the data of the historical H.E.S.S.-I array, showing the massive improvement in the detection of sources with steep spectra, like PG 1553+113, which benefited incredibly from the lowered energy threshold. The analysis is, however, still affected by some systematics in terms of background reconstruction which prevents the system from being able to reach the full potential of an energy threshold of a few tens of GeV. These uncertainties are mainly due to the fact that these kind of observations are analysed using only the signal from one telescope and thus cannot make use of the background rejection one obtains with a stereoscopic reduction. The results obtained here are, however, significant for the future of gamma-ray astrophysics with ground-based telescopes. The heterogeneous array of H.E.S.S. II can be thought of as a sort of precursor of what CTA will be: a system with three different type of telescopes to investigate the gamma-ray sky from few tens of GeV to hundreds of TeV.

As will be briefly mentioned at the end of Chapter 6, the best use for CT5 is to observe bright flaring objects, where two effects join to improve the performance of the instrument: the brightness of the source and the short observation time, that will reduce the impact of systematic noise in the data. So, while this work serves to establish the performance of CT5 on two important extragalactic sources, the observation of short transients can benefit the most from it.

TABLE 2.1: Spectral analysis results of H.E.S.S. II MONO observations. For both blazars, the observational period is provided along with the spectral parameters: decorrelation energy E_0; differential flux at the decorrelation energy Φ_0; photon index $\mathbf{\Gamma}$; and curvature parameter β. These three parameters describe the log-parabola fit to the spectra.

Source	Year	MJD	Livetime [hr]	E_0 [GeV]	Φ_0 $[10^{-9}\,\mathrm{cm}^{-2}\,\mathrm{s}^{-1}\,\mathrm{TeV}^{-1}]$	$\mathbf{\Gamma}$	β
PKS 2155−304	2013	56403–56601	43.7	151	$0.530 \pm 0.018_{\mathrm{stat}}$	$2.65 \pm 0.09_{\mathrm{stat}}$	$0.22 \pm 0.07_{\mathrm{stat}}$
	2014	56805–56817	12.3	177	$0.532 \pm 0.029_{\mathrm{stat}}$	$2.82 \pm 0.13_{\mathrm{stat}}$	$0.16 \pm 0.10_{\mathrm{stat}}$
	2013+2014	56403–56817	56.0	156	$0.511 \pm 0.015_{\mathrm{stat}}$	$2.63 \pm 0.07_{\mathrm{stat}}$	$0.24 \pm 0.06_{\mathrm{stat}}$
PG 1553+113	2013	56441–56513	16.8	141	$1.48 \pm 0.07_{\mathrm{stat}}$	$2.95 \pm 0.23_{\mathrm{stat}}$	$1.04 \pm 0.31_{\mathrm{stat}}$

TABLE 2.2: *Fermi*-LAT spectral analysis results for the time intervals contemporaneous with the H.E.S.S. II observations. For each data set and energy threshold, E_{th}, the differential flux ϕ_0 at decorrelation energy E_0, photon index Γ, and value of the test statistic (TS), for the power-law fit, are provided.

Source	Year	MJD	$\mathrm{E_{th}}$ (GeV)	ϕ_0 10^{-11}(ph cm^{-2}s^{-1}GeV^{-1})	Γ	$\mathrm{E_0}$ (GeV)	TS
PKS 2155−304	2013	56403–56601	0.1	557± 26	$1.82^{+0.03}_{-0.03}$	1.48	2162.6
			10	2.52 ±0.43	$2.00^{+0.21}_{-0.21}$	25.5	379.7
			50	0.12±0.05	$1.82^{+0.66}_{-0.72}$	112	52.4
PKS 2155−304	2014	56805–56817	0.1	996±168	$1.79^{+0.13}_{-0.13}$	1.54	193.5
			10	2.36±1.18	$1.20^{+0.45}_{-0.45}$	53.3	52.4
			50	1.00±0.71	$1.53^{+1.03}_{-1.20}$	115	23.7
PG 1553+113	2013	56403–56817	0.1	118±13	$1.59\ ^{+0.07}_{-0.07}$	2.95	455.6
			10	2.04±0.53	$1.68^{+0.26}_{-0.21}$	33.5	169.9
			50	0.64±0.27	$2.97^{+0.91}_{-1.13}$	80.8	66.8

TABLE 2.3: Estimated contributions to the systematic uncertainties in the spectral measurements using H.E.S.S. II mono for the analyses presented in this work. Numbers separated by "/" correspond to PKS 2155−304 and PG 1553+113, respectively. Refer to [96] for a complete description.

Source of Uncertainty	Energy Scale	Flux	Index	Curvature
MC shower interactions	–	1%	–	–
MC atmosphere simulation	7%		–	–
Instrument simulation / calibration	10%	10%	–	–
Broken pixels	–	5%	–	–
Live Time	–	$< 5\%$	–	–
Reconstruction and selection cuts	15%	15%	0.1 / 0.46	0.01 / 0.8
Background subtraction	–	6%/10%	0.14 / 0.46	0.12 / 0.6
Total	19%	20%/22%	0.17 / 0.65	0.12 / 1.0

TABLE 2.4: Parameters obtained for the combined fit of the *Fermi*-LAT and H.E.S.S. data. The reference energy E_0 used here is 100 GeV. For both blazars, the log-parabola fits values are provided. For PG 1553+113, the values for the power-law model, which was marginally disfavoured, are also given. The last column gives the significance, obtained by comparing the χ^2 values for the log-parabola model against those for the power-law model, using only statistical errors in the analysis.

Source	$\phi_0[10^{-11}$ cm^{-2}s$^{-1}]$	$\mathbf{\Gamma}$	β	$log_{10}(E_{\rm peak}$[GeV])	Sig. (σ)
PKS 2155−304	$2.35 \pm 0.10_{\rm stat} \pm 0.57_{\rm sys}$	$2.30 \pm 0.04_{\rm stat} \pm 0.09_{\rm sys}$	$0.15 \pm 0.02_{\rm stat} \pm 0.02_{\rm sys}$	$0.99 \pm 0.19_{\rm stat} \pm 0.19_{\rm sys}$	5.1
PG 1553+113	$5.97 \pm 0.25_{\rm stat} \pm 2.19_{\rm sys}$	$1.68 \pm 0.05_{\rm stat} \pm 0.13_{\rm sys}$	–	–	–
PG 1553+113	$6.66 \pm 0.42_{\rm stat} \pm 1.43_{\rm sys}$	$1.83 \pm 0.08_{\rm stat} \pm 0.29_{\rm sys}$	$0.12 \pm 0.05_{\rm stat} \pm 0.13_{\rm sys}$	$2.76 \pm 0.45_{\rm stat} \pm 0.93_{\rm sys}$	2.2

Chapter 3

PSR B1259-63 with H.E.S.S., importance of contemporaneous observations

The GeV range can hide interesting phenomena like the "GeV-flare" of the binary PSR B1259−63. For the study of this phenomenon it becomes particularly important having contemporaneous observations at different wavelength. Following the summary of the gamma-ray binary phenomenon presented in the introduction (see Section 1.5.3), I go into more details on the H.E.S.S. observation of one particular binary, PSR B1259−63. Part of the work was published as conference proceedings for the ICRC 2015 [114] and for GAMMA 2016 [115]. At the time of writing, these results are being finalised for a further journal publication, where I will be part of the team of corresponding authors. I have performed the full Fermi-LAT analysis and contributed to the H.E.S.S. one. My key collaborators on this project are P. Bordas (H.E.S.S. analysis and interpretation), C. Mariaud (H.E.S.S. analysis) and T. Murach (H.E.S.S. analysis and leader of the PSR B1259−63 binary task force).

3.1 Orbital modulation of the binary emission

3.1.1 Description of the system

The gamma-ray binary PSR B1259-63 is a system comprising a pulsar in orbit around the Be star LS 2883. One of the peculiarities of this system, is that it is the only case

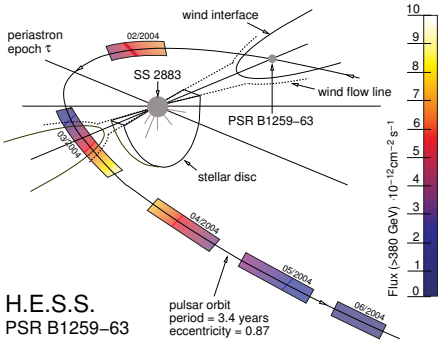

FIGURE 3.1: Orbital geometry of the PSR B1259−63/LS 2883 system, taken from [121]. The shaded areas indicate the position of the pulsar along its orbit during the 2004 H.E.S.S. observation periods. The colour of the shading represents the intensity of the observed VHE emission, as given by the colour-flux mapping in the bar at the right-hand side of the figure.

in the class of gamma-ray binaries for which the nature of the compact object has been clearly established. The pulsar has a period of 48-ms with an associated spin-down luminosity $\dot{E} \approx 8 \times 10^{35}$ erg/s [59, 116].

The companion star (LS 2883) has a mass of ∼20-30 $M_\odot$ and drives a stellar wind and an equatorial outflow which forms a disc around the star which extends for at least 10 stellar radii [116–118].

The orbital period of the system is the longest in the gamma-ray binaries sample detected so far, being 3.4 years. The orbit itself, shown schematically in Figure 3.1, is quite eccentric with an eccentricity parameter $e \sim 0.87$. This means the pulsar-companion separation decreases from 13.4 Astronomical Units (AU) at the apoastron to less than 1 AU at the periastron [116, 119, 120].

3.1.2 The multiwavelength view: a surprise in gamma-rays

Because the plane of the orbit is inclined with respect to the plane of the circumstellar disk, the pulsar crosses the disk twice when it is close to the periastron. Its interaction with the stellar wind and the circumstellar disk gives rise to an enhancement of the non-thermal emission that is visible across the full electromagnetic spectrum, from radio to gamma rays [see e.g 118, Fig. 1]. The moments of the crossing with respect to the time of the periastron ($t_{\rm per}$) are inferred from the disappearance of the pulsed signal of the neutron star. This happens at $t_{\rm per} - 15$d and $t_{\rm per} + 15$d [122]. Coincident with this crossing, there is a clear brightening in the X-ray and radio light curve so that a double-peak structure is formed [118].

At very high energies, the H.E.S.S. Collaboration discovered the source during the periastron passage in 2004 and recorded also the subsequent passages in 2007, 2010/2011 and 2014 (this latest passage is the main focus of this chapter). Any observation at other orbital phases did not lead to a detectable signal [114, 115, 121, 123, 124].

Before entering into the details of the VHE emission of this source, there is an interesting point regarding the emission detected at GeV energies. The first periastron event observable with the *Fermi* satellite was in 2011. At this time, the emission of the source in this energy band was for the most part extremely low, usually below the sensitivity limit of the instrument. As a complete surprise, however, a flaring state that started ~ 30 days after the periastron passage was detected, lasting for roughly a month. The power emitted by this event was so high that it almost matched the spin-down luminosity of the pulsar [125, 126]. The presence of the flare was detected again in 2014 strengthening the hypothesis that it is a periodic phenomenon [127][1]. After the first detection, the GeV flare was *not* found to be correlated with flaring at other wavelengths. One of the possible interpretations put forward for the GeV flare is that it represented the IC emission of the unshocked pulsar wind on the ambient photon field [128, 129]. However, the most recent observations in X-rays showed a different component with a hard photon index arising at the moment of the GeV flare along with an abrupt decrease in the width of the H_α line seen in the near infrared. These observational results have been explained as the disruption of the disk around the star with the subsequent release of the spin-down energy of the pulsar in a clumpy medium made of the disk fragments [127]. The model, however, leaves open the question of the origin of the accelerated electrons that cause the flare, making the explanation event still very unclear.

Regarding the observation at very high energies, due to the visibility constraints of the ground based telescopes, each observation campaign was only able to probe a different interval of the periastron passage. When merging together the data from 2004, 2007 and 2011 events into a single phase-folded light curve, it was possible to recognize a double-peaked profile of the TeV flux, as at X-ray energies, with a similar minimum at $\sim t_{\rm per}$ [124].

3.2 The 2014 results with H.E.S.S.

The campaign on the occasion of the periastron passage of May 2014 was of high importance for the study of this source. As shown in the preliminary results [114, 115],

[1] EGRET (the *Fermi*-LAT predecessor) might have had sufficient sensitivity to detect the flare, but it never pointed towards the source during that phase interval.

the data-set collected during this event covered some of the visibility gaps left from the campaigns in the previous years (due to the presence of the full moon in the sky as visible from Figure 3.3).

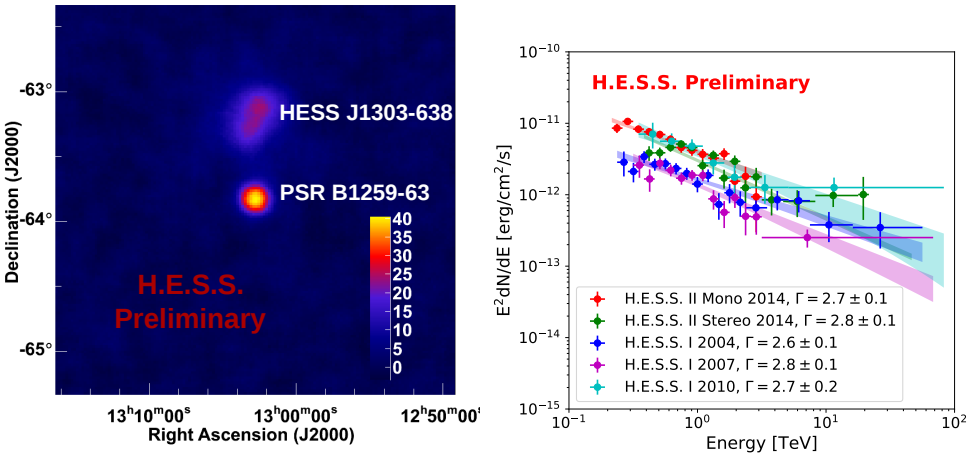

(A) Significance Map (B) Spectrum

FIGURE 3.2: *Left* panel: Significance sky map around the position of PSR B1259−63 using H.E.S.S. II STEREO taken from [114]. The faint emission that is visible just above the source is the pulsar wind nebula HESS J1303−631. *Right* panel: SED of the source using the 2014 data from H.E.S.S. II with the reanalysis of the data of the previous periastron passages superimposed. Plot adapted from [115].

The source was clearly detected with all the configurations of the instruments, as illustrated in Figure 3.2, confirming the performance of the full array also for galactic sources. However, for CT5 MONO data, due to a larger zenith angle and a higher level of contamination from the night sky background and nearby sources, a safe energy threshold of ~ 200 GeV was imposed. The emission over the full energy range follows a straight power-law without indication of a cut-off up to 10 TeV, with a photon index of 2.7 ± 0.1 for the MONO analysis and 2.8 ± 0.1 for the stereo analysis [115]. These results are in complete agreement with what was observed during the previous campaigns using only the other 4 small reflectors (as visible from Figure 3.2b), indicating a lack of detectable spectral variability.

Joining together the data taken during the various campaigns by the H.E.S.S. array allows us to produce a proper phase folded light-curve for energies above 1 TeV. This is shown in the top panel of Figure 3.3 where the data are binned into *moon-to-moon* visibility intervals (called "periods"). Even though this result is preliminary[2], the graph highlights a very interesting picture with a structured light curve at TeV energies. The 2014 data uncover a higher flux state before the periastron passage, approximately 30

[2]At the time of writing results are being finalised within the H.E.S.S. Collaboration and seem to confirm the trend shown in these results.

days before it, followed by the expected high flux observed right after the first disc crossing. Another aspect that arises in the analysis of these data is in relation to the GeV flare seen by the *Fermi*-LAT.

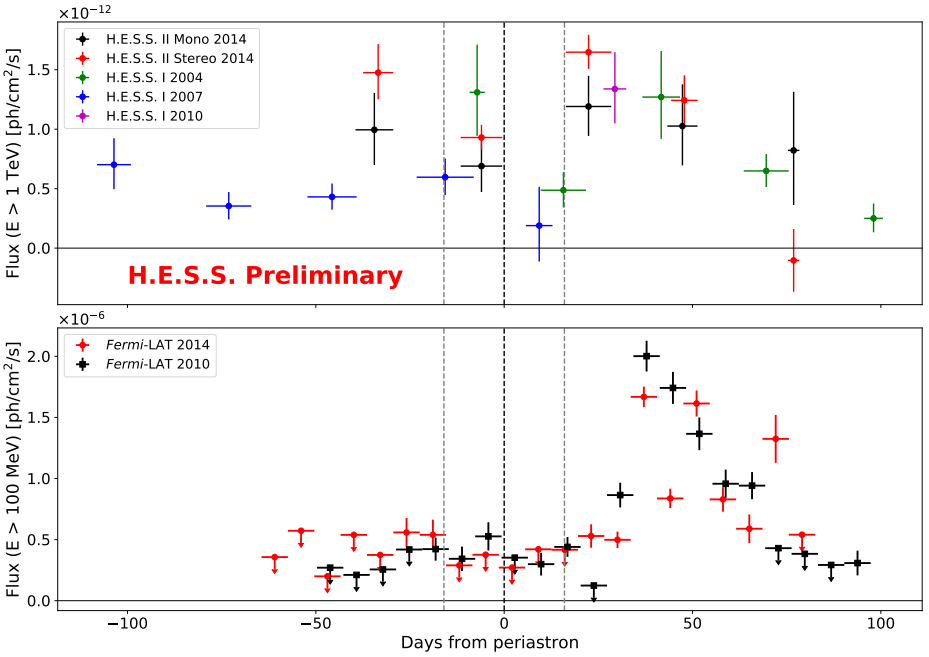

FIGURE 3.3: In the *top* panel the period-wise phase folded light curve of PSR B1269−63. The points are from the analysis of the H.E.S.S. II data in 2014 (red for STEREO and black for MONO) and the HESS I data collected during the previous observation campaigns in 2004 (green), 2007 (blue) and 2010 (magenta). The black dashed line indicates the time of periastron, while the grey dashed lines highlight the time of the disc crossing. Figure adapted from [115]. The *bottom* panel shows instead the light curve of the emission above 100 MeV as detected by the *Fermi*-LAT for the 2010/2011 passage (black points) and 2014 passage (red points).

3.2.1 The link with *Fermi*-LAT

The lower panel of Figure 3.3 shows the light curve of the gamma-ray emission for energies above 100 MeV. The data were analysed over a large interval before and after the periastron passage to have a good fit of all the background sources and were extracted from a square region with a side of 28 degrees. The fitting routine, done with a binned likelihood method, took into account all the sources detected in the 3FGL catalogue and the latest available background models for the galactic diffuse emission and the isotropic background (as done in Chapter 2 and explained also in Appendix C). The photon index obtained over the full time interval was 3.24 ± 0.08 with a flux above 100 MeV of $(5.2 \pm 0.2) \times 10^{-7}$ ph/cm^2/s. This index was fixed and used to derive the weekly binned light curve (the points were calculated only in case the TS of the source in the bin was

greater than 10, indicating a significance level of $\sim 3\sigma$)[3]. The result of the fit on the GeV flare itself is given in Table 3.1, where I used the same time intervals used in [130], comparing the 2011 and 2014 results. As was already becoming clear during the 2014 H.E.S.S. observation campaign, the so-called "Fermi flare" is in fact a recurrent event, with the 2014 outburst sharing many of the characteristics of the original one seen in 2010.

TABLE 3.1: Fit of the GeV flare of PSR B1259−63 during the 2010/11 and 2014 periastron passage.

Time interval	From periastron	Flux [ph/cm^2/s]	Ph. Index
MJD 55576 - 55585	31d-40d	$(1.97 \pm 0.11) \times 10^{-6}$	3.02 ± 0.09
MJD 55585 - 55615	40d-71d	$(1.11 \pm 0.06) \times 10^{-6}$	3.05 ± 0.08
MJD 55576 - 55615	31d-71d	$(1.31 \pm 0.05) \times 10^{-6}$	3.04 ± 0.06
MJD 56812 - 56823	31d-42d	$(1.30 \pm 0.06) \times 10^{-6}$	3.26 ± 0.09
MJD 56823 - 56851	42d-71d	$(0.96 \pm 0.05) \times 10^{-6}$	3.20 ± 0.10
MJD 56812 - 56851	31d-71d	$(1.04 \pm 0.04) \times 10^{-6}$	3.18 ± 0.07

The most important aspect here is the relation between the flux levels detected at GeV and TeV energies. For the first time, we have simultaneous H.E.S.S. and *Fermi*-LAT observations during the GeV flare, and the points show a high TeV flux during this interval.

In the H.E.S.S. light curve, there is an interesting phenomenon that will be hopefully confirmed by future observations. In the time interval between 30 and 40 days before the moment of the periastron, well before the first disc crossing, there is an unexpected flux enhancement not related to the emission at lower energies.

The analysis of the TeV data is still in a preliminary state. At the time of writing we envisage the realization of a more finely binned light curve of the H.E.S.S. observation where the trends will be clearer. Furthermore, we are in the process of producing a "stacked" phase-folded light-curve, where all the data taken during the various years will be folded together to study in more detail the periodicity of this source at TeV energies[4].

[3] Allowing the photon index to vary in the weekly light curve produced compatible results and did not give any statistically significant evidence of spectral variability.

[4] Some further preliminary updates were released at the ICRC2017 Conference and appeared in [131].

3.3 Conclusions

The observational campaign carried out by the H.E.S.S. Collaboration on PSR B1259−63 in 2014 had the chance of covering some of gaps left by the previous 3 periastron campaign. Even though it was not possible to cover the onset of the GeV flare, there were observations during the flaring stage that detected a high level of TeV flux, possibly related to the GeV flaring phenomenon. Furthermore, a completely unexpected high flux level was observed between 40 and 30 days before the periastron passage, in a time range where we are still far from the disc around the star LS 2883. The data presented in this chapter are, however, still preliminary and the results are being finalised at the time of writing and will be published in a forthcoming paper.

On the *Fermi*-LAT side, the flaring behaviour was again confirmed with the detection of a GeV flare ~ 30 days after the periastron. Even if there are some differences between the 2010/2011 flare and the 2014 one, there must be an underlying effect to trigger this event, although the origin of this emission is not completely clear yet. Regarding the brightening detected at TeV energies before the first disc crossing, there is no counterpart in the *Fermi*-LAT data, with the flux level of the source below the sensitivity limit of the instrument.

The observations of the future periastron events will be fundamental to confirm the emission pattern seen until now. Unfortunately, the visibility for the 2017 periastron passage was not optimal, although some observation time was granted to further investigate the flux enhancement before the first disc crossing. The periastron passage expected in February 2021 might be observed by the future Cherenkov Telescope Array (CTA) which would have a great visibility of the source from its location in South America (details in Appendix B). This new Cherenkov array will be more sensitive than the present ground based gamma-ray telescopes and will be able to cover a wider energy range, hopefully bringing more insights to understand the source of the emission from this particular binary system.

Chapter 4

Gamma rays in our vicinity: Solar Flares

In this chapter I describe the analysis of various Solar Flares, a research carried out with collaborators at the MPI-K (Heidelberg) where I contributed with the analysis of the recent data from Fermi-LAT and the validation of the analysis of the proton spectra. During its flaring events, our Sun is capable of releasing high fluxes of gamma-rays, emitted mainly through the decay of π^0 mesons originating from pp and pα interactions. In this chapter, the gamma-ray data were used to derive constraints on the proton spectrum using up-to-date cross sections and comparing the effects of these new cross sections to what has previously been published. This chapter refers to [132], which is a work in preparation.

4.1 Gamma-ray emission from the Sun.

As described in section 1.5.4, our Sun is capable of releasing an amount of energy up to 10^{32} erg, on time-scales of the order of hundreds of seconds during major flares. Part of the released energy is emitted in the form of gamma rays, involving different channels. While the emission at energies above 100 MeV can be linked to the decay of neutral pions (see Section 1.4), at lower energies other processes can contribute such as bremsstrahlung radiation from electrons and positrons (see subsection 1.3.2 for a discussion of the general process) that are produced in the decay of charged pions. Also, because of the presence of other nuclear species in the solar atmosphere, the flare spectrum also shows several gamma ray lines at ∼MeV energies superimposed on a broad nuclear continuum, e.g., see Figure 4.1.

If the emission were due only to proton-proton interactions, the dominant contributions to the gamma-ray spectrum would be limited to the *pion bump* (as visible in Figure 4.1) determined by the decay $\pi^0 \rightarrow 2\gamma$ plus the leptonic channel of the e^+e^- produced in the decay of charged pions. However, due to the fact that in the Sun's atmosphere there are also many other atomic nuclei, additional contributions have to be taken into account. For this reason, in the generation of the results that will follow, the following nuclei have also been included: H, ^{4}He, ^{12}C, ^{14}N, ^{16}O, ^{20}Ne, ^{24}Mg, ^{28}Si, ^{32}S and ^{56}Fe with abundances in number of particles with respect to hydrogen set to $n/n_H = 1;\ 8.41 \times 10^{-2};\ 2.45 \times 10^{-4};\ 7.24 \times 10^{-5};\ 5.37 \times 10^{-4};\ 1.12 \times 10^{-4};\ 3.47 \times 10^{-5};\ 3.31 \times 10^{-5};\ 1.38 \times 10^{-5};\ 2.82 \times 10^{-5}$ respectively, so as to match the Solar composition reported in [133].

A major effect of the inclusion of these nuclear interactions is the production of gamma-ray lines over a broad continuum. These lines are due to the de-excitation of unstable atomic nuclei, like the 2.223 MeV line of the neutron capture[1] or the 4.43 MeV line from the de-excitation of ^{12}C [69]. The continuum is instead a combination of different phenomena. The most important of these is the presence of unresolved, blended lines that make up the majority of the baseline flux level below 10 MeV. Below $\sim$ 20 MeV, the remaining continuum forms a broad peak related to the immediate decay of the *compound nucleus*, formed by the projectile which releases the whole energy into the target. At higher energies the emission is due to a shorter interaction between projectile and target. See Figure 4.1 for the result of an example calculation of this nuclear continuum emission. When dealing with nuclear reactions, another type of background can be important, especially if the spectrum of the accelerated nuclei is soft. As visible from the right panel of Figure 4.1 (computed for a soft, $\alpha = 4$ spectrum of accelerated nuclei), there is a significant contribution from the so-called *hard photon* component, which is thought to be due to incoherent bremsstrahlung between neutrons and protons [see e.g. 134–136]. Furthermore, as we have seen in section 1.4, pion production from protons is a threshold process that can only happen if the kinetic energy of the particles (T_p) is above $\sim$ 280 MeV. However, the pion production in the presence of heavier nuclei can happen for energies as low as $T_p \gtrsim 20$ MeV per nucleon [137, 138].

The calculation of the nuclear components at MeV energies was performed using the TALYS framework [139] (for the total production cross sections) and a Monte Carlo code developed by my collaborators following the prescriptions from [140]. The contributions to the gamma-ray spectrum at higher energies (above tens of MeV) can be calculated instead using recently developed parametrizations based on the most recent experimental

[1] In the process of deuterium production from the fusion of neutrons with ambient protons

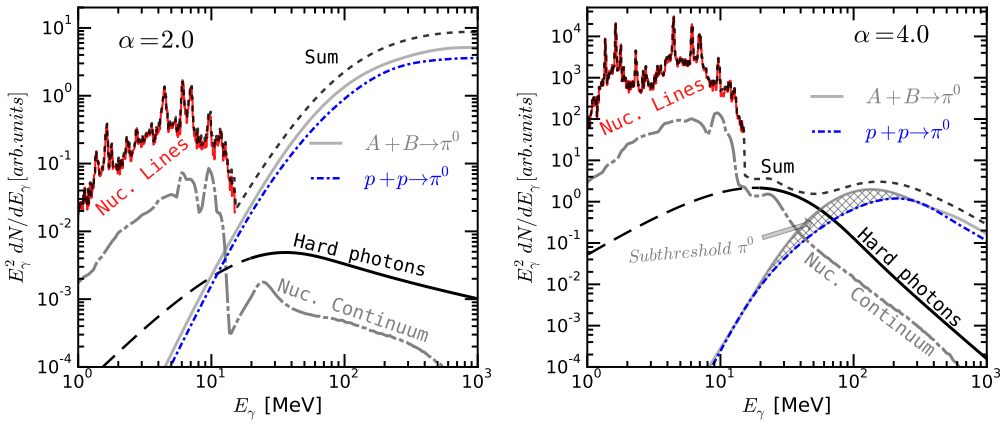

FIGURE 4.1: Nuclear gamma-ray continuum for a solar composition of elements for two different power-law primary fluxes with $\alpha = 2$ (left) and $\alpha = 4$ (right). The grey long dash-dot line represents the continuum radiation from nuclei once subtracted dominant component of unresolved lines. The black line shows the hard photon emission ($A + B \to \gamma$) which is valid only for $E_\gamma > 30$ MeV (and drawn as a dashed line for the extrapolation to lower energies). The gray line is the $A + B \to \pi^0 \to 2\gamma$ contribution from all nuclear interactions except for the $p + p \to \pi^0 \to 2\gamma$ which is shown separately with the thin blue dash-dot line. The difference in shape between $A + B \to \pi^0 \to 2\gamma$ and $p+p \to \pi^0 \to 2\gamma$ spectra in the energy range 20 – 200 MeV is due to the production of sub-threshold pions which is shaded in the right panel. The nuclear γ-ray lines are added for comparison.

data. The most important process, the gamma-ray emission from the decay of neutral pions in *pp* interactions has been parametrized by Kafexhiu et al. [34]. The production of charged pions (leading to the gamma-ray emission from secondary leptons due to bremsstrahlung and annihilation in flight) follows the parametrization given by [141]. The effects of nuclear interaction with the sub-threshold pion production and the hard-photon component follow instead the parametrization available in [142].

The gamma ray emission for energies $\gtrsim$ 100 MeV can be probed with high precision thanks to the *Fermi*-LAT measurements. Using the parametrizations listed above, we reconstruct the spectrum of the primary particles assuming a power-law distribution as a function of their kinetic energy.

4.2 The analysis of Solar Flare data

The fits are done on the published data for some of the brightest Solar Flares observed by the *Fermi*-LAT between 2011 and 2013. In detail they are: the Solar Flare of 2011 March 7 and June 7 [143], the one of 2012 March 7 [144] and the one of 2013 October 11 [145]. For the last two flares, the data are provided also in separate time intervals. The *Fermi*-LAT data of these flares show an extended emission lasting from $\sim$ 30 minutes (in

the case of SF20131011) up to several hours (for the other flares) with spectra peaked at ~ 200 MeV and high energy emission detected up to ~ 1 GeV.

4.2.1 Data fitting with Monte Carlo Markov Chains

The fits to obtain the proton distributions are performed using the joint application of a Markov Chain Monte Carlo (MCMC) and Bayesian inference. This implementation allows good control over all the steps of the fitting routine as well as a thorough exploration of the the parameter space in order to properly find the global fit minimum and calculate the associated uncertainties. As the name suggests, the method involves the use of Markov chains together with a Monte Carlo sampling. Using the definition reported in [146], a Markov chain is a sequence of elements in which the conditional distribution of the element X_{i+1} depends only on X_i, and it is fully determined by the initial point X_1 and the transition probability from X_i to X_{i+1}, which is the *same* for all values of i. The basic idea is to use Monte Carlo sampling to generate the Markov chain by sampling from a transition probability constructed so that the asymptotic distribution of the chain values X_i matches that of the Likelihood function, $\mathcal{L}(\lambda)$, that we are using for our fit. In other words, once the chain has "burned in" and no longer remembers the initial value of the chain, we are effectively sampling the Likelihood function: parameter sets, λ, in the parameter fitting space that give a bad fit (bad likelihood) will appear less frequently in the Markov chain. A simple algorithm to understand how this works in practice is the Metropolis-Hastings one [147]. We start from a point $\{\lambda\}$ in the parameter space and we generate a random step to a new position in parameter space $\{\lambda'\}$, using an easy-to-sample "proposal" distribution function that is symmetric in λ and λ' such as as a Gaussian in $\delta\lambda$. If the new position $\{\lambda'\}$ increases the Likelihood value with respect to $\{\lambda\}$ (so that $\mathcal{L}' > \mathcal{L}$), we accept the move and generate a new step starting from the new position. If instead the Likelihood value is lower, we generate a random number uniformly distributed between 0 and 1 (called r) and we proceed in the following way:

- if $r > \frac{\mathcal{L}'}{\mathcal{L}} \rightarrow$ reject the step and generate a new random step starting from $\{\lambda\}$
- if $r < \frac{\mathcal{L}'}{\mathcal{L}} \rightarrow$ accept the step and generate a new random step starting from $\{\lambda'\}$

This implementation ensures that we don't remain trapped in local maxima of the Likelihood function. At this point, this method can be associated to the Bayesian inference to derive limits on the parameters. What is done is to take the Bayes theorem

and apply it to our problem. The Bayes theorem states that [148]:

$$P(\theta|D) = \frac{P(D|\theta)P(\theta)}{P(D)}$$

where $P(\theta|D)$ is our *posterior* probability distribution of the parameter, $P(D|\theta)$ probability of the measure given the model (which comes from the Likelihood function), $P(\theta)$ is the *prior* probability distribution of the parameters that here was chosen to be an "uninformative" uniform distribution, and finally $P(D)$ is the normalization constant, called *evidence* that is nothing but $P(D) = \int P(D|\theta)P(\theta)d\theta$. What is most important is that if the MCMC is able to explore properly the parameter space, by looking at the final histogram of the distribution of each parameter, it is possible to infer the posterior probability distribution of the parameter and define confidence intervals on the possible values. Because this point relies on a proper and efficient exploration of the parameter space, which the Metropolis-Hastings often fails to do (e.g., if the Likelihood function implies that some of the fit parameters are strongly correlated), I chose to instead use the `emcee PYTHON` tool for the MCMC implementation[2]. This tool, described by Foreman-Mackey et al. [149], is based on the technique of the ensemble sampler with affine invariance [150], a method in which a set of parallel *walkers* explore in an effective way the parameter space updating their positions based on the knowledge of each others' positions: the next step of each walker is generated on the vector that connects the positions of the walker we want to move and another one randomly chosen in the "complementary set" of the remaining ones. This "stretch move" algorithm is illustrated in [150]. This method is also in the analysis routine used to cross check the proton spectra using the publicly available software, NAIMA [151].

In Figure 4.2, we report the outcome of the MCMC spectral fit of the proton distribution on the SF20110307 data, showing the distribution of the Monte Carlo sampling and the histograms representing the posterior distributions for the fitted parameters, which are extracted from the sampling of the total posterior distribution. From these histograms is possible to extract the confidence intervals associated to the fitted parameter and the reference value. In the fit results reported in this chapter, the parameter values are represented by the median of the histogram with uncertainties given by the 16^{th} and 84^{th} percentiles. If our Likelihood were Gaussian, these percentile values would represent the canonical 1σ error.

[2] `http://dan.iel.fm/emcee/current/` accessed on the 26/06/2017

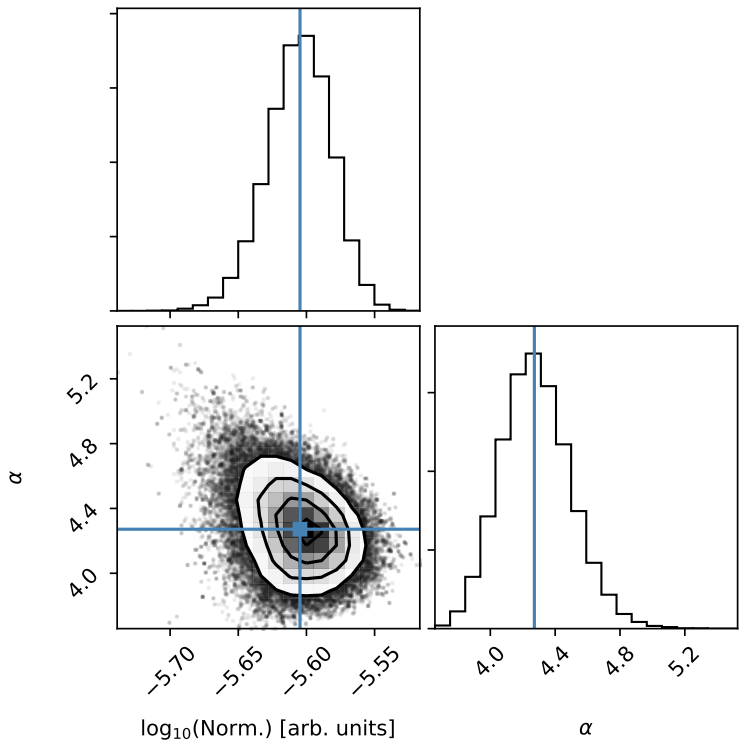

FIGURE 4.2: Corner plot of the MCMC fit on the SF20110307 data. The bottom left panel shows the distribution of the Montecarlo sampling as a density plot, while the top and right panels are the histograms of the posterior distributions for the logarithm of the normalization and the index of the fitting function. The blue lines indicate the median of the posterior distributions.

4.2.2 Fit results

The results of the MCMC scan are presented in Table 4.1 and visually in Figure 4.3 for the different time intervals of SF20120307. The fit of the proton spectrum reported in the original papers [143–145] makes use of a photon templates obtained from the cross sections derived in [152], while the new results presented here use the parametrization described in [34, 141, 142]. In the new analysis, the spectrum is slightly harder than the one obtained in the previous papers and this is even more evident if we consider a Solar composition for the target material. For SF20120307 in particular, where the data are available for different time intervals, it is possible to study the time evolution of the flare highlighting a trend towards a softening of the spectrum with time.

We have also tested the assumption of a primary particle distribution following a power-law with exponential cut-off. However, the small energy range of the available data does not allow a proper determination of the fit parameters. The main problem being

the degeneracy between the power-law index and the cut-off value[3]. This case is well illustrated in Figure 4.4: the data above 60 MeV can be fit without statistical significant differences by both power-law and power-law with exponential cut-off. The best way to break this degeneracy would be to increase the energy range of the fit, making use of the MeV data. Unfortunately, this information is not always available because of the lack of the necessary sensitivity of the GBM instrument for this type of measurements. In the particular case of SF20131011, the level of gamma-ray lines indicates a preference for a harder power-law.

TABLE 4.1: MCMC results for the primary spectrum parameter α for the selected Solar Flares observed by the *Fermi*-LAT. The analysis for a pure hydrogen composition are denoted by $p+p$, whereas, a solar composition of elements is denoted by "Solar". The "Literature" column quotes the index α values that are found in the literature. For the flare of the 2012 March 7, the various time interval are indicated with consecutive letters as in [144], while for the flare of 2013 October 11, intervals (c) and (d) correspond to the time intervals (7:16:40 - 7:35:00 UTC) and (7:08:00 - 7:35:00 UTC) respectively. From [132].

	Power-Law		
	$p+p$	Solar	Literature
Flare	α	α	α
SF20110307	$4.27^{+0.22}_{-0.20}$	$3.82^{+0.09}_{-0.08}$	$4.5^{+0.2}_{-0.2}$
SF20110607	$4.13^{+0.54}_{-0.43}$	$3.53^{+0.15}_{-0.12}$	$4.3^{+0.3}_{-0.3}$
SF20120307 (a)	$3.46^{+0.13}_{-0.11}$	$3.37^{+0.08}_{-0.06}$	$3.8^{+0.1}_{-0.1}$
SF20120307 (b)	$3.71^{+0.04}_{-0.04}$	$3.56^{+0.02}_{-0.02}$	$4.0^{+0.1}_{-0.1}$
SF20120307 (c)	$4.26^{+0.10}_{-0.06}$	$4.10^{+0.03}_{-0.03}$	$4.6^{+0.2}_{-0.2}$
SF20120307 (d)	$4.47^{+0.07}_{-0.07}$	$4.22^{+0.01}_{-0.01}$	$4.8^{+0.1}_{-0.1}$
SF20120307 (e)	$4.60^{+0.32}_{-0.27}$	$3.94^{+0.11}_{-0.12}$	$5.1^{+0.3}_{-0.3}$
SF20120307 (f)	$5.09^{+0.21}_{-0.13}$	$4.51^{+0.03}_{-0.03}$	$5.5^{+0.2}_{-0.2}$
SF20131011 (c)	$3.98^{+0.30}_{-0.24}$	$3.74^{+0.18}_{-0.18}$	$3.8^{+0.2}_{-0.2}$
SF20131011 (d)	$3.89^{+0.26}_{-0.23}$	$3.65^{+0.17}_{-0.17}$	$3.7^{+0.2}_{-0.2}$

4.3 The PASS 8 re-analysis

Due to the fact that the data used for the fit were published before the release of the latest *Fermi*-LAT IRFs, I performed a new analysis to assess the improvements using the most up-to-date tools for the analysis of the *Fermi*-LAT data focusing on two flares: the SF20110607 of the 7^{th} June 2011 and SF20131011 of the 11^{th} October 2013. These two flares were chosen because they are short and easy to analyse, given the fact that we did not need to properly track the movement of the Sun in the field of view [143]

[3]The fit of data on such narrow energy range makes it impossible to distinguish between a steep power-law and the cut-off region of a power-law function with exponential cut-off.

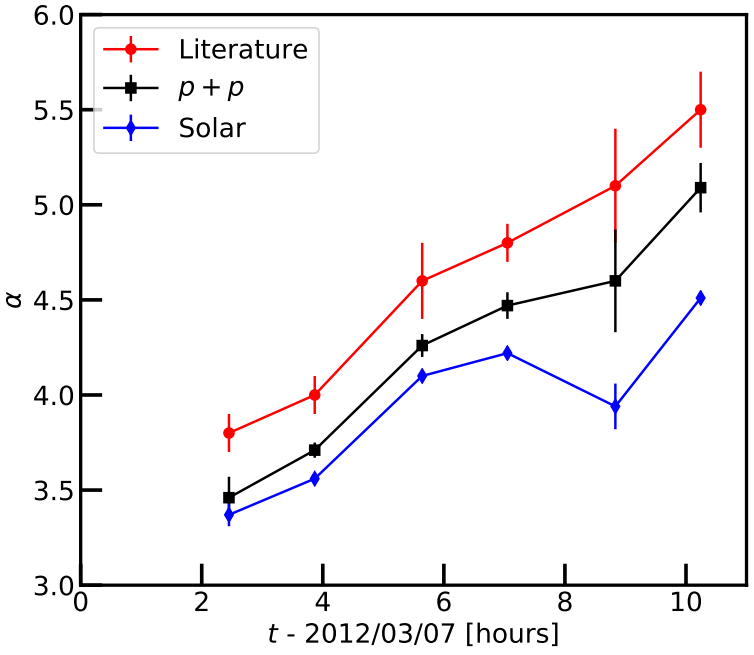

FIGURE 4.3: Comparison between the fit parameters for the different time intervals of the Solar Flare SF20120307 when fitting with a power-law function as a function of time. Adapted from [132]

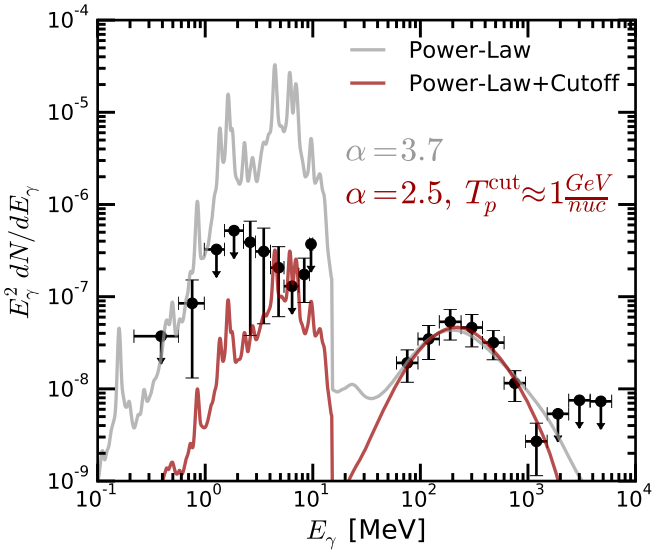

FIGURE 4.4: Spectrum from *Fermi*-LAT and *Fermi*-GBM for the SF20131011(c) interval from [145], with superimposed the results from the best fit model. The lines are from the calculation of the gamma-ray spectra assuming a solar composition of elements and using the best fit parameters obtained with the MCMC scan above 60 MeV data. The grey line correspond to a pure power-law primary spectrum, whereas, the red line correspond to a power-law with an exponential cut-off. The nuclear gamma-ray line spectrum below 10 MeV is calculated assuming the same primary particles spectra.

or use a dedicated analysis due to the saturation of the anti-coincidence detector [144]. The analysis was performed in an energy range between 60 MeV and 50 GeV on photons of SOURCE class (see Appendix C) using the same time intervals defined in [143] and [145]. The region of interest (RoI) analysed is a square region of 24 degree size centred on the position of the Sun during the time of the flare. For a better localization of the centroid of the emission, I only used the data above 100 MeV, where the *Fermi*-LAT has a better PSF using the standard tool `gtfindsrc`. During the flare SF20110607, the Sun was close to the projected position of the Crab pulsar (as shown in Figure 1.11), so the centroid was extracted from a circle with a radius of 5 degrees to avoid contamination.

In the re-analysis of the data, we made use of an extra feature allowed by the PASS8 reconstruction: the account for the energy dispersion matrix in the flux determination. This step has the double advantage of improving the reconstruction below 100 MeV and to reduce the systematic uncertainties[4].

In Table 4.2, I show the result of the binned likelihood fit on the re-analysed gamma-ray data, modelled with a power-law and power-law with exponential cut-off functions (the latter phenomenological function statistically favoured over a simple power-law)[5].

The SED points are computed following the procedure illustrated in [143]: fixing the power law index at 2 and leaving free the normalization in each energy bin. The SED for the 2011 flare can be seen in Figure 4.5 compared to the old results. With the new analysis there is a better determination of the SED compared to the published data. In particular the upper limit for $E > 1$ GeV is more constraining, which highlights a strong suppression of the gamma-ray flux above 1 GeV.

4.4 Conclusions

The analysis reported here demonstrates that the *Fermi*-LAT data are a great tool to constrain the spectrum of non-thermal particles produced by the Sun during flaring events. However, at the moment these limits are still very much model dependent and rely on a good knowledge of the gamma-ray production cross sections and the composition of the target material. The work presented in this chapter has shown how, using more precise cross sections, we can reconstruct spectra for the primary particles harder than what has been presented in the literature so far. Spectra that are even

[4] As reported in `https://fermi.gsf/c.nasa.gov/ssc/data/analysis/documentation/Pass8_edisp_usage.html` (url accessed on the 1/8/2018)

[5] The fits are on the photon distribution and not on the primary particles.

TABLE 4.2: Final values of the fit of the 2 solar flares that have been re-analysed with PASS 8 data. The time range for the analysis of the solar flare 2011 June 7 is 07:47:40UT - 08:23:40UT, whereas, for the solar flare 2013 October 11 are (a) 07:08:00UT - 07:35:00UT and (b) 07:16:40UT - 07:35:00UT. The parameter Φ_{100} indicates the flux above 100 MeV.

Spectral Parameters	Dataset		
	SF20110607	SF20131011(a)	SF20131011(b)
Power Law			
Φ_{100} [10^{-5} ph/cm^2/s]	2.62 ± 0.17	14.9 ± 0.4	22.7 ± 0.7
Γ	2.45 ± 0.07	2.35 ± 0.03	2.37 ± 0.03
Power Law with exp. cut-off			
Φ_{100} [10^{-5} ph/cm^2/s]	3.22 ± 0.21	18.4 ± 0.5	27.8 ± 0.8
Γ	0.00 ± 0.04	0.13 ± 0.17	0.22 ± 0.17
E_c [MeV]	103.6 ± 6.6	125 ± 11	129 ± 12

harder are instead required if the composition of the interacting particles resembles the one present in the solar atmosphere.

Some useful insight into the actual shape of the primary particle spectrum can come from the data in the low energy gamma ray band. Figure 4.4 shows the *Fermi*-LAT data for the SF20131011 (interval (c)) together with the flux points registered by the GBM instrument in the energy range between hundreds of keV and tens of MeV (from [145]). The lines superimposed are derived by extrapolating the fit to the *Fermi*-LAT data (grey for power-law and red for power-law with an exponential cut-off) to low energies after the inclusion in the calculation of the contribute of the gamma ray lines and the nuclear continuum. It is clear that the synergy between the two instruments on-board the *Fermi*-LAT can place strong constraints on the spectra of the primary particles accelerated in solar flares. In particular, having a longer lever arm of available data (from MeV to GeV) would help to break the degeneracy between simple power-law and power-law with exponential cut-off models.

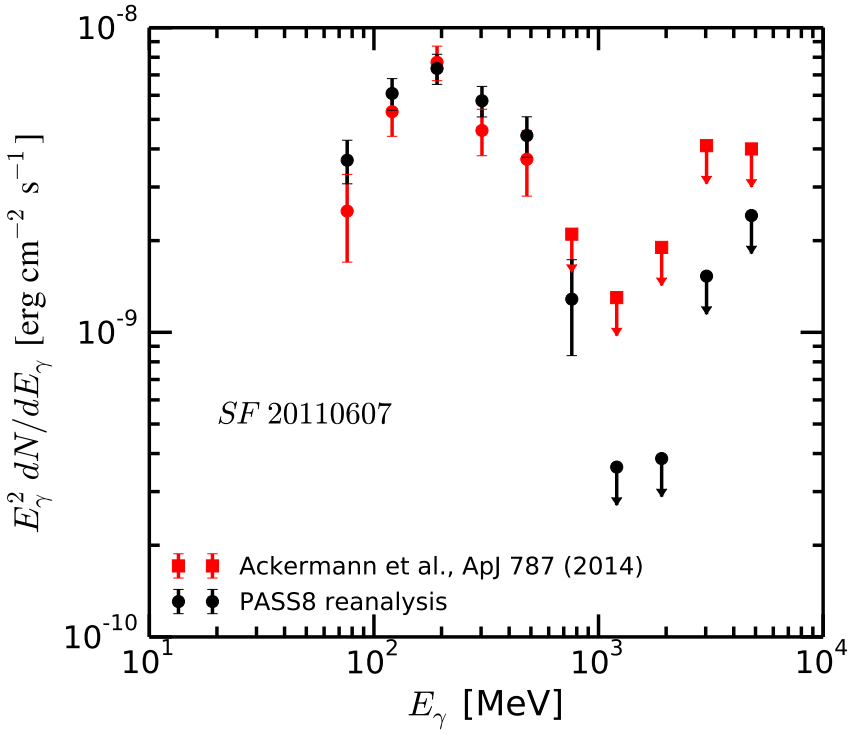

FIGURE 4.5: Comparison between the *Fermi*-LAT data of the solar flare of the 7^{th} of June 2011 reported in [143] (red squares) and the reanalysis made using the PASS 8 IRFs (black circles). Beside the reduction of the size of the errorbars, the upperlimits above 1 GeV are more constraining.

Chapter 5

The hard spectrum of Mrk 501: the importance of continuous monitoring

Long-term coverage of a single source helps greatly providing a detailed and unbiased characterization of its properties. The case I am presenting in this chapter refers to the blazar Mrk 501. This blazar is famous for being an highly variable gamma-ray emitter and for presenting hard spectra in the GeV energy range. Thanks to the presence of a long-term light curve and to the large energy range of the Fermi-LAT, it is possible to identify the presence of a different spectral component responsible for the emission above 1 GeV, confirming what has been previously suggested using a smaller set of data. Understanding the nature of the high-energy component would benefit greatly from the inclusion of simultaneous Cherenkov VHE data. However, the link between the observations of the Fermi-LAT and of high energy ground based telescopes is still not well defined given on one side the lack of statistics and on the other the lack of a continuous monitoring of the source. This is about to change, though, thanks to HAWC, which has a much higher on-source duty cycle, and FACT, which has focussed its observation strategy on the continuous observation of a small sample of sources. This has the advantage of providing the scientific community with an unbiased coverage of variable source at TeV energies. The material presented here will be part of a forthcoming publication.

5.1 A hard source

The blazar Markarian 501 (often indicated as MRK 501) is one of the most famous gamma-ray sources in the extragalactic sky. It belongs to the class of the HBL, High-peaked BL Lacs, meaning that the synchrotron peak of the SED is found in the X-ray band. It is one of the closest AGNs with a redshift $z = 0.034$, and one of the most well-studied TeV-blazars. The source owes its name to being part of the catalogue of the optically selected quasars with a bright UV continuum compiled by Markarian [153]. As a VHE emitter, it was first discovered by the Whipple telescope during the 1990s as the second extragalactic object in the sky (after its "sibling" MRK 421) [154]. At TeV energies, this source has shown some extreme flaring events, becoming tens of times brighter than during its quiescent state [see e.g. 155–157]. During these intense flares, the variability time-scale can be as short as few minutes [158, 159] with signs of a harder when brighter behaviour: the photon index goes from a value $\Gamma_{VHE} \sim 3$ and approaches $\Gamma_{VHE} \sim 2$ at the peak of the emission, implying a very flat SED that does not show any sign of intrinsic cut-off up to $E \sim 10$ TeV [157]. At High Energy (100 MeV $<$ E $<$ 100 GeV) the source is clearly detectable by the *Fermi*-LAT which has opened the HE window for MRK 501[1].

5.2 Prior evidence for multiple components

Since the start of the *Fermi*-LAT observation of this AGN, there have been various claims of a very hard spectra seen in the HE energy range. The event that started the quest for these extremely hard components in the spectrum of MRK 501 was a TeV flare detected by the VERITAS telescopes in 2009 [156]. A follow-up analysis of the *Fermi*-LAT data performed by Neronov et al. [160] showed the possibility of a photon index for energies above 10 GeV of $\Gamma = 1.1 \pm 0.2$. Later on Shukla et al. [161], looking at a long dataset of *Fermi*-LAT data, have confirmed the presence of very hard spectra for energies above 10 GeV. These findings motivated a search for emission models that would be able to accommodate such observations. This is an important issue, given the fact that the theory of *Diffusive Shock Acceleration* (DSA) cannot explain photon indices $\Gamma < 1.5$[2]. Different models have been proposed to overcome this problem, requiring something more involved than a simple *one-zone SSC* approach which has very often been used to

[1] The EGRET instrument, the *Fermi*-LAT predecessor, was not sensitive enough to detect MRK 501.

[2] In DSA, primary particles are produced with a power-law distribution with index $p = -2$ for differential flux (dN/dE). When radiating via e.g synchrotron or IC processes, the power-law index of the gamma-ray differential flux will be $-\Gamma = (p+1)/2 - 1 = -1.5$ in the hardest case

describe the broad-band emission of BL Lacs. The proposed solutions mostly go towards scenarios with multiple components: multiple blobs with stochastic acceleration that leads to Maxwellian-type distributions and hence very hard spectra [162, 163]; presence of a multi-zone scenario with a more stationary component that originates from a shock inside the jet plus a more impulsive and hard component coming from the base of the jet [161]. Solutions involving hadronic models have also been put forward where the hard spectra arise from the secondary emission of π^0 decays produced in $p\gamma$ interactions between the protons accelerated in the jet and synchrotron photons [164].

5.3 New *Fermi*-LAT evidence for two emission components

In this chapter, I am using the *Fermi*-LAT data collected from the beginning of the mission in August 2008 till the end of July 2015 in the energy window 100 MeV – 500 GeV. The idea is to take full advantage of the long temporal coverage and the wide energy range, to analyse the statistical properties of the source emission in different activity states, in order to find further proof of the presence of different components. Shukla et al. [165] have already shown, on a shorter time-scale, some hints of different components in the *Fermi*-LAT energy range by finding distinct spectral behaviour below and above an energy of 2 GeV. Furthermore, recent radio observations have found an indication of a separate off-axis jet structure of MRK 501, though it was not possible to link the presence of this new morphological feature to the gamma-ray emission [166].

In a first analysis, I divide the energy range in a lower and higher interval, with a separation at 10 GeV, a value previously assumed when looking for hard spectra. To investigate the behaviour of the source in these two energy ranges, I derive a light-curve of the emission using a 28-day binning. The procedure requires first a full analysis of the entire time interval in each energy range (the results are reported in Table 5.1) using a standard type of analysis to determine the correct parameters of all the background sources that appear in the region of interest of the analysis (see e.g. Appendix C for details on the production of light curves). The 28-day light-curve is obtained through a new likelihood fit in each time interval. To correctly model the sources in the field of view, I leave free to be varied the normalization of all the sources which are flagged as variable ($\mathrm{TS}_{var} > 72.44$, indicating a 99% probability for the source to be variable) in the 3FGL catalogue [106]. This is to avoid the possibility that the flux of MRK 501 would be wrongly reconstructed due to a flare of a nearby source. The emission from MRK 501 is modelled with a power-law function with both normalization and photon

TABLE 5.1: Fit results for the low ($E < 10$ GeV) and high ($E > 10$ GeV) energy band of the time averaged *Fermi*-LAT data.

Parameter	100 MeV - 10 GeV	10 GeV - 500 GeV
Norm. [ph/cm^2/s/MeV]	$N_0 = (2.50 \pm 0.04) \times 10^{-12}$	$N_0 = (2.6 \pm 0.1) \times 10^{-14}$
Index	$\Gamma = 1.69 \pm 0.02$	$\Gamma = 1.82 \pm 0.05$
Energy scale [MeV]	2055	27580
Int. Flux [ph/cm^2/s]	$N_0 = (5.7 \pm 0.01) \times 10^{-8}$	$N_0 = (1.95 \pm 0.08) \times 10^{-9}$
TS source	16841.5	5651.3

index left free to be varied in each interval. To compute a flux point, a TS value of at least 10 is required, ensuring a $\sim 3\,\sigma$ detection in each time interval. The light-curves for both the energy ranges is shown in Figure 5.1. The choice of a bin-size of 28 days is driven by the need of having enough photon counts in each time interval, even for energies above 10 GeV. While this analysis can be able to track slow, long-term changes in the flux level, it lacks the time resolution to study fast flaring activity.

From Table 5.1 it is already clear that the photon indices in the low and high energy band are incompatible over the full dataset, indicating the possibility of a different origin. Through a study of the correlation between the different energy bands, I show next how the data can be used to separate different components responsible for the high energy emission in MRK 501.

5.3.1 Comparison of the emission above and below 10 GeV

The first step applied to the data is a cleaning routine, requiring a TS value of at least 25 ($\sim 5\,\sigma$) and the removal of data-points where the power-law parameters cannot be fully determined (e.g. photon indices with unrealistically small error bars and flux points compatible with 0 within the 1σ error bar). Furthermore, for a meaningful comparison between the high and low energy dataset, only the time intervals where the condition to retain a data point is satisfied in both energy ranges are kept, leaving us with a total sample of 69 points.

Figure 5.2 shows the correlation plots between the fluxes and the photon indices in the high and low energy range. When considering the flux-flux plot (Figure 5.2a), we observe a mild correlation between the datasets, with a Pearson's coefficient of 0.31. This value does not take into account the presence of the uncertainties in the flux level. For this reason, a dataset of 300 new light-curves is generated in which the flux value is taken from a Gaussian distribution with mean in the original point and width given by the uncertainty on the flux value. Using these fake-datasets, under the assumption of

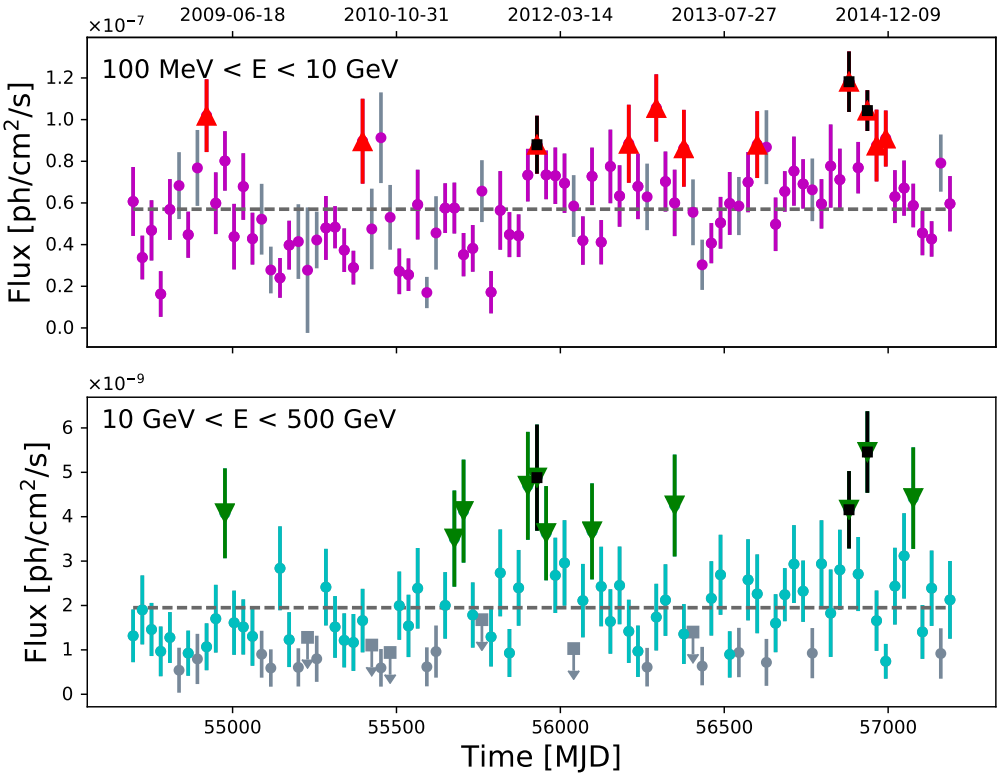

FIGURE 5.1: Light-curve of MRK 501 in two energy ranges, binned on 28-day intervals. The *upper* panel shows the flux between 100 MeV and 10 GeV. The time bins where the flux is above the 84^{th} percentile of the distribution are marked in red using upward triangles. The *lower* panel shows the corresponding light-curve in the higher, 10 GeV - 500 GeV, energy band, where now the fluxes above the 84^{th} percentile are marked with green downward triangles. The three data-points that present high flux in both energy bands are marked with black error bars. The grey dashed lines indicate the average flux in the lower and higher bands. Each coloured data-point in the light-curve was detected with a 5σ confidence level, while the grey circles have a TS value between 10 and 25. Upper-limits are marked with grey squares. In the upper panel, the points that do not have a clear detection (TS$\geq$ 25) in the higher energy range are marked by a magenta point with grey error bars.

an absence of intrinsic correlation, it is possible to compute a distribution of Pearson's coefficients with $r = 0.17^{+0.12}_{-0.14}$ where the uncertainties on the r value are in terms of the 16^{th} and 84^{th} percentiles of the distribution of the sample made of these 300 elements[3]. The photon indices of the two energy ranges, shown in Figure 5.2b, instead appear completely uncorrelated.

The first part of the analysis examines whether the emission of MRK 501 can be explained with a single component, especially during high flux states. The threshold for a state to be defined as high is set to be the 84^{th} percentile of the flux level distribution in

[3]the 16^{th} and 84^{th} percentile are the intervals corresponding to the canonical $1\,\sigma$ interval for a normal distribution.

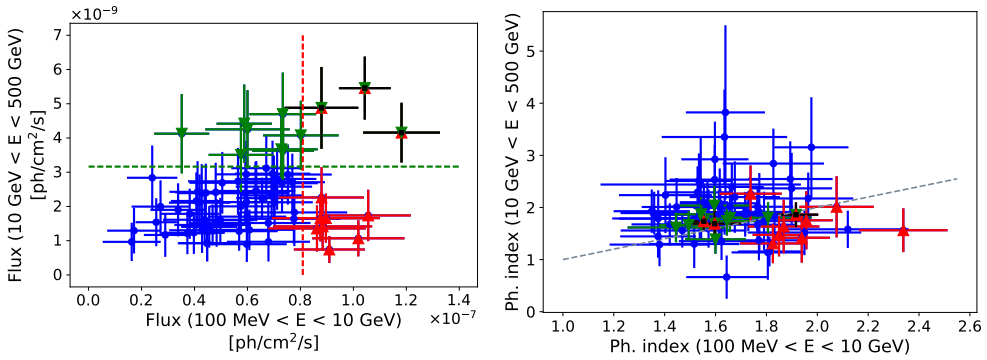

(A) Flux - flux correlation (B) Index - index correlation

FIGURE 5.2: Scatter plot of the flux below 10 GeV and the flux above 10 GeV (*left* panel) and index-index correlation (*right* panel). The red and green points refer to the points where the flux is above the 84^{th} percentile of the flux distribution in the energy range below and above 10 GeV, respectively. In the right panel the grey dashed line represents a perfect, 1:1 correlation.

each band. This gives us 11 high flux intervals for the low energy sample, and another 11 for the high energy one. The fluxes at the corresponding thresholds are:

- 84^{th} percentile for $E < 10$ GeV: 8.09×10^{-8} ph/cm^2/s
- 84^{th} percentile for $E > 10$ GeV: 3.16×10^{-9} ph/cm^2/s

The high state time intervals are indicated with a darker colour in Figures 5.1, 5.2a and 5.2b. The 3 time intervals where both the low and high energy datasets are in high states are indicated in black in the previous figures. Figure 5.2a illustrates the possibility to visually separate the high state of the low energy band ($E < 10$ GeV) into two components: one correlating with the high state in the high energy band and another one apparently independent from it: a possible indication of a different origin.

To quantify this effect the distance between each point of the high state of the low-energy band (red points in Figure 5.2a) from their centroid is computed. If the points come from a single population, the histogram of these distances would show a compact structure, while it would be less compact in the case of two components. The computation of the centroid position involves first a rescaling of each data point, renormalizing their value and variance so as to take into account the different flux scales between the energy bands, and performing a weighted mean in the x and y direction. After the computation of the centroid, a calculation of its distance from each point in terms of standard deviations is performed, as shown by the blue histogram in Figure 5.3a. To assess if the distance distribution shape could be explained as a fluctuation from a single population, I simulate

a 2D distribution of 10^6 points having the same mean and variance as the original flux-flux distribution and an intrinsic correlation coefficient so that, when applying cuts on the minimum flux observed, the value would be the same as that of the original data points. This cut in the flux consists of excluding from the simulated data all the points whose flux is below the minimum of the original *Fermi*-LAT distribution, in order to reproduce a sensitivity limit. The association of errorbars for each point i, is done according to the relations:

$$\sigma_{F_i} = 0.45 \left(\frac{F_i}{F_{min}} \right)^{-\frac{1}{2}} F_i \tag{5.1}$$

for the low energy direction, and

$$\sigma_{F_i} = 0.636 \left(\frac{F_i}{F_{min}} \right)^{-\frac{1}{2}} F_i \tag{5.2}$$

for the high energy direction. In these expressions, the normalization values are obtained through a fit of the original *Fermi*-LAT data, while the $\frac{1}{2}$ comes from the usage of a Gaussian approximation (used in the *Fermi*-LAT tools to obtain the uncertainty in the flux value). Applying the same procedure for the centroid distance to the simulated points, I obtain the distribution represented by the green histogram in Figure 5.3a. Adopting a Kolmogorov-Smirnov test on the similarities between the two histograms[4], we obtain a probability value of 21% for the two histograms to belong to the same population. However, these results are obtained using the assumption of Gaussian errors on the flux. This approximation is correct only in the case of a large number of photons, but incorrectly reconstructs the flux uncertainty in the case of low counts, as is the case for the high energy light-curve, where there are typically less than 10 photons per bin. Adopting the approximation developed by Gehrels [167, equations 10 and 14], I associated with each flux point its Poissonian uncertainty, given the number of photons attributed to the source in each time interval by the likelihood fit. Similarly, a Poissonian uncertainty is associated to each of the simulated values (for fluxes above 10 GeV) according to the relations:

$$\sigma^{+}_{F_i} = 1.12 \left(\frac{F_i}{F_{min}} \right)^{-0.66} \tag{5.3}$$

for positive uncertainty and

$$\sigma^{-}_{F_i} = 0.60 \left(\frac{F_i}{F_{min}} \right)^{-0.46} \tag{5.4}$$

[4]using the SCIPY routine documented `ks_2samp` documented at `https://docs.scipy.org/doc/scipy/reference/generated/scipy.stats.ks_2samp.html` accessed on 18/03/2018

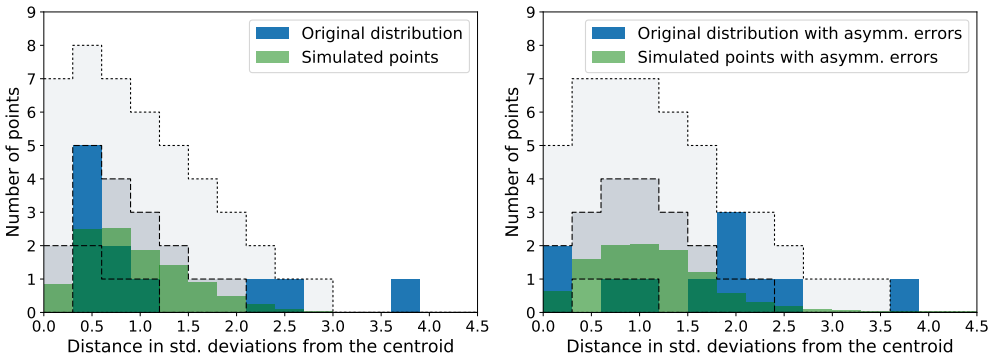

(A) Symmetric errors (B) Asymmetric errors

FIGURE 5.3: Distribution of the distances between the points of the low energy, high flux dataset and their centroids in units of standard deviations. The original points are indicated with the blue histogram, while the simulated ones with the green one. The left panel refers to the default case with symmetric errorbars, while the right plot is the one after the application of the Poissonian uncertainties in the high energy direction. The dashed and dotted lines indicate the 1σ and 3σ contours respectively, obtained from a sample of 10000 sets of 11 points extracted from the simulated distribution.

for negative uncertainty, where now both normalization and exponent are derived from a fit to the original data. Using the new uncertainties, the procedure used before has to be modified to take into account the asymmetric errors for each data-point. The procedure to correctly deal with data-points with asymmetric errors goes through the reconstruction of a reasonable likelihood function that could have produced those values. In our case, given the Poissonian origin of the asymmetry, I chose to use a Gaussian function with variable width, linear in the variance, applying the algorithms to combine values and errors as described by Barlow [168]. The outcome is the histogram shown in 5.3b, where the Kolmogorov-Smirnov tests gives a probability of 8.6×10^{-3} for the two histograms to come from the same population: a significance value for a new component between 2 and 3 σ.

5.3.2 Further analysis on the flux-index correlation

The analysis of the correlation between flux and index in each energy band reveals other interesting facts. To investigate further the mild significance value found for the presence of a different component in the energy range 100 MeV – 10 GeV, I again subdivide this energy range to identify possible different behaviour in each energy decade: 100 MeV – 1 GeV; 1 GeV – 10 GeV and 10 GeV – 500 GeV; computing a 28-day light curve also for the first two datasets. To reduce the possible contamination in the lowest energy bin

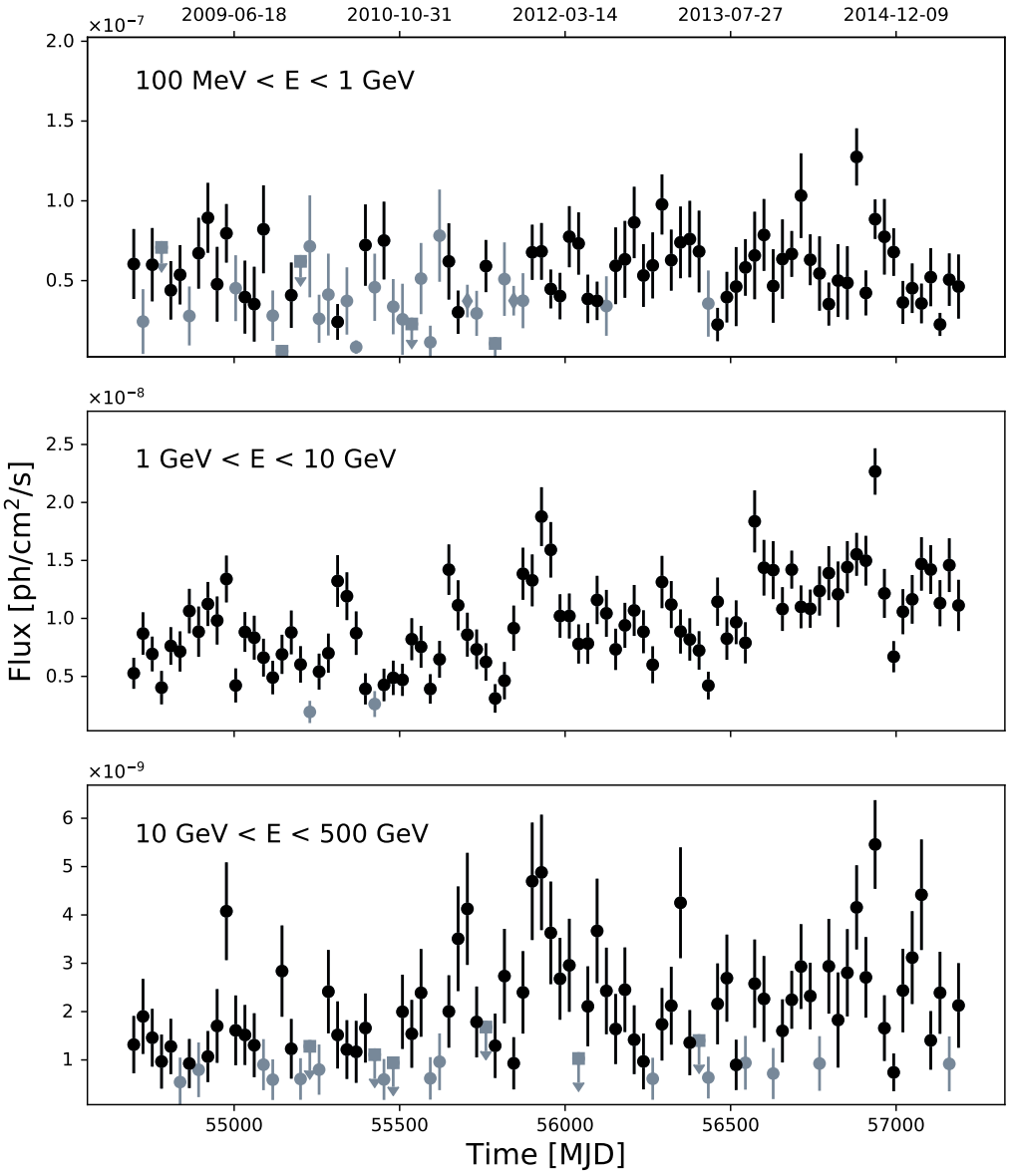

FIGURE 5.4: Comparison between the light curves at each energy band: 100 MeV - 1 GeV (*top* panel); 1 GeV - 10 GeV (*middle* panel) and 10 GeV - 500 GeV (*bottom* panel). The black points are the ones where the detection had a TS value of at least 25 (5σ). The grey circles are data points that had a TS value between 10 and 25 (~ 3 and $\sim 5\sigma$) and the grey diamonds are points flagged as problematic (upper panel only). The grey squares are upper limits computed in the case the source had a TS value below 10 (3σ).

(100 MeV–1 GeV, the one with the worst PSF), the photon index of variable source are also left free to be varied in the light-curve computation.

The full comparison between the components is reported in Figure 5.4. One of the first aspects to notice is that the lowest energy band has a lower flux variability compared to the other two, as visible after computing the fractional variability of the source. This

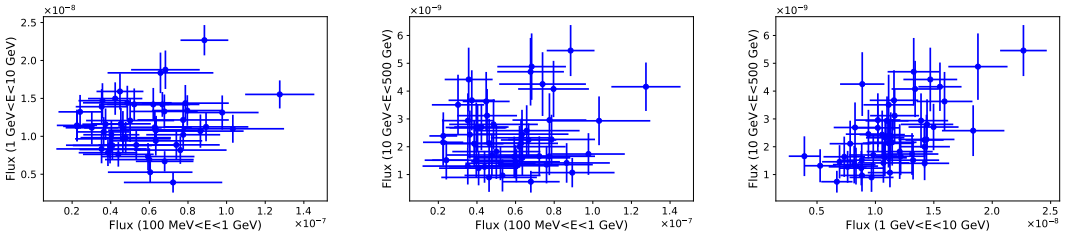

(A) [0.1-1] - [1-10] GeV (B) [0.1-1] - [10-500] GeV (C) [1-10] - [10-500] GeV

FIGURE 5.5: Flux-Flux correlation between the three energy bands. The 51 data-points were taken from the intersection between all the three energy bands. There is significant correlation found only in the rightmost plot.

quantity is expressed as [169, eq. 10 and B2]:

$$F_{var} = \sqrt{\frac{S^2 - \overline{\sigma_{err}^2}}{\overline{f}^2}} \tag{5.5}$$

with an uncertainty that can be computed as:

$$\sigma_{F_{var}} = \sqrt{\left\{\sqrt{\frac{1}{2N}}\frac{\overline{\sigma_{err}^2}}{\overline{f}^2 F_{var}}\right\}^2 + \left\{\sqrt{\frac{\overline{\sigma_{err}^2}}{N}}\frac{1}{\overline{f}}\right\}^2} \tag{5.6}$$

where S^2 is the variance of the flux, $\overline{\sigma_{err}^2}$ is the average error on the flux, $\bar{f}$ is the mean flux and N is the number of points in the light curve. The fractional variability's role is to state how much of the flux variance cannot be explained by the measurement uncertainties, giving an indication of the true variability of the source. Neglecting the upper limits, the fractional variability in each band is:

- 100 MeV - 1 GeV: $F_{var} = 0.15 \pm 0.08$
- 1 GeV - 10 GeV: $F_{var} = 0.35 \pm 0.02$
- 10 GeV - 500 GeV: $F_{var} = 0.41 \pm 0.05$

with a clear detection of variability for the energy bands above 1 GeV. It is also worth noting that the best determination of the source flux is obtained in the middle energy range, where the *Fermi*-LAT can count on the combination of a reasonable level of statistics and the peak of the effective area (refer to Figure 1.14a).

Figure 5.5, shows the correlations plots between the fluxes at the different energies. The only one that seems to have a significant correlation is the one between the two bands

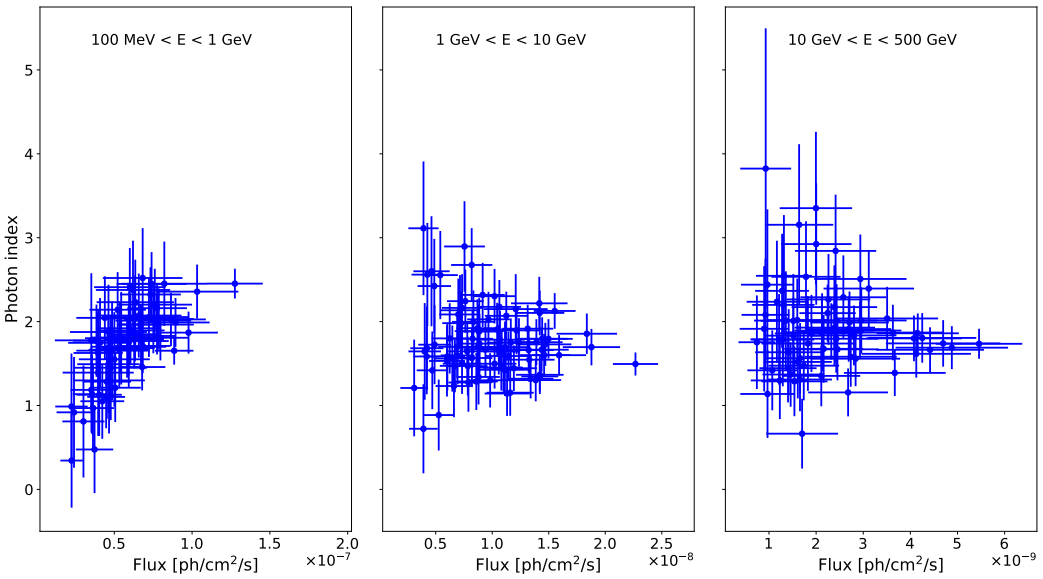

FIGURE 5.6: Correlation plot between flux level and photon index for each energy band. The *left* panel refers to the energy band 100 MeV - 1 GeV, the *middle* panel to the interval 1 GeV - 10 GeV, in the *rightmost* one to the energies between 10 GeV and 500 GeV. For each plot only the points for each data set with TS> 25 were taken into account.

above 1 GeV shown in the panel 5.5c. For these two energy windows, the Pearson's correlation coefficient is 0.63 (with associated to a chance probability of $\sim 10^{-6}$) and after running the randomizing test, can still be obtained a distribution of correlation coefficients $r = 0.45^{+0.09}_{-0.10}$ without any prior assumption on the intrinsic correlation of the simulated points. This means that the correlation is robust against the flux uncertainties, even in the conservative hypothesis in which the simulated points are originated from a symmetric, uncorrelated Gaussian. For the other two plots shown in Figures 5.5a and 5.5b there is instead a complete lack of correlation.

The similarity between the two energy bands above 1 GeV is not limited to the statistical correlation between the fluxes, but it can also be seen by looking at the *flux-index* plot in Figure 5.6. The interesting aspect that arises from this analysis is the presence of a different behaviour between the lowest energy band and the others. At low energy, we find a correlation between the flux and photon index, with a Pearson's coefficient of 0.72 ($0.37^{+0.10}_{-0.09}$ after taking into account the error bars without correlation assumption) and extremely hard spectra at low fluxes. What is instead remarkable is what happens at energies above 1 GeV. In this case, the *flux-index* plot shows a convergence of the photon index to values between 1.5 and 1.8, with a spread that increases at lower fluxes. instead

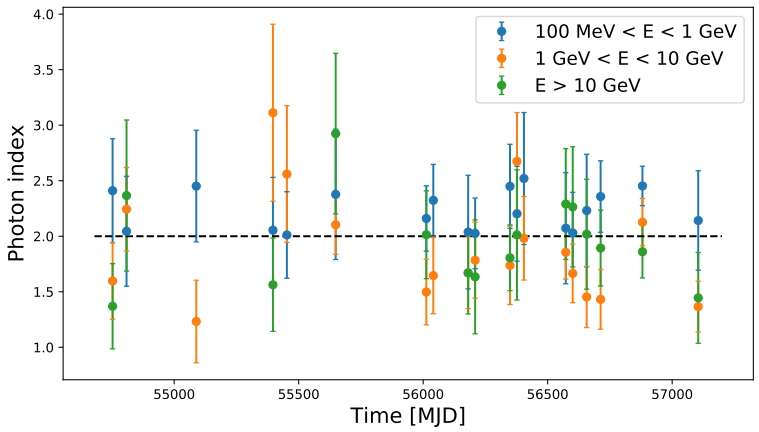

FIGURE 5.7: Comparison between the photon indices in three energy bands for time intervals in which the photon index in the energy band 100 MeV – 1 GeV is greater than 2 (implying a soft spectrum). The blue, orange, and green points are the photon indices measured in the energy range 100 MeV – 1 GeV, 1 GeV – 10 GeV, and 10 GeV – 500 GeV, respectively.

In Figure 5.7, given the different behaviour of the relation between photon index and flux, I have explored the possibility of having a convex shape in the SED of the source. The data are selected to retain only the points in which the photon index in the lowest energy band (100 MeV – 1 GeV) is greater than 2 finding 19 time intervals. Despite having in some cases a harder photon index, the size of the uncertainty on the measure does not allow to draw strong conclusions in this regard.

5.4 Conclusions and future prospects

Despite the intense observational campaigns on MRK 501, this source continues to be extremely interesting, bringing new elements to the puzzling nature of its gamma-ray emission. In this chapter, I have shown how, using a long term dataset, it is possible to identify hints of the presence of two different components in the energy range between 100 MeV and 10 GeV. From the analysis of the flux and photon index variations, it is also found that all the emission between 1 and 10 GeV and above 10 GeV is highly correlated, suggesting a similar origin, with an interesting convergence of the photon index to values close to 1.5 when the source is in a high flux state, while in a low flux state the source can present both harder and softer indices. This seems to suggest that the actual separation between the components contributing to the high energy spectrum of the Mrk 501 occurs at $\sim$ 1 GeV. With more precise measurements of the photon index, it could also be possible to study the presence of "V-shaped" features in the SED, which

would arise from having a soft component at low energy (photon index > 2) and a hard one at higher energy (photon index < 2).

The detailed analysis of these data was possible thanks to the continuous coverage of the gamma-ray sky from the *Fermi*-LAT. What remains still partly unknown is the behaviour of this source at the highest energies. In the TeV regime, MRK 501 has shown indications of the *harder when brighter* phenomena, in association with flaring events, with a photon index value of ~ 2 during flares [157]. A behaviour which is opposite of what seen for $E < 1$ GeV. The coverage is however, still too sparse to be able to connect the emission at tens of GeV to what has been detected in the VHE window and possible observational biases should be taken into account.

Fortunately, the near future, we should start to see the fruits of VHE monitoring programs set up to fill this gap. In particular there are 2 types of instruments that will play an important role in improving our monitoring capabilities. One is FACT (First G-ADP Cherenkov Telescope)[5] [170, 171, design and performances]. This is a Cherenkov telescope with a reflective surface of ~ 10 m^2, located in the Canary Islands, on the same site of the MAGIC experiment. Because of its improved detectors, this telescope can operate even with strong moonlight, i.e., it has a higher on-source duty cycle than H.E.S.S., and it is currently carrying out an important monitoring program on a selection of gamma-ray sources of which the blazar MRK 501 is one of the most relevant[6]. The point is to be able to characterize the source at TeV energies in an unbiased way, reconstructing its emission at *all* flux states. With a threshold of ~ 750 GeV, this telescope's energy coverage sits just above the energy range of the *Fermi*-LAT, complementing its lower energy coverage.

The other relevant monitoring instrument will be HAWC (described briefly in 1.7). Because of its design, this instrument is actually similar to the *Fermi*-LAT, in terms of its ability to continuously scan of the sky, regardless of the Moon or even the day-night cycle. Its sensitivity is best at energies ~ 10 TeV and, even if this sensitivity is not high enough to detect the Mkn 501 on short time-scales when it is in its quiescent state, it still has very powerful monitoring capabilities, e.g., it could catch a powerful flare seen by *Fermi*-LAT that would be completely missed by the imaging air Cherenkov telescopes.

These monitoring programs will be extremely important for the advancement of the variability studies at VHE.

[5] `http://www.isdc.unige.ch/fact/` - accessed 25/05/2017
[6] `http://www.fact-project.org/monitoring/` - accessed 25/05/2017

Chapter 6

Exploring cut-off spectra with high photon statistic

In this chapter I describe the impact that future ground-based telescopes will have on the determination of the cut-off parameters of bright sources detected with the Fermi-LAT. The shape of the cut-off region, for example, can give important insight on the balance between acceleration and cooling processes. The advent of CTA will significantly improve the amount of statistics available above 20 GeV. Using the simulated IRFs for the future instrument, I computed the expected signal from 3 of the brightest sources detected by the Fermi-LAT. This chapter refers to the work published in [172] and discusses some recent developments using H.E.S.S. data on the blazar 3C 279.

6.1 The importance of the cut-off region

The shape of the observed spectra that we detect in gamma-rays can be generally described by a power-law function with a modified exponential cut-off[1]

$$\frac{dN}{dE} = N_0 \left(\frac{E}{E_0}\right)^{-\Gamma} \exp\left[-\left(\frac{E}{E_c}\right)^{\beta_\gamma}\right] \tag{6.1}$$

where E_0 indicates the energy scale of the power-law region; Γ represents the power-law index of the particles, E_c characterizes the position of the cut-off energy, while the parameter β_γ determines the steepness of the cut-off (stretched for $\beta_\gamma < 1$, compressed for $\beta_\gamma > 1$).

[1] other functions that are often used are broken power-laws and log-parabolas.

The importance of determining the shape of the cut-off region in the gamma-ray spectrum is directly connected with the cut-off region in the energy distribution of the primary particles. In standard scenarios, the competing processes of acceleration and cooling are the ones that determine the give cut-off spectrum of the primary particles, and consequently they affect the final gamma ray spectrum that arises from the interaction processes. To avoid confusion I will call β_γ and β_e the cut-off parameters for photons and primary particles respectively.

In the following section I am using the framework of the second order Fermi acceleration in order to derive simple analytical expressions to retrieve the cut-off shape, keeping in mind that these are general results that can also be obtained with the theory of Diffusive Shock Acceleration theory.

The key parameter that determines the effectiveness of the acceleration mechanism is the momentum diffusion coefficient, which depends on the momentum itself p and on the power-law index of the fluctuations of the magnetic field q. It can be written, together with the escape time as (some more details are reported in Appendix A):

$$D_p(p) = D_* \left(\frac{p}{p_*}\right)^q \qquad \tau_{esc} = \tau_* \left(\frac{p}{p_*}\right)^{q-2} \tag{6.2}$$

where D_*, τ_* and p_* are normalization constants. On the other hand the dependence of the radiative cooling processes can be stated as:

$$\tau_{cool} \propto p^r \tag{6.3}$$

To find the exact shape of the primary spectrum, it is necessary to solve the transport equation (see equation (A.14) in Appendix A):

$$\frac{\partial f}{\partial t} = -\frac{1}{p^2}\frac{\partial}{\partial p}\left\{p^2\left[f\frac{p}{\tau_{cool}(p)} - D_p(p)\frac{\partial f}{\partial p}\right]\right\} - \frac{f}{\tau_{esc}(p)} + \frac{S(p,t)}{4\pi p^2} \tag{6.4}$$

6.1.1 Solution for Bohm diffusion without losses

Solving (6.4) in the Bohm case ($q = 1$) with no radiative losses, gives a distribution of particle energies that has a simple exponential cut-off with $\beta_e = 1$. This case can be demonstrated easily enough. For the case of a steady state, loss-free solution, and

assuming a single δ injection[2], equation (6.4) can be rewritten as:

$$\frac{1}{p^2}\frac{\partial}{\partial p}\left(p^2 p \frac{D_*}{p_*}\frac{\partial f}{\partial p}\right) - \frac{f}{p^{-1}\frac{p_*}{\tau_*}} = 0 \tag{6.5}$$

where the dependences on p of the diffusion coefficient and of the escape time are made explicit. Using the fact that the acceleration time-scale is given by $\tau_{acc} = p^2/D(p)$, it is possible to write:

$$\underbrace{p^2\frac{d^2 f}{dp^2}}_{(1)} + \underbrace{3p\frac{df}{dp}}_{(2)} - \underbrace{f\frac{\tau_{acc}(p)}{\tau_{esc}(p)}}_{(3)} = 0 \tag{6.6}$$

Using the *dominant balance* asymptotic approximation [see e.g. 173, ch. 3], it is possible to show the behaviour of the solution for the two extreme cases: $p \ll 1$ and $p \gg 1$. In the first case, only the terms (1) and (2) in equation (6.6) contribute, giving as a solution $f(p) = A\left(\frac{x}{x_*}\right)^{\alpha}$ (with $\alpha = -2$ for this particular case). Instead, for large values of p, due to the p^2 dependence of the ratio between acceleration and escape time, the dominant contribution comes from (1) and (3). The solution is an exponentially decreasing function $f(p) = Ae^{-(p/p_*)}$ [3]. Furthermore, even in the case where the radiative cooling is constant ($r = 0$), the escape time will eventually dominate for large values of p, resulting in the exponential cut-off form being maintained.

When terms cannot be easily neglected, both the acceleration and escape time-scales enter in the full solution. This is clearly shown in the case $q = 2$ (the *hard-sphere* case). Here, both acceleration and escape times become independent of the energy of the particle and, adapting (6.5) for the new momentum dependencies, it can be shown that the solution is a simple power-law function with spectral index $\alpha = -\frac{3}{2} - \sqrt{\frac{9}{4} + \frac{\tau_{acc}}{\tau_{esc}}}$. For this special case, this expression extends the simpler one that was given in the Introduction (section 1.2.2), which is valid only in absence of momentum diffusion [24].

6.1.2 The general case

For realistic conditions of particle acceleration up to high energies, the radiative losses can no longer be ignored and the situation is more complicated. In the framework of diffusive shock acceleration, Zirakashvili and Aharonian [175] solved analytically the transport equation for electrons when dealing with Bohm diffusion and synchrotron losses, obtaining $\beta_e = 2$.

[2] δ injection represents the case the particular injection spectrum is a Dirac's δ function in momentum space.

[3] this approach has been tested using the numerical solution of (6.6) through the software Wolfram MATHEMATICA [174].

In the case of stochastic acceleration, Schlickeiser [176] and Aharonian et al. [177] already demonstrated the formation of modified cut-offs in the particle spectrum when balancing acceleration and radiative losses.

In this context, there is a general relation linking the cut-off of the particle spectrum to the acceleration and cooling processes. As shown before in Equations (6.2) and (6.3), both the diffusion coefficient and the radiative cooling time scale can be expressed in terms of their dependency on the energy of the particle, through the indices q and r. The final cut-off the primary particle spectrum is found via the relation [178]:

$$\beta_e = 2 - q - r \tag{6.7}$$

Besides the Bohm diffusion case, which arises for $q = 1$, other canonical values for this parameter are $q = \frac{3}{2}$ and $q = \frac{5}{3}$ for, respectively, a Kraichnan or a Kolmogorov spectrum of magnetic turbulence, and $q = 2$ for the "hard-sphere" approximation. The slope q governs the frequency of the collisions for particles random-walking in the turbulence.

The application of the relation (6.7) tells us that the presence of a radiative cooling with a time-scale inversely proportional to the energy of the particle, leads to a sharpening of the cut-off.

6.1.3 From primary particles to photons

What has been shown up to here holds for the spectra of the primary particles, but intuitively it is possible to imagine that different shapes of these initial spectra would result in different spectra of the photons. In Chapter 1, I described the relation between the slope of the power-law of the primary particles and the slope of the emitted gamma rays for various radiative process. Here I go into more details about what happens to the cut-off shape.

The case of synchrotron radiation was studied in detail by Fritz [179] who found that the relation between the primary particle cut-off and the photon cut-off β_γ is:

$$\beta_\gamma = \frac{\beta_e}{\beta_e + 2} \tag{6.8}$$

which means that the photons always have a stretched spectrum with respect to the primary particles spectrum. In the particular case of Bohm diffusion ($q = 1$), used previously as an example, and synchrotron radiation ($r = -1$), the final photon cut-off is $\beta_\gamma = 0.5$.

The relation between the value of the cut-off of the primary particles and the value of the cut-off of the gamma rays is more involved for the case of inverse Compton losses. The main reason is that in this type of interaction there is not only the shape of the distribution of the primary particles to be taken into account, but also the distribution of the target photon field, and the energy of the centre of mass of the interaction, which dictates if we are in the Thomson or in the Klein-Nishina regime[4]. Lefa et al. [180] carried out a detailed analysis on the effect of all these factors on the value of β_γ using different photon fields, studying the interaction between electrons and photons in the Thomson and K.N. limit. According to their findings, in the latter, the electron will lose almost all of its energy in the course of a single interaction. For this reason the emitted photon spectrum will resemble the spectrum of the primaries with $\beta_\gamma = \beta_e$. The behaviour in the Thomson regime is instead more similar to the one found for only synchrotron radiation with an overall stretching of the cut-off. However, the exact result depends on the distribution of the target photon field, with different possible scenarios:

- Thomson regime on monochromatic target: $\beta_\gamma = \frac{\beta_e}{2}$;
- Thomson regime on Planckian photon field: $\beta_\gamma = \frac{\beta_e}{\beta_e+2}$;
- Thomson regime on Synchrotron photons (SSC scenario): $\beta_\gamma = \frac{\beta_e}{\beta_e+4}$.

A relation between the cut-off of the primary particles and the gamma ray photons can be found also for the hadronic channel (described in section 1.4). In this case, one of the most important processes is the emission of gamma rays from the decay of neutral mesons (mainly π and η mesons) produced in proton-proton interactions. Once the description for emissivity of the π^0-mesons is taken into account, Kelner et al. [181] and Kafexhiu et al. [34] have shown that also in this case there is a stretching of the cut-off in the photon spectrum.

Precise measurements of gamma-ray-photon cut-offs are then useful tools to reconstruct the value of the cut-off of the primary particle spectrum and consequently the balance between acceleration and cooling of the particles. For variable sources time resolution is a particularly important aspect in order to disentangle the effects of different flaring events.

Regarding the feasibility of this task, in the case that the cut-off resides in the GeV domain, the best instrument that can currently probe it is the *Fermi*-LAT. As described in section 1.6.1, this space telescope can count on an effective area of roughly 1 m^2 and to

[4] as reviewed in section 1.3.1, the Thomson regime holds if $\varepsilon_e \varepsilon_\gamma^{bg} \ll \left(m_e c^2\right)^2$

properly measure the cut-off region, a high level of count statistics is needed. However, this is available only for a limited number of sources, those which have particularly high fluxes. In the study I carried out with my collaborators and reported in [172], we have chosen a set of 3 bright sources observed with the *Fermi*-LAT, described in the following section and reported in Table 6.1. They are the averaged emission of the Vela pulsar and 2 bright flares observed for the AGNs 3C 454.3 and 3C 279 in 2010 and 2015 respectively.

TABLE 6.1: Sources and type of event analysed. In the last column is reported the MJD interval from which the SED has been extracted.

Object	Class	Event type	Analysed period	MJD interval
3C 454.3	AGN (FSRQ)	Flare	Nov. 2010	55516 - 55523
3C 279	AGN (FSRQ)	Flare	June 2015	57187 - 57190
Vela PSR[5]	Pulsar	Avg. emission	Aug. 4, 2008 - July 31, 2012	54682 - 56139

Having obtained the best limits on the cut-off value achievable with the *Fermi*-LAT, I then make use of the simulated IRFs for the next generation Cherenkov Telescope Array to assess the benefit that this observatory can give to this type of studies.

6.2 The sources and the analysis of the data

The reduction of the *Fermi*-LAT data was performed between energies of 70 MeV and 300 GeV, following a rather standard procedure already used for the sources discussed in previous chapters and described in more details in Appendix C. The data were extracted from a square region $30° \times 30°$ centred on the positions given by the 3FGL catalogue [106] using SOURCE class events. The spectral parameters of the sources were then obtained by fitting a model to each region of interest. To determine the contribution of the background sources I performed the fit of the RoIs in two steps, removing in the first phase all of the sources with detection significance lower than $\sim 2\,\sigma$. For the flaring events of the 2 AGNs, this procedure was done on longer time intervals to avoid the influence of statistical fluctuations due to very short time-scales. Because the analysis of these data also considered energies below 100 MeV, the data reduction also made use of the information coming from the energy dispersion matrix (as in Chapter 4) which had the advantage of reducing the systematic uncertainties on the effective area. The points of the SED were then computed for bins with a test statistic value of at least 9 (corresponding to a significance of $\sim 3\,\sigma$). Following the approach used in Chapter 5, the number of expected photons was also saved, in order to correct the wrong Gaussian approximation on the flux uncertainty in presence of a low number of photons in the

[5] 3FGL time interval

energy bin. These data-points were then used when estimating the impact of CTA in the study of the cut-off region.

6.2.1 Vela pulsar

The Vela pulsar is the brightest persistent source in the GeV energy range [182]. In this analysis I use the averaged emission of the pulsar over 4 years of data using the same time interval of the 3FGL catalogue. Due to the large amount of data collected by the *Fermi*-LAT for this object, the corresponding spectral parameter constraints are the strongest compared to the other two sources and we can consider this as our best case study. The role of this data-set is to give an idea of the extremely high precision that can be achieved with the *Fermi*-LAT when high statistic are available. As I will show for the 2 flares, the situation is different when it is not possible to average the emission of multiple years of observation. The best fit values when fitting the spectrum with a function like Equation (6.1) are in Table 6.2 and the corresponding SED is in Figure 6.1.

TABLE 6.2: Fit of the photon spectrum with a power-law with stretched exponential cut-off for the Vela pulsar as obtained by the *gtlike* routine

Parameter	Value
N [ph/cm^2/s/GeV]	$\left(1.39^{+0.12}_{-0.10}\right) 10^{-5}$
Γ	1.019 ± 0.011
E_c [GeV]	0.238 ± 0.016
β_γ	0.464 ± 0.009
E_s (fixed) [GeV]	0.83255

For our study, the parameter we are mostly interested in is β_γ, which distorts the cut-off. For this dataset I obtained $\beta_\gamma = 0.464 \pm 0.009$. From this result we can exclude the possibility of $\beta_\gamma = 1$, namely a simple exponential cut-off function. Because we are dealing with the averaged emission from a pulsar, the outcome of $\beta_\gamma < 1$ can also be explained as the superposition of different spectra emitted during the various phases of the pulse [183]. Besides superposition effects, sub-exponential cut-offs can also naturally arise when taking into account the emission in the transition regime between curvature and synchrotron radiation, as shown by Kelner et al. [184]. A general aspect that should be noted when dealing with a sub-exponential cut-off, is that, having $\beta_\gamma < 1$, the cut-off value shifts to lower energies, with the bend of the spectrum starting at much lower energies. For the Vela pulsar we are already in the cut-off region at energies of 250 MeV having a value for $E_c = 0.238 \pm 0.016$ GeV even though the actual peak of the SED is at ~ 1 GeV.

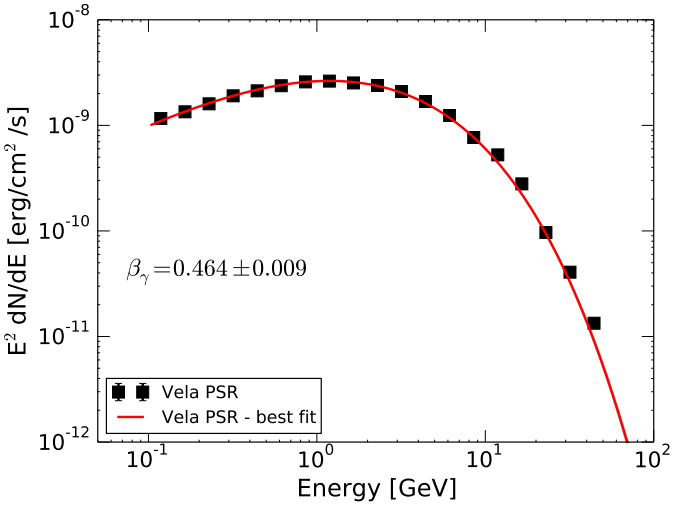

FIGURE 6.1: SED of the Vela pulsar averaged over 4 years of data. The thick red curve is the best fit model and the shaded area represents the 1 σ confidence band (not visible due to the small statistical uncertainties).

6.2.2 3C 454.3 flare

The FSRQ 3C 454.3 is the brightest AGN in the GeV band observed by *Fermi*-LAT. It is a highly variable source located at a redshift $z = 0.859$ [106]. For this study I have analysed the brightest flare detected by the *Fermi*-LAT in November 2010 when the source reached an integrated flux above 100 MeV of $\sim 8 \times 10^{-5}$ ph cm^{-2} s^{-1} [185]. For the study of the flaring phase, I used the same interval identified by Abdo et al. [185], analysing it with the latest tools provided by the *Fermi* collaboration. The resulting SED is shown in Figure 6.2 where I also show the fit of the power-law with stretched exponential cut-off (PLSEC) and the 1 σ contour based on the statistical uncertainties. The analysis of the data from 3C 454.3 cannot provide a constraint as strong as the one obtained for the Vela pulsar. In this case, $\beta_\gamma = 0.4 \pm 0.1$. The results of the value of the other parameters are reported in Table 6.3 where it is worth noticing the asymmetry of the 1 σ confidence interval of each parameter.

TABLE 6.3: Fit of the photon spectrum with a power-law with stretched exponential cut-off for 3C 454.3 as obtained by the *gtlike* routine

Parameter	Value
N [ph/cm^2/s/GeV]	$\left(4.7^{+3.9}_{-1.2}\right) 10^{-5}$
Γ	$1.87^{+0.08}_{-0.12}$
E_c [GeV]	$1.1^{+1.6}_{-0.9}$
β_γ	0.4 ± 0.1
E_s (fixed) [GeV]	0.41275

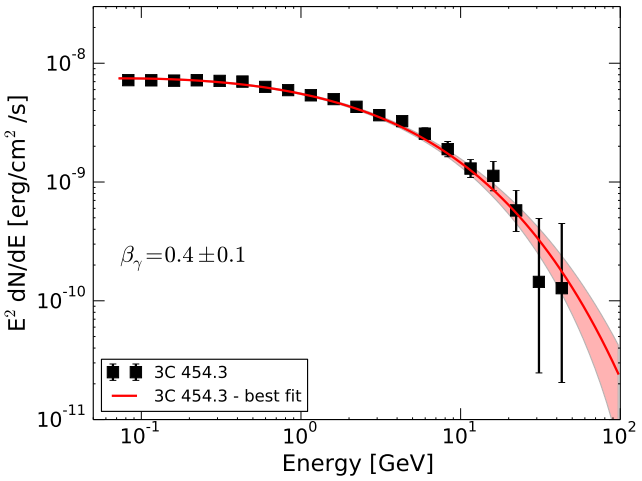

FIGURE 6.2: SED of the blazar 3C 454.3 during its flaring phase with the value of the parameter beta. The thick red curve is the best fit model and the shaded area represents the 1 σ confidence band.

As a FSRQ blazar, we expect the gamma-ray peak of this source to be produced by Inverse Compton interactions on external photon fields like disc emission or the Broad Line Region (see section 1.5.2). If we assume that these interactions are happening in the Thomson regime, from the fitted value of β_γ, we obtain a value $\beta_e = 1.3 \pm 0.6$ where the big uncertainty is related to the indirect measurement[6]. Alternatively, an SSC model would require $\beta_e = 2.7 \pm 0.9$ leading to a very steep cut-off in the primary particle spectrum. A different explanation, that is also compatible with the values we obtained, is the emission via proton synchrotron due to interaction between the jet of the source and a red giant star [186]. In this case, the proton spectrum would have a simple exponential cut-off that, via synchrotron emission, would produce gamma rays with $\beta_\gamma = 1/3$. As we have seen, having a precise measurement of the β_γ parameter is crucial for characterising the interplay of acceleration and radiative cooling during flaring states. The poor constraint obtained through the analysis of the *Fermi*-LAT data alone (due to the limited *Fermi*-LAT photon statistics) prevent further speculation on the possible origin of this value.

6.2.3 3C 279 flare

This FSRQ is historically known to be a variable gamma-ray emitter, already detected by EGRET [187], it has a redshift $z = 0.536$ [188]. This bright AGN underwent a very bright flare in June 2015 [189, 190] that triggered a dedicated pointing of the *Fermi*-LAT

[6]This value is emission model dependent and its uncertainty comes from the propagation of the error on β_γ.

to maximise the statistic. Thanks to this decision, the data are able to show minute-scale variability for this bright flare [191]. However, to obtain a measurement of the cut-off, a large number of photons is required, so my analysis refers to the 3 days that showed the highest flux [cfr. 192, for a daily lightcurve]. The SED of the source obtained by integrating the emission over this time interval is shown in Figure 6.3.

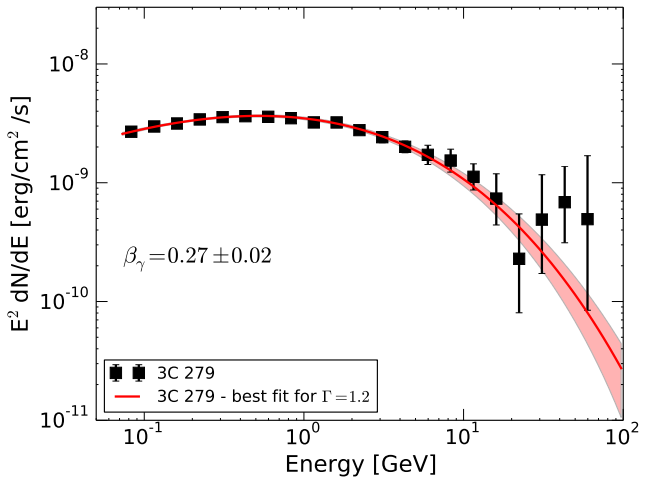

FIGURE 6.3: SED of the blazar 3C 279 during its flaring phase with the parameter β_γ. The thick red curve is the best fit model and the shaded area represents the 1 σ confidence band. The parameter value and the confidence band were derived after fixing the photon index Γ to 1.2.

For this AGN, the *gtlike* routine could not converge when all parameters of the modified exponential cut-off model were left free. For this reason we perform separate fits fixing the photon index to the values 1.2, 1.4 and 1.6. The choice of these values is motivated by the hard spectrum measured in the X-rays by the *Swift*-XRT instrument. Ackermann et al. [191] report a value of $\Gamma_X = 1.17 \pm 0.06$ during the peak of the flare, while Pittori et al. [193], in an ATel report a value of 1.4. Finally, a joint fit of the *Fermi*-LAT data and the measured luminosity in the X rays gives something closer to 1.6. Given these values, we decide to show in the SED in Figure 6.3 only the case for $\Gamma = 1.2$ and focus our analysis on it. The values for the other fits are given in Table 6.4. With the photon index parameter fixed, the stretching of the cut-off is constrained to $\beta_\gamma = 0.27 \pm 0.02$ where the effect of the assumption on the photon index in the fit considerably reduces the uncertainty on the measurement. With this caveat in mind, we highlight that a value of β_γ close to 0.3-0.4 can be explained either by a simple exponential cut-off in the primary particles for external Compton (and proton synchrotron), or by $\beta_e \sim 2$ for an SSC scenario.

TABLE 6.4: Fit of the photon spectrum with a power-law with stretched exponential cut-off for 3C 279 for the different choices of the photon index. The plot of the SED with the best fit function using $\Gamma = 1.2$ can be seen in Figure 6.3

Parameter	$\Gamma = 1.2$	$\Gamma = 1.4$	$\Gamma = 1.6$
N [ph/cm^2/s/GeV]	$\left(2.8^{+0.8}_{-0.6}\right) 10^{-4}$	$(8.6 \pm 1.0)\, 10^{-5}$	$\left(3.7^{+0.3}_{-0.2}\right) 10^{-5}$
Γ (fixed)	1.2	1.4	1.6
E_c [GeV]	$\left(8.4^{+6.6}_{-4.1}\right) 10^{-3}$	0.10 ± 0.04	$0.81^{+0.16}_{-0.15}$
β_γ	0.27 ± 0.02	0.34 ± 0.03	0.46 ± 0.04
E_s (fixed) [GeV]		0.341966	

6.3 The potential of CTA

The possibility of exploring the cut-off region of GeV sources more sensitively may be brought about through an increase of effective area of the gamma-ray instrument. This can be achieved through a lowering of the energy threshold of ground based Cherenkov telescopes. These instruments have already proven themselves to be able to reach a minimum energy close to few tens of GeV under particular conditions as shown by MAGIC [194] and H.E.S.S. Collaborations [195]. In this section, I will demonstrate the improvement possible through such an increase in the effective area at energies around tens of GeV, for our sample of bright "*Fermi*" sources. In particular, I will look at the case of the *Cherenkov Telescope Array* observatory, currently planned as the next step in the evolution of Imaging Atmospheric Cherenkov Telescopes.

In this study I focus on the impact of the performance of the CTA observatory on the determination of the spectral parameters of the sources we have studied in the previous section, comparing the SEDs that we obtained with the *Fermi*-LAT and the SEDs that we would expect from joint fits that include CTA. For this section I am making use of instrument response functions for a preliminary design of the southern array[7], based on the study of Bernlöhr et al. [196] and parametrized in Appendix B[8]. Since in this study I am dealing with 2 flaring AGNs, and in general we are interested in the possibility of constraining the spectra of bright flaring objects, I base my studies on the simulations done by the CTA consortium with the optimisation for an observation time of 0.5 and 5 hours, to highlight the significant improvement already achievable on short time-scales. For the Vela pulsar I instead simulate only the outcome of a 5 hours observation, which can potentially represent the data taken during a single night.

[7] `https://www.cta-observatory.org/science/cta-performance/` with simulations dated 2015-05-05 - accessed on 25/05/2017

[8] The decision to go for a parametrization is justified by the fact that the IRFs are still very preliminary as the observatory is not yet in place. The use of an analytical parametrization makes all the assumption clearer and the analysis more reproducible.

Through the convolution of the effective area with the source flux, I compute the expected count rate at the CTA detector. To do this, I extrapolate the flux level from the *Fermi*-LAT best fits and convolve it with the effective area of the CTA observatory, applying also the EBL absorption for the 2 extragalactic sources (according to the model of Franceschini et al. [55]). At this point the expected number of events in the time interval is drawn from a probability density function matching the expected differential count rate at the detector.

To properly simulate the response of CTA, I smear the *true* distribution with the parametrized IRFs and successively unfold this *measured* sample of events so to recover the *reconstructed* datapoints. The unfolding of the measured distribution of photons is performed via the `RooUnfold` package[9] [197]. The unfolding procedure uses an iterative Bayesian approach trained on a large test dataset to recover the response matrix with an arbitrary bin size. To correctly take into account the background level, the distribution injected in the unfolding routine is the sum of the signals of the source and the background. The uncertainties on each bin also take into account the covariance matrix, which is particularly relevant near the threshold. With this operation, we are able to derive the number of expected counts in each of the 10 logarithmically spaced new energy bins spanning from 20 GeV to 2 TeV (11 bins for the 5 hours case).

The actual source counts and the 1 σ errorbars are instead derived starting from the total number of counts in the bin $N = S + B$, where S is the count coming from the source and B represents the background counts, supposed to be known with good accuracy for the observation.

The lower and upper limits on the source counts are then extracted following a "classical approach" [198]:

$$S_{up} = N_{up} - B \tag{6.9}$$

and

$$S_{low} = N_{low} - B. \tag{6.10}$$

I avoid the case of $B > S$ in the calculation, defining only high and low limits for a 68% confidence interval.

The resulting SED with both the *Fermi*-LAT points above 10 GeV and the CTA ones is shown in figure 6.4. The *Fermi*-LAT points are the ones from section 6.2, obtained with an integration time of a few days. As can be seen in the plot, for the 2 bright AGNs considered, up to 100 GeV, the CTA points are above the 5 σ detection limit: flares

[9] `http://hepunx.rl.ac.uk/~adye/software/unfold/RooUnfold.html` - accessed on 25/05/2017

with brightness similar to the ones analysed here will therefore be easily detectable. In the case of the Vela pulsar we are instead deeply in the cut-off region and after a 5 hours observation, there is still not enough statistic to reconstruct points above 80 GeV. Nevertheless, the size of the reconstructed error bars compare very well with what Fermi was able to achieve with 4 years of data.

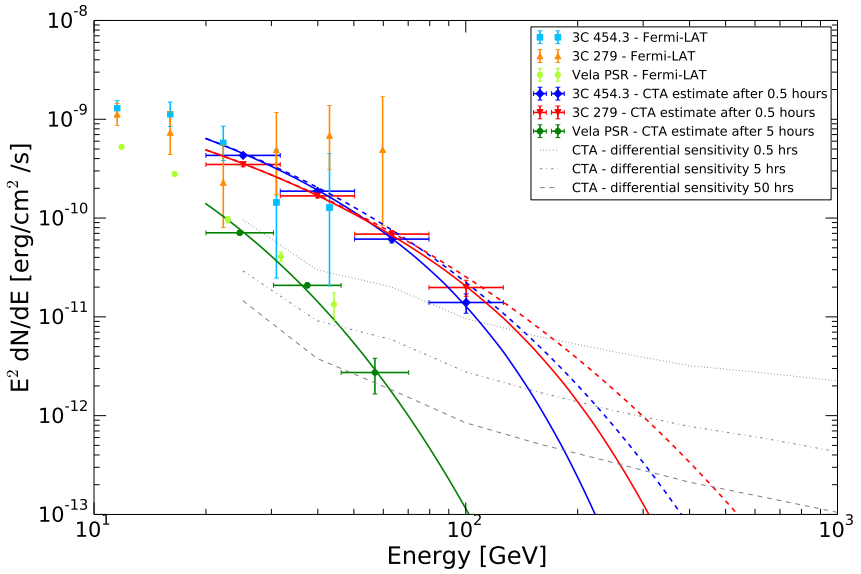

FIGURE 6.4: SED above 10 GeV with the *Fermi*-LAT points and the CTA estimate after 30 minutes of observation for 3C 454.3 and 3C 279 and after 5 hours for the Vela pulsar (blue, red and green respectively). The solid lines are the observable extrapolated spectra that in the case of the AGNs have been absorbed according to the EBL model of Franceschini et al. [55], while the dashed lines represent the de-absorbed extrapolation. The grey lines are the differential sensitivity of CTA-South after 0.5, 5 and 50 h of observation.

Once we have the simulated points, the improvement in our ability to constrain the parameter β_γ for the 2 blazars can be assessed by fitting the combined *Fermi* and CTA datasets shown in Figure 6.4. For the Vela pulsar the addition of the 3 CTA datapoints is not able to significantly improve the constraints, due to the high level of statistics that the *Fermi*-LAT already achieves with an integration time of 4 years, so the focus will be on the blazars.

The χ^2 minimization is performed through a MCMC method using the PYTHON tool `emcee`, already described in section 4.2.1. The starting point for the MCMC routine is the best fit model from the *Fermi*-LAT data and I use 100 parallel walkers running for 24000 steps with a burn-in phase of 100 steps. In the fitting procedure, the CTA points are de-absorbed for the EBL effect and the likelihood calculation also takes into account the covariance matrix of these unfolded points. The resulting constraints on the β_γ parameter for the 2 bright blazar flares are reported in Figure 6.5, along with the

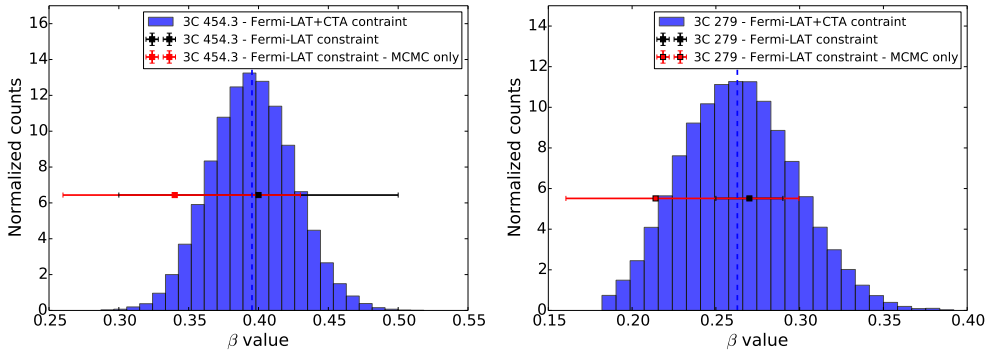

(A) 3C 454.3 (B) 3C 279

FIGURE 6.5: β_γ posterior distribution of the joint dataset. In panel 6.5a there is the β_γ distribution for the blazar 3C 454.3 while in panel 6.5b we report the one for the blazar 3C 279. The full histogram represents the distribution of β_γ for the joint fit while the black and red bars correspond to the 1 sigma confidence interval obtained when fitting the *Fermi*-LAT points only using the official tools and the MCMC method, respectively. Note that in the fit of the joint 3C 279 dataset, the photon index was left free to vary with a consequent shift in the value of the parameters. The width of the posterior distribution in this case remains comparable to the size of the 1 σ confidence interval obtained with the *Fermi*-LAT only data and with a smaller number of degrees of freedom.

TABLE 6.5: Value of mean and RMS of the β_γ parameter after the fit of the *Fermi*-LAT and CTA estimated data for observation time of 0.5 hours and 5 hours.

Object	β_γ after 0.5 hrs (ratio error/value)	β_γ after 5 hrs (ratio error/value)
3C 454.3	0.40 ± 0.03 (0.08)	0.40 ± 0.02 (0.05)
3C 279	0.26 ± 0.03 (0.12)	0.26 ± 0.02 (0.08)

posterior distribution obtained from the *Fermi*-LAT data alone and the result obtained with the official *Fermi*-LAT tools. The mean value and the RMS of these histograms are reported in Table 6.5 for an observing time of 0.5 and 5 hours. The difference between the values of β_γ for 3C 279 depends on the fact that the MCMC fit on the *Fermi*-LAT data only converges to parameters values that are slightly different from the ones used to extract the CTA data points, as visible in Figure 6.5b. However, this result clearly demonstrates that we could be able to reduce the uncertainty on the β_γ down to a $\sim 10\%$ level by adding the data that CTA could collect in just 0.5 hour.

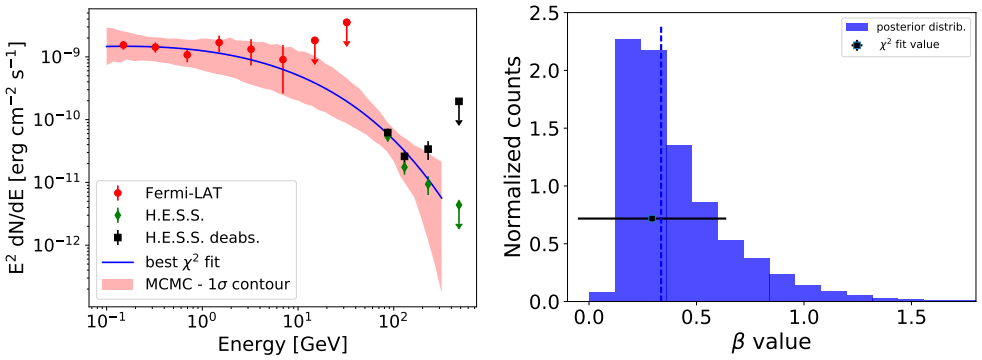

(A) 3C 279 *Fermi*-LAT– H.E.S.S. simultaneous SED

(B) Posterior distribution β_γ parameter

FIGURE 6.6: On the left plot, SED for the blazar 3C 279 using simultaneous data collected by *Fermi*-LAT and H.E.S.S. in 3.1 hours of observation. The red circles are the *Fermi*-LAT points, the green diamonds the original H.E.S.S. points, and the black squares are the H.E.S.S. points after EBL de-absorption. The blue line is the result of a minimum χ^2 fit to the the *Fermi*-LAT and de-absorbed H.E.S.S. dataset using a PLSEC function. The red contour is instead derived from the MCMC scan of the parameter space. The right panel shows the final posterior distribution of the β parameter in comparison with the value obtained with a simple χ^2 fit. The dashed blue vertical line indicates the 50^{th} percentile of the distribution.

6.4 Recent developments

Recent observations carried out by the H.E.S.S. telescope can already bring us a bit closer to what could be the outcome of the CTA observations[10]. During the flare of the FSRQ 3C 279 that I have shown in this chapter, the H.E.S.S. Collaboration observed for two nights around the peak of the GeV lightcurve. During the first night CT5 was not participating in the observations and the data lead to upperlimits on the flux. During the second night however (MJD 57189, right after the peak in the *Fermi*-LAT light-curve), the use of CT5 MONO observations yielded a clear detection, with a significance of 8.7σ over 3.1 hours of live time [199]. Furthermore, thanks to the pointing strategy adopted by the *Fermi*-LAT, it was actually possible to derive a spectrum at GeV energies completely simultaneous to the H.E.S.S. observation. The *Fermi*-LAT analysis was performed in a similar way as illustrated in this chapter, but it was not possible to use the energy dispersion correction, so the fit was restricted to energies above 100 MeV. In Figure 6.6, we show the gamma-ray spectrum obtained with the two instruments.

Using the same approach used with the simulated CTA data, I have fit the two datasets with a PLSEC function, obtaining the values reported in Table 6.6. The β_γ parameter

[10]this information was not publicly available at the time of publication of [172], which this chapter refers to.

TABLE 6.6: Fit results for the simultaneous datasets obtained with *Fermi*-LAT and H.E.S.S. of the 3C 279 flare. The results obtained with a standard χ^2 fitting routine and the results obtained with the MCMC scan are reported in this table. The normalization and the cut-off position were fit in terms of the $\log_{10}$ of their value and then transformed back to a linear quantity. Even with this implementation, the χ^2 fit is not able to retrieve a good estimate of the uncertainty on the parameter value, due to the high correlation between the parameters.

Parameter	χ^2 fit	MCMC fit
$\log_{10} N_0$ [ph/cm^2/s/GeV]	-4.5 ± 1.6	$-4.75^{+0.91}_{-0.24}$
Γ	1.73 ± 0.83	$1.93^{+0.29}_{-0.41}$
$\log_{10} E_c$ [GeV]	-0.7 ± 5.2	$0.13^{+1.33}_{-2.82}$
β_γ	0.29 ± 0.35	$0.34^{+0.32}_{-0.14}$
E_0 [GeV]	0.3 - fixed	
χ^2_{red} value	1.58	2.08

is still affected by a large uncertainty. However, the best fit value still points toward a scenario with $\beta_\gamma \sim \frac{1}{3}$, meaning that in the scenario of emission due to leptonic Inverse Compton, the primary particles have a value cut-off index close to 1.

As visible from the plot in Figure 6.6, the last data-point in the H.E.S.S. spectrum seems to indicate an up-turn in the de-absorbed spectrum of the source. Because of the strong dependency of the EBL absorption with energy at energies above 200 GeV for redshifts greater than 0.5, it is important to take into account the actual systematics in the energy scale. However, the application of the same methodology implemented to derive the intrinsic spectra in Chapter 2, did not bring any significant change in the reconstructed value of β_γ. The constraint mainly comes from the first two points of the H.E.S.S. spectrum and the statistical errors are more important than the systematic ones in this particular case.

6.5 Conclusions

In this chapter I have investigated the spectra of a sample of some of the brightest sources observed by *Fermi*-LAT, namely the Vela pulsar and the 2 bright FSRQs, 3C 454.3 and 3C 279. The value of the cut-off index β_γ retrieved from the analysis of the Vela pulsar is very well defined thanks to the very good statistics obtained through the long exposure. The two blazars however, suffer from a lack of counts above 10 GeV, where the photon flux is simply too low for the *Fermi*-LAT to obtain good constraints. The results place mild limits on the primary particle distribution due to the uncertainties from the fits.

The level of uncertainty on the parent (electron) cut-off index β_e is inferred to sit between 30 and 50 percent of the value.

Using the data from both *Fermi*-LAT and CTA, I have shown that the photon cut-off could be improved to 10% precision level, allowing a potential revolution in the understanding of transient objects at high energies. This may give us the chance to capture the evolution of the cut-off region during the flare, while source re-balances the acceleration and cooling of the primary particles. Furthermore, the publication of the data taken by H.E.S.S. on the 3C 279 flare has brought some new results on the characterization of the spectral cut-off of this bright AGN. This result provides a preview of what might happen in the future, when CTA will be able to probe these energies in a more effective way. Even though the constraints are not strict, the results point towards a distribution of primary particles with a simple exponential high energy cut-off.

Conclusions and future plans

The main aim of the work I did during the years that led me to the writing of this manuscript was to shed light on the various types of astrophysical phenomena that we encounter when studying the often highly variable sources that make up the gamma-ray sky. At the moment, we are in a transitional period, awaiting the advent of CTA, which is expected to drastically improve our gamma-ray observations, in particular in the "tens of GeV" regime.

Over the past 10 years, we have already seen ground-based telescopes striving for lower energy thresholds, especially when dealing with extragalactic sources. For the purpose of exploring the energy window below 100 GeV, the H.E.S.S. Collaboration added a much larger telescope to its 10m array, turning it into pathfinder for CTA, as it is a fully hybrid array, capable of observing in different modes and different sub-arrays. The first results obtained with the MONO data of this array were presented in Chapter 2, where I have illustrated the benefits of combining the *Fermi*-LAT and H.E.S.S. results in a more continuous way. The good determination of the spectrum in the energy range around 100 GeV, allowed a more precise reconstruction of the intrinsic emission spectrum of the blazars PKS 2155−304 and PG 1553+113. These first results were unfortunately affected by the large systematics that limited the possibility of lowering the threshold even more for long exposures. What was still very important in these results was the good synergy shown utilising *Fermi*-LAT and H.E.S.S. data. This level of synergy was seen as well in the study of the gamma-ray emission from the binary system PSR B1259−63. For this system, having simultaneous coverage at GeV and TeV energies allowed us to shed more light on the still enigmatic phenomenon of the so called *GeV-flare*, as discussed in Chapter 3. Through simultaneous observations it was possible to confirm, from the TeV light curve, that the source was in high state during the GeV flare, while further observations will be necessary to unveil the exact physical processes responsible for the high energy emission in this binary system.

For the moment, the sub-GeV domain is the territory of satellite telescopes like *Fermi*-LAT (and its "little brother" *AGILE*). In this energy range, these telescopes can provide incredible data set, especially from the observations of bright objects such as solar flares, which can outshine the other sources of the GeV sky during their prompt emission (see Chapter 4). The use of this high quality data together with updated models for the hadronic interactions in the Sun's atmosphere is changing what we thought we knew about the acceleration of particles in the solar flares, indicating that the spectra of the primary particles are harder than previously thought. As good as this data is, however, our ability to test these model predictions would be significantly enhanced by extending our coverage down to the MeV energy range, so we can better constrain the energy distribution of the primary particles by breaking the degeneracy between cutoff energy and slope and by also allowing us to see directly the contributions from nuclear interactions.

Another reason why the contribution to the knowledge in gamma-ray astrophysics brought by the *Fermi*-LAT is so important is the possibility of having an unbiased monitoring of the sky, through its large field of its survey mode operation. When joining these long term observations with the very extended energy coverage, the results can be used to explore the presence of various spectral components in the emission of sources as it was done with the blazar MRK 501 in Chapter 5. Interestingly, for this source there seems to be the presence very hard photon indices, harder than 1.5, which cannot be easily explained in the framework of diffusive shock acceleration. Unfortunately, the lack of statistics at high energies due to the small effective area of *Fermi*-LAT prevents a good determination of the spectrum for $E > 10$ GeV. Fortunately, in ground based gamma-ray experiments there is now a trend towards focusing on few objects to maximise the physics returns from the observations and monitoring programs on objects like MRK 501 are being more and more common [200]. The FACT program and the HAWC observations will both be powerful probes of the long term behaviour of gamma-ray sources in the TeV range, providing flux measurements unbiased toward bright flares as has been the case till now.

The energy range around 10 GeV remains a critical window, and future observations using CTA will be fundamental for exploring in detail this energy interval. As shown in Chapter 6, the impact of the much larger collection area compared to the space telescopes will produce extremely precise spectra, not only in energy domain, but also in the temporal one. As I have shown, in the case of flares from bright sources, the quality of the data above 20 GeV gathered after just 30 minutes of data taking can match that gathered by *Fermi*-LAT only after several days of continuous observation.

The role of the *Fermi*-LAT however, remains crucial for two distinct reasons: to give the trigger for bright GeV flares since CTA is not an all-sky monitor, and to extend the spectrum to sub-GeV energies, constraining it at the beginning of the cut-off region, a role that CTA would not be able to undertake for many extragalactic objects.

This fundamental increase in the collection area at an energy of a few tens of GeV, hopefully will be enough to detect with ground based telescopes the still elusive *gamma ray bursts* (introduced in Chapter 1). The plots in Figure 7.1, show the light curve and the high energy spectrum of the long duration GRB GRB090926A[11]. Two main points can be highlighted: from the light curve in the left panel, we see the clear feature of delayed emission in the high energy range ($E > 100$ MeV); the SED in the right panel instead shows the presence of a hard component which extends up to GeV energies (in the c and especially d intervals). The possibility to catch this enhanced emission at GeV energies in the later stages of the burst is what motivates GRB searches with ground-based, low-threshold Cherenkov telescopes. A low threshold is again important because of the impact of EBL absorption (see subsection 1.5.2.2). A telescope that reaches down to 20-30 GeV can see much more of the Universe (and potentially many more GRBs) than current telescopes with ~ 100 GeV thresholds. Also, our knowledge about the intrinsic VHE spectra of GRBs is highly uncertain. With a low threshold instrument, however, the extrapolation from the "Fermi range" is minimal, and GeV-detected bursts like GRB GRB090926A should essentially be guaranteed sources for CTA. At the moment, perhaps not entirely surprisingly, the detection of GRBs with ground based gamma-ray telescopes is still missing, even though the major IACT Collaborations have in place fast slewing systems and quick response to GRB alerts coming from other instruments [e.g. 201, 202]. The hope is that the first detection of a GRB with a ground based telescope will be announced soon, allowing a deeper understanding of this still poorly understood source class.

[11] the naming convention for GRBs is to have GRB followed by two digits for the year, two digits for the month, two digits for the day and a letter that discriminates between multiple bursts detected on the same date. GRB090926A means the first burst detected on the 26^{th} of September 2009.

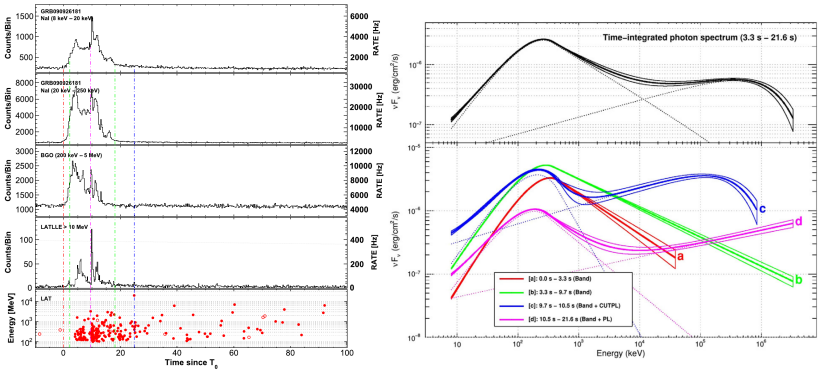

FIGURE 7.1: Light curve and SED of GRB090926A from [40] (originally from [203] and [204] respectively). The *left* panel shows the light curve in different energy bands, highlighting the delayed emission of higher energies. The *right* panel shows instead the spectral evolution of the spectrum.

Appendix A

Diffusion and stochastic acceleration

This appendix gives some more details regarding the diffusion of cosmic ray particles in a magnetic field and the induced effect of stochastic acceleration. This is meant to put the first section of Chapter 6 more in context.

In the theory of stochastic acceleration, the main ingredient is the scattering between particles and the irregularities of the magnetic field present in the plasma.

One of the important parameters that comes into play in the process of acceleration and propagation of high energy particles in astrophysical environments is the diffusion coefficient D that gives us the measure of how easily particles can move around in presence of turbulent magnetic fields. When measuring the diffusion in spatial coordinates, the units of this parameter are those of an area divided by a time. More generally, the diffusion coefficient can be seen as the average variance of a quantity in the interval of time:

$$D = \frac{\left\langle (\Delta x)^2 \right\rangle}{2\Delta t} \tag{A.1}$$

and in this form we can apply the concept not only to spatial diffusion.

Following the description used by Kulsrud in [205] for the quasi linear theory, and the explanation given in the introduction of [178], we assume that the turbulence in the magnetic field can be written as a small perturbation δB on top of a homogeneous field B_0. The amplitude of these perturbations follows a power-law distribution as a function of their wave numbers with index q so that the energy density of the perturbations can

be written as the integral of the power spectrum between the wave numbers k_1 and k_2:

$$\frac{(\delta B)^2}{8\pi} = \int_{k_1}^{k_2} W(k)dk \propto \int_{k_1}^{k_2} k^{-q}\, dk \propto k^{-q+1} \tag{A.2}$$

If the characteristic frequency of the perturbation is close to the gyration frequency Ω_g of the particle, the particle will receive a small change in its pitch angle. This resonant condition implies also that $1/k \sim R_L$, where R_L is the Larmor radius and that the period of the perturbation is $\tau = \frac{2\pi}{\Omega_g}$. With these assumptions, each interaction would give a change in the pitch angle of

$$\delta\theta = -\pi \frac{\delta B}{B} \cos\phi' \tag{A.3}$$

with the average effect given by:

$$D_\theta = \frac{\left\langle (\Delta\theta)^2 \right\rangle}{2t} = \frac{\pi}{8}\Omega_g \left\langle \left(\frac{\delta B}{B}\right)^2 \right\rangle \tag{A.4}$$

after the integration over the phase ϕ' and

$$\tau_\theta = \frac{1}{D_\theta} \approx \frac{1}{\Omega_g \left\langle \left(\frac{\delta B}{B}\right)^2 \right\rangle} \propto E^{2-q} \tag{A.5}$$

where, as in [205], the numerical factors are neglected and I have also explicitly stated the energy dependence.

The step from pitch-angle to spatial diffusion coefficient is well explained by Drury [206]. The time-scale τ_θ of the diffusion of the pitch angle is the time needed for the cumulative change in pitch angle to become equal to one. Because this is a random process, after N steps the cumulative change will be $\Delta\theta \sim \sqrt{N}\delta\theta$ and consequently the number of steps needed will be $N = (\delta\theta)^{-2}$. After N steps, the displacement in the direction parallel to the field is given by

$$\lambda_\parallel \sim N R_L \tag{A.6}$$

The mean free path perpendicular to the field is instead

$$\lambda_\perp \sim \sqrt{N}\delta\theta R_L \tag{A.7}$$

Finally, it is possible to write the diffusion coefficient in both directions explicitly indicating the proportionality to the energy of the particle (due to the resonant condition)[1]

$$D_{\parallel} = \frac{1}{3} R_L c \left\langle \left(\frac{\delta B}{B} \right)^2 \right\rangle \propto E^{2-q} \tag{A.8}$$

$$D_{\perp} = \frac{1}{3} R_L c \left\langle \left(\frac{\delta B}{B} \right)^2 \right\rangle^{-1} \propto E^{q} \tag{A.9}$$

Multiplying (A.8) and (A.9), we obtain that the product is equal to:

$$D_{\parallel} D_{\perp} = \left(\frac{1}{3} R_L c \right)^2 = D_B^2 \tag{A.10}$$

where D_B is called the Bohm diffusion coefficient and represents the minimum diffusion coefficient and it is obtained with a random field on the scale of the Larmor radius and in terms of the power-law index of the perturbations, it is obtained for $q = 1$.

In the reference frame of the observer, the scattering process will also produce diffusion in momentum space with the particle gaining Δp for each scattering [206]. The change in momentum is approximately:

$$\Delta p \sim p \left(\frac{v_A}{v} \right) \tag{A.11}$$

where v_A is the Alfvén speed in the plasma and v the speed of the particle. From this it is possible to compute, in the same way as before, the momentum diffusion coefficient:

$$D_p = \frac{\left\langle (\Delta p)^2 \right\rangle}{\tau} = p^2 \left(\frac{v_A}{v} \right)^2 \frac{1}{\tau} \tag{A.12}$$

where τ is the one already computed in (A.5). It is worth explicitly stating the dependence on the momentum (or energy) of the particle having

$$D_p \propto p^q \tag{A.13}$$

All these elements go into the transport equation of the particles (e.g. [207] and references therein):

$$\frac{\partial f}{\partial t} = -\frac{1}{p^2} \frac{\partial}{\partial p} \left\{ p^2 \left[A(p) f - D_p(p) \frac{\partial f}{\partial p} \right] \right\} - \frac{f}{\tau_{esc}(p)} + \frac{S(p,t)}{4\pi p^2} \tag{A.14}$$

where $f(p,t)$ is the particle distribution as a function of momentum and time, so that the number of particles $n(p,t)$ with momentum between p and $p + dp$ will be given by

[1] the factor $\frac{1}{3}$ comes from the 3 dimensions of space and naturally arises with a proper computation of the displacements.

$4\pi p^2 f(p,t)dp$. $D_p(p)$ is the momentum diffusion coefficient as in (A.12) and the term $A(p)$ incorporates any possible systematic acceleration or the effect of radiative losses. τ_{esc} is the escape time and $S(p,t)$ is the source term. The escape time is defined as

$$\tau_{esc} = \frac{1}{D_{\|}} \tag{A.15}$$

the time-scale for diffusion along the field line and therefore depends on the momentum of the particle as p^{q-2}.

Appendix B

Parametrization of CTA performances

In this Appendix, I explain in more detail the analytical parametrization of the CTA Instrument Response Functions used in Chapter 6.

B.1 The CTA Observatory

As mentioned in Chapter 6 and in section 1.7.4, the CTA observatory is set to bring a revolution in the study of gamma-ray sources at tens of GeV energies. The full project consists of two sites, one in the northern hemisphere (in the island of La Palma in the Canary Islands, Figure B.1a), more optimised for the study of extragalactic objects, and one in the southern hemisphere (in the Atacama desert of Chile, Figure B.1b), enhanced for TeV observations of the galactic plane. Each of them will consist of an ensemble of several Cherenkov telescopes of various diameters to explore different energy bands of the gamma-ray spectrum, from $\sim$ 20 GeV to $\sim$ 100 GeV as described by Actis et al. [208]. At the time of writing, the preparatory works for its construction have already started and there are already estimates of the final performance of the instrument available[1]. The IRFs of the Southern array have been parametrized in the following section using simple analytical functions.

[1] `https://portal.cta-observatory.org/Pages/CTA-Performance.aspx` with simulations dated 2015-05-05 - accessed 26/05/2017

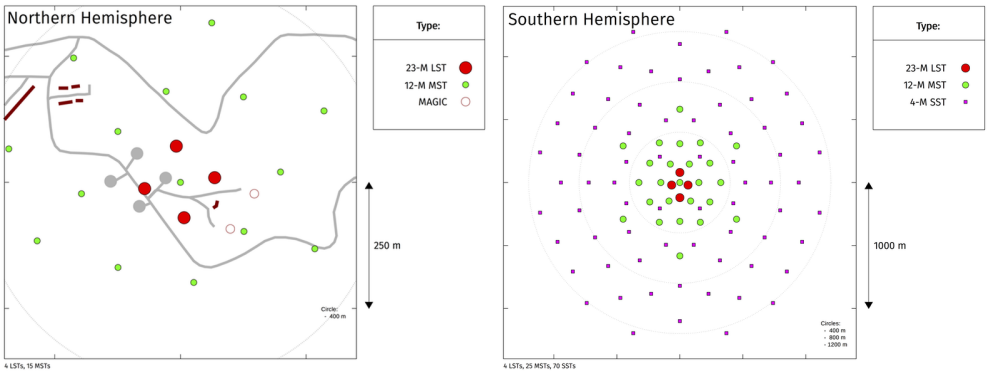

(A) Northern Array (B) Southern Array

FIGURE B.1: Expected layout of the CTA Observatories in the (left panel) Northern and Southern (right panel) Hemisphere. For the Northern Hemisphere the position of the present MAGIC experiment is highlighted.

B.2 The analytical parametrization of the Southern array

To extract the expected flux in a hypothetical observation from CTA, we used a parametrization of the expected collection area, the background rate, the energy resolution, and the energy bias. The collection area was described with a triple smooth broken power-law of the form:

$$A_{eff}(E) = A \left(\frac{E}{B_1}\right)^a \left(1 + \frac{E}{B_1}\right)^b \left(1 + \frac{E}{B_2}\right)^c \text{ m}^2 \tag{B.1}$$

where the parameters B_1 and B_2 are the positions of the breaks. The maximum difference between this curve and the actual estimate remains within 20%. From the parameters in Table B.1 one can already appreciate the potential of the instrument with respect to the *Fermi* satellite. The case in favour of ground based telescopes is in the much larger effective area: while *Fermi* can only count ~ 1 m^2 across the energy range (visible in Fig. 1.14a), due to the Cherenkov light pool having a radius of ~ 100 m, a ground based telescope can in principle detect $\sim 10^4$ more photons in the same time interval for energies below 100 GeV.

The background rate after gamma/hadron separation has been approximated instead with a simple power-law of the form:

$$B(E) = N \left(\frac{E}{0.1 \text{ TeV}}\right)^a \text{ Hz} \tag{B.2}$$

This parametrisation can instead be as far as 60% from the simulations of the actual estimated rate. However, the results are not strongly influenced by the actual level of background due to the extreme brightness of the sources investigated here. Only an

Effective area		
Parameter	0.5 hours	5 hours
A $[m^2]$	17461	22064
B_1 [TeV]	0.026	0.027
B_2 [TeV]	2.86	4.65
a	5.47	5.15
b	-4.29	-4.07
c	-1.23	-1.18

Table B.1: Parameters for the parametrization of the effective area for the 0.5 and 5 hours case.

Background level		
Parameter	0.5 hours	5 hours
N [Hz]	0.0255	0.0279
a	-1.717	-1.857

Table B.2: Parameters for the parametrization of the background level after cuts for the 0.5 and 5 hours case.

increase of several orders of magnitude in the background level would lead to noticeable effects on the results. The value of the parameters for these IRFs at 0.5 and 5 hours are reported in Tables B.1 and B.2.

The energy resolution was instead modelled using a smooth broken power-law:

$$\frac{\Delta E}{E} = 0.0468 \left(\frac{E}{0.64 \text{ TeV}}\right)^{-0.59} \left(1 + \frac{E}{0.64 \text{ TeV}}\right)^{0.69} \tag{B.3}$$

with a difference with the simulations of less than 8%. The energy bias was finally extracted from the migration matrix available together with the other IRFs of the Southern site and approximated with the exponential of a power-law function:

$$\frac{E_R - E_T}{E_T} = \exp\left[-\left(\frac{E_T}{0.023 \text{ TeV}}\right)^{2.43}\right] \tag{B.4}$$

where E_T is the true energy of the event and E_R is the reconstructed one. This function was able to approximate well the energy bias near threshold giving a value of the bias of 0.5 at 20 GeV, dropping quickly and becoming already negligible around 40 GeV. The outcome of these parametrizations is compared visually with the original CTA simulation in Figure B.2, where it is possible to note the agreement between the functions used and the original IRFs.

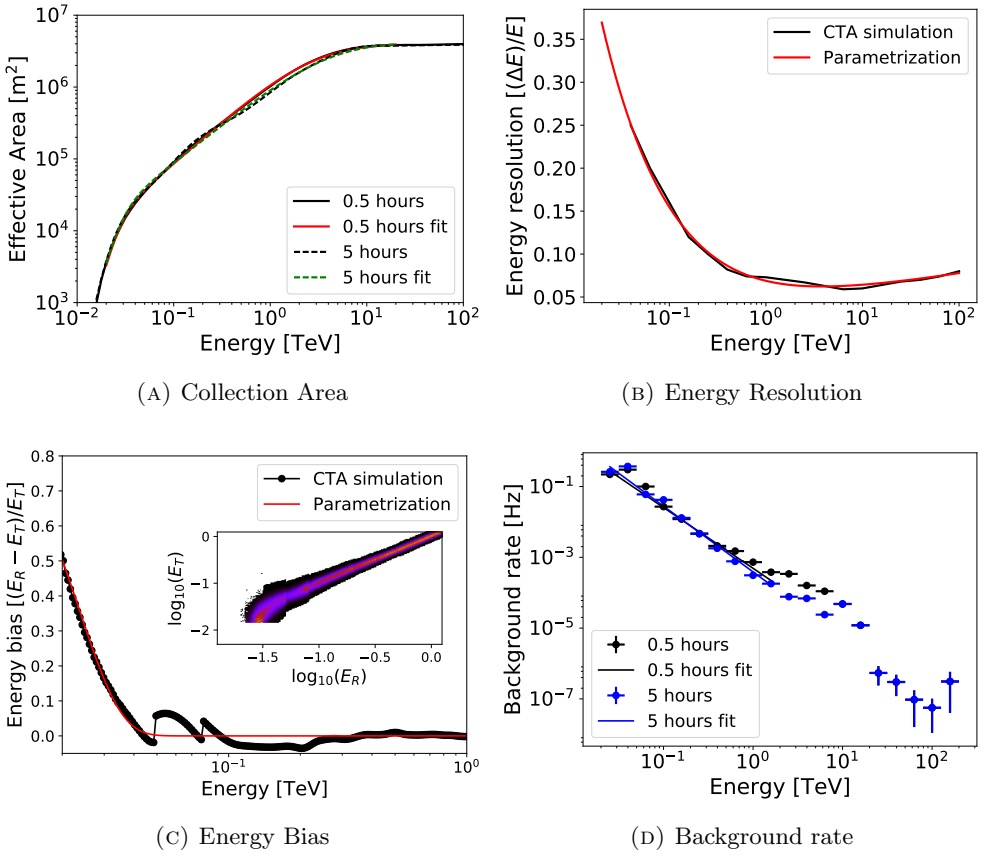

(A) Collection Area

(B) Energy Resolution

(C) Energy Bias

(D) Background rate

FIGURE B.2: Results of the parametrization of the CTA-South IRFs. On the top-left (B.2a): Parametrization of the collection area for the case of 0.5 (solid) and 5 hours(dashed). In black are the simulated curves provided by the CTA Collaboration, while the coloured ones are the result of the parametrization. Top right (B.2b): Energy resolution. In black the official curve and in red the parametrization. Bottom left (B.2c): in black energy bias curve extracted from the migration matrix provided by the CTA Collaboration and in red the parametrized curve. The sudden jumps seen in the black points are due to a change in the simulations in the original migration matrix, as visible from the inset. Bottom right (B.2d): back ground rate estimated in the case of 0.5 hours (black) and 5 hours (blue). The solid lines represent the power-law coming from the parametrization that was used in the analysis.

Appendix C

The analysis of Fermi-LAT data

Following the description of the Fermi-LAT instrument given in Section 1.6.1, I want to describe here the pipeline for the analysis of the Fermi-LAT data following the recommendations FSSC (Fermi Science Support Center)[1]

The *Fermi*-LAT data are publicly available in the form of photon lists as a `.fits` file (Flexible Image Transport System), a format widely spread in the astronomy community and it possible to download them from the data server website[2]. Together with the photon list, it is important to also download the spacecraft data file, another `.fits` file where all the data concerning the status of the spacecraft and the pointing position are stored. The analysis is then performed using a set of routines named *Science Tools*[3], which are based on the *ftools* used for the analysis of the data from other high-energy missions[4]. At the time of writing, the latest software version has the tag v10r0p5[5] with IRF version Pass 8 Release 2 Version 6[6].

C.1 Data cleaning

The first step is the data selection and cleaning. This is done through the `gtselect` routine, which filter the photon list in terms of data type, time interval, energy range and size of the region of the sky that is required for the analysis. Due to the large PSF,

[1] `http://fermi.gsfc.nasa.gov/ssc/` - accessed 26/05/2017

[2] `http://fermi.gsfc.nasa.gov/cgi-bin/ssc/LAT/LATDataQuery.cgi` - accessed 26/05/2017

[3] `http://fermi.gsfc.nasa.gov/ssc/data/analysis/scitools/overview.html` for a general overview and a list of the tools - accessed 26/05/2017

[4] `https://heasarc.gsfc.nasa.gov/ftools/ftools_menu.html` - accessed 26/05/2017

[5] `http://fermi.gsfc.nasa.gov/ssc/data/analysis/software/` - accessed 26/05/2017

[6] `http://www.slac.stanford.edu/exp/glast/groups/canda/lat_Performance.htm` - accessed 26/05/2017

up to 6° at 100 MeV, it is advisable to start with a region centred on the source with a size of 25°. With the latest version of the *Fermi*-LAT IRFs, there are different types of photons that can be selected, based on the background rejection, the accuracy in the direction reconstruction and the energy resolution[7]. The data type used throughout the thesis was the P8R2_SOURCE_V6, suitable for most of the analysis. The following step requires a further filtering according to the status of the instrument. This operation is performed using the `gtmktime` routine. The standard filter used to ensure the good quality of the data is given by the string "(DATA_QUAL>0) && (LAT_CONFIG==1)".

C.2 Final data reduction and likelihood fits

Once the data have been cleaned, the results on a specific source are obtained through a Maximum Likelihood fit. Before running the final fit, there are first some intermediate steps to be done. The first is to produce a *livetime cube* of the region of interest using `gtltcube`. This computes the exact live-time for each part of the sky that needs to be analysed. This step is needed due to the dependence of the effective area of the instrument with the angle between the source position and the axis of the spacecraft. Another parameter to take into account in this case is the maximum angle allowed for the integration of the live-time. To avoid the contamination of low energy gamma rays coming from the Earth limb, this is set to 90 degrees.

The actual data file used for the final analysis is a *count cube* which is a binned map in space and energy. This step is performed with the `gtbin` command. The typical size of the bins are: 0.2 degrees per bin for the spacial directions and 10 bins per decade on the energy axis. It is worth noting that this tool will produce a square region centred on the source position, while the initial selection is done on a circular portion of the sky. This square region is what in the following I will call the *Region of Interest* (ROI).

From these two steps, the *exposure cube* (via `gtexpcube2`) for each part of the sky at the various energy can be computed. Given the fact that the PSF of the instrument is quite poor at low energy, the *Fermi*-LAT Collaboration advises to compute the exposure for a much larger portion of the sky (up to 20 degrees more) to correctly take into account the emission from sources outside the chosen ROI, which might contaminate the reconstructed flux at low energy. At this point we explicitly define a model of the ROI, writing on a `.xml` file all the sources that might contribute to the ROI. In practical

[7] the list of all the available data types is at `https://fermi.gsfc.nasa.gov/ssc/data/analysis/documentation/Cicerone/Cicerone_Data/LAT_DP.html` with the recommended usage at `http://fermi.gsfc.nasa.gov/ssc/data/analysis/documentation/Cicerone/Cicerone_Data_Exploration/Data_preparation.html` - accessed 26/05/2017

terms, these are all the gamma-ray sources included in the field of view plus the sources outside it that can still give rise to relevant emission. Furthermore, we need to include the models for the diffuse emission: the one related to the galactic diffuse background and the one for the isotropic gamma-ray background (available on-line[8]). This step of producing the model is often done using the latest data products compiled by the *Fermi*-LAT Collaboration, like the latest version of the point source catalogue, the 3FGL [106] and the background models `gll_iem_v06.fits` and `iso_P8R2_SOURCE_V6_v06.txt`).

All these steps are required to compute a final *source map* (with `gtsrcmap`), which convolves the response functions for each of the sources defined in the model file. At this point the final fitting routine can take place.

C.2.1 The Maximum Likelihood fit

The Maximum Likelihood fit aims to find the best value of the model parameters in order to achieve the best agreement with the data. In general, the Likelihood function $\mathcal{L}$ is the product of the probabilities of all the observations according to the model we have chosen to test. In the case of counting experiments like *Fermi*-LAT, the probability distribution of detecting a certain amount of photons N_d, when the model predicts a number N_p is given by the Poissonian distribution:

$$P(N_d|N_p) = N_p^{N_d}\frac{e^{-N_p}}{N_d!} \tag{C.1}$$

so the likelihood function in our case is given by the product of all the probabilities associated to each bin i in space and energy:

$$\mathcal{L} = \prod_i N_{p_i}^{N_{d_i}}\frac{e^{-N_{p_i}}}{N_{d_i}!} = e^{-N_p}\prod_i \frac{N_{p_i}^{N_{d_i}}}{N_{d_i}!} \tag{C.2}$$

Because we are interested in finding the maximum of this function, for practical purposes it is preferable to use the $-\ln$ of C.2 to deal with sums instead of products and with a minimization instead of a maximization. As a side note, in a Gaussian approximation, the minimization of $-2\ln\mathcal{L}$ is equivalent to a χ^2 minimization.

An important parameter that can be computed via a likelihood fit is the so called *Loglikelihood ratio* for the comparison between models. Dealing with the logarithm of

[8] `https://fermi.gsfc.nasa.gov/ssc/data/access/lat/BackgroundModels.html` - accessed 26/05/2017

the Likelihood, it is possible to define the *Test Statistic* (TS) parameter:

$$TS = -2 \ln \left(\frac{\mathcal{L}(\theta_1 | H_1)}{\mathcal{L}(\theta_0 | H_0)} \right) \tag{C.3}$$

where with the sub-script 1 indicates the model with the hypothesis we want to test against the null one [209]. The Wilks's theorem [210] states that this quantity is asymptotically distributed as the χ^2 with a number of degrees of freedom equal to the difference between the number of free parameters between model H_1 and H_0 [211]. In the Likelihood fit routine implemented in the *Fermi*-LAT tools, it is possible to retrieve the TS value associated to the detection of each source in the model. As a first approximation, the square root of the TS value gives the significance of detection in units of standard deviations.

C.3 Practical use

Due to the high number of free parameters that is involved in a real analysis of the *Fermi*-LAT data (it can be up to > 50 free parameters), I follow the advice given by the *Fermi*-LAT team to do a first fit to remove sources that present a low detection significance (TS≤ 4) and only afterwards the final fit to obtain the best fit parameters with the relative uncertainties.

C.3.1 Generation of spectral points

Once the fit on the whole energy range is done, it is possible to obtain the spectral points via a new likelihood fit on each energy bin. To perform this step, the common procedure is to freeze all the sources in the model, leaving only the normalization of the source of interest free to vary. In the case of low significance energy intervals, where the TS value for the source is less than a certain threshold (usually set to a value of 9), $2\,\sigma$ upper limits are computed.

C.3.2 Generation of light curves

The generation of light-curves also requires a new likelihood fit of the data for each time bin we want to choose. However, in this case there is the additional aspect of the variability that has to be taken into account, not only for the source of interest (that is what we want to assess), but also for the surrounding sources. For this reason,

especially for the case of light curves on long time intervals (see the blazar MRK 501 case in Chapter 5), extra care must be taken in order to avoid that a flare from a nearby source could affect the estimate of the flux of our source of interest. When dealing with light curves sometimes it is also interesting to study the spectral variation of the source. However, this is only feasible if there is enough statistic in the time bin to leave the photon index as a free parameter. Also in the case of the light curve computation, it is common practice to compute $2\,\sigma$ flux upper limits in case the TS of the source is below threshold.

Appendix D

The analysis of H.E.S.S. data

In this Appendix I give some more details regarding the reduction and the analysis of the data coming from the H.E.S.S. array. For the part regarding the array in its phase I (4 small telescopes) I refer to [108]. A complete performance paper for the phase II has not been published yet, so I refer to the various conference proceedings and articles published so far where a description of the apparatus and the data analysis has been described.

D.1 From showers to fluxes, beyond the Hillas analysis

The starting point for a high level analysis is the separation between *gamma-like* and background events. The basic method is to use a parametrization of the shower image through the *Hillas parameters* (see 1.7.4). In the basic Hillas approach, the signal on the camera is first cleaned to retain only the compact image of the shower (with the exclusion of all the other pixels of the camera) and only at this point are the Hillas parameters used to reconstruct the physical quantities associated to the gamma ray. Within the H.E.S.S. Collaboration, more advanced methods have been implemented to boost the efficiency of the shower reconstruction and discrimination of hadronic background. The two main methods are the *Model* [90] and the *ImPACT* [91] reconstruction.

In the Model method (refer to [90]) the first step is to have semi-analytical model of the Cherenkov light associated to a gamma ray shower depending on different parameters like the zenith angle of the observation, different impact distances (projected distance on the ground between the direction of the shower and the telescope), energy of the gamma ray and the first interaction depth. The model template is then convolved with the camera response plus the NSB effect. This prediction is then compared to

the real signal on the camera and the optimal parameters are found through a log-likelihood fit over all the pixels, to obtain the 6 parameters characterizing the shower: 2 parameters for the direction, 2 for the position of the impact parameter on ground, depth of the first interaction and the energy of the primary gamma ray. The background (mostly due to charged particles) is rejected through the definition of *goodness-of-fit* variables that assess the quality of the fit through the comparison of the likelihood value for the camera signal given the best fit model, with the average value of the likelihood that can be obtained by the various realization of the model signal in the camera (average of the likelihood value $\ln \mathcal{L}(s|\mu)$ for each possible value of s given the effect of shower, NSB, and electronic noise). Only at this point is the image divided into pixels belonging to the shower-core and to the background. This goodness parameter can be used together with the total intensity of the shower image (in terms of photo-electrons) and the reconstructed interaction depth to define selection cuts with the aim of optimizing the detection significance for various type of sources.

Similarly, the ImPACT method (refer to [91]) requires the generation of templates to fit the camera data. In this approach however, the templates are generated using complete Montecarlo simulations, without the involvement of analytical or semi-analytical models. The likelihood fitting follows roughly the same procedure as for the Model method (same likelihood definition, but only on pixels related to the shower). A major difference is however the background rejection, which is not done through a goodness-of-the-fit variable, but through a boosted decision tree as the one described in [212]. This gives a "signal-likeness" parameter ζ used for the background discrimination and, together with other camera information, defines the various selection cuts.

The defined selection cuts are specifically optimized to have the maximum significance for a specific type of observed source. For the H.E.S.S.-I analysis there are 3 sets [108]:

- *Standard*, optimized for a source with the same spectrum as the Crab nebula (photon index $\alpha = -2.6$), but with a luminosity that is 10% of it;
- *Loose*, optimized for a bright source ($\sim$Crab flux), but with a steep photon index $\alpha = -3$;
- *Hard*, optimized for a source with 1% of the Crab flux and an hard photon index $\alpha = -2$.

The H.E.S.S. II MONO (and STEREO) selection cuts follow a similar philosophy, but the main difference between the selection cuts (called *Standard*, *Safe* and *Loose*) is in the minimum threshold for the reconstruction [92].

D.2 Background subtraction

After the selection cuts, a large amount of background still has to be removed. This is done by counting the number of events in a region of the sky around the source (the ON region) and the events in other patches of the sky around it (the OFF regions), with a rescaling given by the different solid angle covered. Two methods are implemented within the H.E.S.S. analysis framework: the *Ring* and the *Reflected* method, sketched in Figure D.1 [108]. In the Ring method the OFF region is given by an annulus around the ON region. The number of background counts is then weighted by the effects of radial acceptance of the camera. By moving ON and OFF regions over the entire field of view, it is possible to obtain a background subtracted estimate of the observed sky. For this reason this method is used when showing sky-maps.

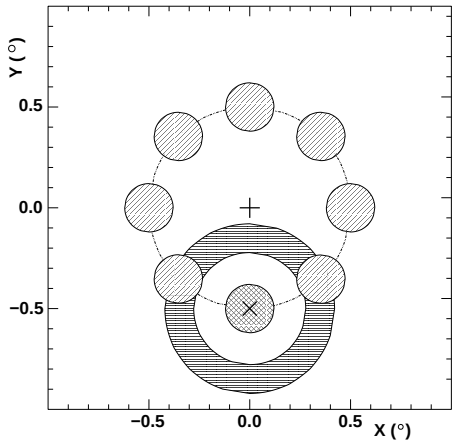

FIGURE D.1: Reflected and Ring Background subtraction methods. In the Ring Method the background is estimated in an OFF region shaped as an annulus around the source position. In the reflected method instead the there are multiple OFF regions at the same radial distance of the source (ON region) with respect to the pointing position of the camera. From [108].

The Reflected method instead takes advantage of the fact that the observations are taken in wobble mode, meaning that there is an offset between the pointing position of the telescope and the position of the source in the sky (usually this offset is between 0.5 and 0.7 degrees). As visible in Figure D.1, the OFF regions, are the reflection of the ON region and are positioned at the same offset from the centre of the camera to avoid corrections due to different radial acceptance. In normal observation conditions, possible non radial effects in the acceptance of the camera are taken into account by changing the wobbling direction every run. This method is the one used to provide the spectral reconstruction because it does not rely on any radial correction (which could be energy dependent) as in the Ring Background method.

D.3 Significance and flux reconstruction

Once the number of ON and OFF events is known, the significance of the source is computed using the expressions developed by Li and Ma [213], which takes into account the statistical fluctuations of both ON and OFF counts before computing the significance of the signal.

The final flux of the source and the spectrum are then computed taking into account the proper effective area of the instrument. This is computed via Montecarlo simulations and has a strong dependence on the energy of the photon and the zenith angle, which reduces the effective area at low energy, while increasing it at high energies.

The spectra are derived using *forward folding* techniques in which a certain spectral model is assumed and fitted to the data after being folded with the instrument response functions of the instrument (most importantly effective area and energy resolution).

The light-curves are constructed by computing the flux level in each temporal bin with the assumption of a certain spectral shape of the source, in a similar way as done with the *Fermi*-LAT data (see Appendix C).

Bibliography

[1] P. Morrison. On gamma-ray astronomy. *Il Nuovo Cimento*, 7:858–865, March 1958. doi: 10.1007/BF02745590.

[2] H. Hu. Status of the EAS studies of cosmic rays with energy below 10**16 eV. *ArXiv e-prints*, November 2009.

[3] A. M. Hillas. The Origin of Ultra-High-Energy Cosmic Rays. *ARA&A*, 22:425–444, 1984. doi: 10.1146/annurev.aa.22.090184.002233.

[4] K. V. Ptitsyna and S. V. Troitsky. PHYSICS OF OUR DAYS Physical conditions in potential accelerators of ultra-high-energy cosmic rays: updated Hillas plot and radiation-loss constraints. *Physics Uspekhi*, 53:691–701, October 2010. doi: 10.3367/UFNe.0180.201007c.0723.

[5] E. Fermi. On the Origin of the Cosmic Radiation. *Physical Review*, 75:1169–1174, April 1949. doi: 10.1103/PhysRev.75.1169.

[6] M. S. Longair. *High Energy Astrophysics*. Cambridge University Press, February 2011.

[7] W. I. Axford, E. Leer, and G. Skadron. The acceleration of cosmic rays by shock waves. *International Cosmic Ray Conference*, 11:132–137, 1977.

[8] G. F. Krymskii. A regular mechanism for the acceleration of charged particles on the front of a shock wave. *Akademiia Nauk SSSR Doklady*, 234:1306–1308, June 1977.

[9] A. R. Bell. The acceleration of cosmic rays in shock fronts. I. *MNRAS*, 182: 147–156, January 1978. doi: 10.1093/mnras/182.2.147.

[10] R. D. Blandford and J. P. Ostriker. Particle acceleration by astrophysical shocks. *ApJ*, 221:L29–L32, April 1978. doi: 10.1086/182658.

[11] A. R. Bell. Cosmic ray acceleration. *Astroparticle Physics*, 43:56–70, March 2013. doi: 10.1016/j.astropartphys.2012.05.022.

[12] V. Petrosian and A. M. Bykov. Particle Acceleration Mechanisms. *Space Sci. Rev.*, 134:207–227, February 2008. doi: 10.1007/s11214-008-9315-6.

[13] V. Petrosian. Stochastic Acceleration by Turbulence. *Space Sci. Rev.*, 173:535–556, November 2012. doi: 10.1007/s11214-012-9900-6.

[14] G. R. Blumenthal and R. J. Gould. Bremsstrahlung, Synchrotron Radiation, and Compton Scattering of High-Energy Electrons Traversing Dilute Gases. *Reviews of Modern Physics*, 42:237–271, 1970. doi: 10.1103/RevModPhys.42.237.

[15] G. B. Rybicki and A. P. Lightman. *Radiative processes in astrophysics*. Wiley-Interscience, 1979.

[16] A. Bettini. *Introduction to Elementary Particle Physics*. Cambridge University Press, July 2012.

[17] P. S. Coppi and R. D. Blandford. Reaction rates and energy distributions for elementary processes in relativistic pair plasmas. *MNRAS*, 245:453–507, August 1990.

[18] F. A. Aharonian and A. M. Atoyan. Compton scattering of relativistic electrons in compact X-ray sources. *Ap&SS*, 79:321–336, October 1981. doi: 10.1007/BF00649428.

[19] C. F. V. Weizsäcker. Ausstrahlung bei Stößen sehr schneller Elektronen. *Zeitschrift fur Physik*, 88:612–625, September 1934. doi: 10.1007/BF01333110.

[20] E. J. Williams. Correlation of certain collision problems with radiation theory. *Kong. Dan. Vid. Sel. Mat. Fys. Med.*, 13N4(4):1–50, 1935.

[21] J. D. Jackson and R. F. Fox. Classical Electrodynamics, 3rd ed. *American Journal of Physics*, 67:841–842, September 1999. doi: 10.1119/1.19136.

[22] W. Heitler. *Quantum theory of radiation*. Oxford University Press, 1954.

[23] F. A. Aharonian and A. V. Plyasheshnikov. Similarities and differences between relativistic electron-photon cascades developed in matter, photon gas and magnetic field. *Astroparticle Physics*, 19:525–548, July 2003. doi: 10.1016/S0927-6505(02)00239-6.

[24] M. S. Longair. *High energy astrophysics. Vol.2: Stars, the galaxy and the interstellar medium*. Cambridge University Press, 1994.

[25] F. Aharonian, L. Bergström, and C. Dermer. Astrophysics at Very High Energies. *Astrophysics at Very High Energies: Saas-Fee Advanced Course 40. Swiss Society for Astrophysics and Astronomy, Saas-Fee Advanced Course, Volume 40. ISBN 978-3-642-36133-3. Springer-Verlag Berlin Heidelberg, 2013*, 40, 2013. doi: 10.1007/978-3-642-36134-0.

[26] V. Anguelov and H. Vankov. Electromagnetic showers in a strong magnetic field. *Journal of Physics G Nuclear Physics*, 25:1755–1764, August 1999. doi: 10.1088/0954-3899/25/8/317.

[27] M. S. Zolotorev and K. T. McDonald. Classical Radiation Processes in the Weizsacker-Williams Approximation. *ArXiv Physics e-prints*, March 2000.

[28] F. A. Aharonian, S. R. Kelner, and A. Y. Prosekin. Angular, spectral, and time distributions of highest energy protons and associated secondary gamma rays and neutrinos propagating through extragalactic magnetic and radiation fields. *Phys. Rev. D*, 82(4):043002, August 2010. doi: 10.1103/PhysRevD.82.043002.

[29] S. Vernetto and P. Lipari. Absorption of very high energy gamma rays in the Milky Way. *Phys. Rev. D*, 94(6):063009, September 2016. doi: 10.1103/PhysRevD.94.063009.

[30] K. Mannheim. The proton blazar. *A&A*, 269:67–76, March 1993.

[31] G. Gamow and M. Schoenberg. Neutrino Theory of Stellar Collapse. *Physical Review*, 59:539–547, April 1941. doi: 10.1103/PhysRev.59.539.

[32] P. Haensel. URCA Processes in Dense Matter and Neutron Star Cooling. *Space Sci. Rev.*, 74:427–436, November 1995. doi: 10.1007/BF00751429.

[33] C. Patrignani and et al. (Particle Data Group). Review of Particle Physics. *Chinese Physics C*, 40(10):100001, October 2016. doi: 10.1088/1674-1137/40/10/100001.

[34] E. Kafexhiu, F. Aharonian, A. M. Taylor, and G. S. Vila. Parametrization of gamma-ray production cross sections for p p interactions in a broad proton energy range from the kinematic threshold to PeV energies. *Phys. Rev. D*, 90(12):123014, December 2014. doi: 10.1103/PhysRevD.90.123014.

[35] T. Sjöstrand, S. Mrenna, and P. Skands. PYTHIA 6.4 physics and manual. *Journal of High Energy Physics*, 5:026, May 2006. doi: 10.1088/1126-6708/2006/05/026.

[36] N. Gehrels and P. Mészáros. Gamma-Ray Bursts. *Science*, 337:932, August 2012. doi: 10.1126/science.1216793.

[37] R. W. Klebesadel, I. B. Strong, and R. A. Olson. Observations of Gamma-Ray Bursts of Cosmic Origin. *ApJ*, 182:L85, June 1973. doi: 10.1086/181225.

[38] E. Costa, F. Frontera, J. Heise, et al. Discovery of an X-ray afterglow associated with the γ-ray burst of 28 February 1997. *Nature*, 387:783–785, June 1997. doi: 10.1038/42885.

[39] C. Kouveliotou, C. A. Meegan, G. J. Fishman, et al. Identification of two classes of gamma-ray bursts. *ApJ*, 413:L101–L104, August 1993. doi: 10.1086/186969.

[40] F. Piron. Gamma-ray bursts at high and very high energies. *Comptes Rendus Physique*, 17:617–631, June 2016. doi: 10.1016/j.crhy.2016.04.005.

[41] B. P. Abbott, R. Abbott, T. D. Abbott, et al. Multi-messenger Observations of a Binary Neutron Star Merger. *ApJ*, 848:L12, October 2017. doi: 10.3847/2041-8213/aa91c9.

[42] K. I. Kellermann, J. J. Condon, A. E. Kimball, R. A. Perley, and Ž. Ivezić. Radio-loud and Radio-quiet QSOs. *ApJ*, 831:168, November 2016. doi: 10.3847/0004-637X/831/2/168.

[43] C. M. Urry and P. Padovani. Unified Schemes for Radio-Loud Active Galactic Nuclei. *PASP*, 107:803, September 1995. doi: 10.1086/133630.

[44] R. Antonucci. Unified models for active galactic nuclei and quasars. *ARA&A*, 31: 473–521, 1993. doi: 10.1146/annurev.aa.31.090193.002353.

[45] C. Zier and P. L. Biermann. Binary black holes and tori in AGN. II. Can stellar winds constitute a dusty torus? *A&A*, 396:91–108, December 2002. doi: 10.1051/0004-6361:20021339.

[46] F. Aharonian, A. G. Akhperjanian, G. Anton, et al. Simultaneous Observations of PKS 2155-304 with HESS, Fermi, RXTE, and Atom: Spectral Energy Distributions and Variability in a Low State. *ApJ*, 696:L150–L155, May 2009. doi: 10.1088/0004-637X/696/2/L150.

[47] H. Netzer. *The Physics and Evolution of Active Galactic Nuclei.* Cambridge University Press, November 2013.

[48] R. Antonucci. Active Galactic Nuclei and Quasars: Why Still a Puzzle after 50 years? *ArXiv e-prints*, January 2015.

[49] B. Punsly. The extended morphology of ultraluminous radio cores. *AJ*, 109: 1555–1575, April 1995. doi: 10.1086/117385.

[50] J. H. Fan and J. S. Zhang. The core dominance parameter of extragalactic radio sources. *A&A*, 407:899–904, September 2003. doi: 10.1051/0004-6361:20030896.

[51] B. L. Fanaroff and J. M. Riley. The morphology of extragalactic radio sources of high and low luminosity. *MNRAS*, 167:31P–36P, May 1974. doi: 10.1093/mnras/167.1.31P.

[52] P. Giommi, P. Padovani, G. Polenta, et al. A simplified view of blazars: clearing the fog around long-standing selection effects. *MNRAS*, 420:2899–2911, March 2012. doi: 10.1111/j.1365-2966.2011.20044.x.

[53] M. Ackermann, M. Ajello, W. B. Atwood, et al. The Third Catalog of Active Galactic Nuclei Detected by the Fermi Large Area Telescope. *ApJ*, 810:14, September 2015. doi: 10.1088/0004-637X/810/1/14.

[54] M. Sikora. Radiation processes in blazars. In C. D. Dermer, M. S. Strickman, and J. D. Kurfess, editors, *Proceedings of the Fourth Compton Symposium*, volume 410 of *American Institute of Physics Conference Series*, pages 494–505, May 1997. doi: 10.1063/1.54010.

[55] A. Franceschini, G. Rodighiero, and M. Vaccari. Extragalactic optical-infrared background radiation, its time evolution and the cosmic photon-photon opacity. *A&A*, 487:837–852, September 2008. doi: 10.1051/0004-6361:200809691.

[56] P. S. Coppi and F. A. Aharonian. Understanding the spectra of TeV blazars: implications for the cosmic infrared background. *Astroparticle Physics*, 11:35–39, June 1999. doi: 10.1016/S0927-6505(99)00021-3.

[57] L. Costamante. Gamma-Rays from Blazars and the Extragalactic Background Light. *International Journal of Modern Physics D*, 22:1330025-83, August 2013. doi: 10.1142/S0218271813300255.

[58] G. Dubus. Gamma-ray emission from binaries in context. *Comptes Rendus Physique*, 16:661–673, August 2015. doi: 10.1016/j.crhy.2015.08.014.

[59] G. Dubus. Gamma-ray binaries and related systems. *A&A Rev.*, 21:64, August 2013. doi: 10.1007/s00159-013-0064-5.

[60] P. Eger, H. Laffon, P. Bordas, et al. Discovery of a variable X-ray counterpart to HESS J1832-093: a new gamma-ray binary? *MNRAS*, 457:1753–1758, April 2016. doi: 10.1093/mnras/stw125.

[61] R. H. D. Corbet, L. Chomiuk, M. J. Coe, et al. A Luminous Gamma-ray Binary in the Large Magellanic Cloud. *ApJ*, 829:105, October 2016. doi: 10.3847/0004-637X/829/2/105.

[62] Mathieu de Naurois. The Very High Energy Sky from 20 GeV to Hundreds of TeV - Selected Highlights. *PoS*, ICRC2015:021, 2016.

[63] M. J. Aschwanden. Particle acceleration and kinematics in solar flares - A Synthesis of Recent Observations and Theoretical Concepts (Invited Review). *Space Sci. Rev.*, 101:1–227, January 2002. doi: 10.1023/A:1019712124366.

[64] A. O. Benz. Flare Observations. *Living Reviews in Solar Physics*, 14:2, December 2017. doi: 10.1007/s41116-016-0004-3.

[65] G. Kanbach, D. L. Bertsch, C. E. Fichtel, et al. Detection of a long-duration solar gamma-ray flare on June 11, 1991 with EGRET on COMPTON-GRO. *A&AS*, 97: 349–353, January 1993.

[66] V. V. Akimov, P. Ambrož, A. V. Belov, et al. Evidence for prolonged acceleration based on a detailed analysis of the long-duration solar gamma-ray flare of June 15, 1991. *Sol. Phys.*, 166:107–134, June 1996. doi: 10.1007/BF00179358.

[67] G. Rank, J. Ryan, H. Debrunner, M. McConnell, and V. Schönfelder. Extended gamma-ray emission of the solar flares in june 1991. *A&A*, 378:1046–1066, November 2001. doi: 10.1051/0004-6361:20011060.

[68] J. M. Ryan. Long-Duration Solar Gamma-Ray Flares. *Space Sci. Rev.*, 93:581–610, August 2000.

[69] L. Miroshnichenko, editor. *Solar Cosmic Rays*, volume 405 of *Astrophysics and Space Science Library*, 2015. doi: 10.1007/978-3-319-09429-8.

[70] R. A. Mewaldt, C. M. S. Cohen, A. W. Labrador, et al. Proton, helium, and electron spectra during the large solar particle events of October-November 2003. *Journal of Geophysical Research (Space Physics)*, 110:A09S18, September 2005. doi: 10.1029/2005JA011038.

[71] M.J. Berger, J.H. Hubbell, S.M. Seltzer, et al. Xcom: Photon cross section database (version 1.5)., 2010. URL `http://physics.nist.gov/xcom`. Accessed: [Thursday, 16-Feb-2017 08:15:45 EST].

[72] P. F. Michelson, W. B. Atwood, and S. Ritz. Fermi Gamma-ray Space Telescope: high-energy results from the first year. *Reports on Progress in Physics*, 73(7): 074901, July 2010. doi: 10.1088/0034-4885/73/7/074901.

[73] W. B. Atwood, A. A. Abdo, M. Ackermann, et al. The Large Area Telescope on the Fermi Gamma-Ray Space Telescope Mission. *ApJ*, 697:1071–1102, June 2009. doi: 10.1088/0004-637X/697/2/1071.

[74] M. Ackermann, M. Ajello, A. Albert, et al. The Fermi Large Area Telescope on Orbit: Event Classification, Instrument Response Functions, and Calibration. *ApJS*, 203:4, November 2012. doi: 10.1088/0067-0049/203/1/4.

[75] W. B. Atwood, R. Bagagli, L. Baldini, et al. Design and initial tests of the Tracker-converter of the Gamma-ray Large Area Space Telescope. *Astroparticle Physics*, 28:422–434, December 2007. doi: 10.1016/j.astropartphys.2007.08.010.

[76] W.N. Johnson, J.E. Grove, B.F. Phlips, J.P. Norris, and A.A. Moiseev. A CsI(tl) hodoscopic calorimeter for the GLAST mission. In *1997 IEEE Nuclear Science Symposium Conference Record*. Institute of Electrical and Electronics Engineers (IEEE), 1997. doi: 10.1109/nssmic.1997.672494. URL `https://doi.org/10.1109%2Fnssmic.1997.672494`.

[77] A. A. Moiseev, R. C. Hartman, J. F. Ormes, et al. The anti-coincidence detector for the GLAST large area telescope. *Astroparticle Physics*, 27:339–358, June 2007. doi: 10.1016/j.astropartphys.2006.12.003.

[78] J. Knödlseder. The future of gamma-ray astronomy. *Comptes Rendus Physique*, 17:663–678, June 2016. doi: 10.1016/j.crhy.2016.04.008.

[79] A. De Angelis, V. Tatischeff, M. Tavani, et al. The e-ASTROGAM mission (exploring the extreme Universe with gamma rays in the MeV-GeV range). *ArXiv e-prints*, November 2016.

[80] N. P. Topchiev, A. M. Galper, V. Bonvicini, et al. The GAMMA-400 gamma-ray telescope for precision gamma-ray emission investigations. In *Journal of Physics Conference Series*, volume 675 of *Journal of Physics Conference Series*, page 032009, February 2016. doi: 10.1088/1742-6596/675/3/032009.

[81] L. Baldini. Space-Based Cosmic-Ray and Gamma-Ray Detectors: a Review. *ArXiv e-prints*, July 2014.

[82] R. Engel, D. Heck, and T. Pierog. Extensive Air Showers and Hadronic Interactions at High Energy. *Annual Review of Nuclear and Particle Science*, 61:467–489, November 2011. doi: 10.1146/annurev.nucl.012809.104544.

[83] M. S. Longair. *High energy astrophysics. Vol.1: Particles, photons and their detection*. Cambridge University Press, March 1992.

[84] Andrew J. Smith. HAWC: Design, Operation, Reconstruction and Analysis. *PoS*, ICRC2015:966, 2016.

[85] A. U. Abeysekara, R. Alfaro, C. Alvarez, et al. Sensitivity of the high altitude water Cherenkov detector to sources of multi-TeV gamma rays. *Astroparticle Physics*, 50:26–32, December 2013. doi: 10.1016/j.astropartphys.2013.08.002.

[86] J. Holder. Atmospheric Cherenkov Gamma-ray Telescopes. *ArXiv e-prints*, October 2015.

[87] A. M. Hillas. Evolution of ground-based gamma-ray astronomy from the early days to the Cherenkov Telescope Arrays. *Astroparticle Physics*, 43:19–43, March 2013. doi: 10.1016/j.astropartphys.2012.06.002.

[88] A. M. Hillas. Cerenkov light images of EAS produced by primary gamma. *International Cosmic Ray Conference*, 3, August 1985.

[89] M. Holler, A. Balzer, R. Chalmé-Calvet, et al. Photon Reconstruction for H.E.S.S. Using a Semi-Analytical Shower Model. In *Proceedings of the 34th International Cosmic Ray Conference (ICRC 2015)*, volume ICRC2015, page 980, 2016.

[90] M. de Naurois and L. Rolland. A high performance likelihood reconstruction of γ-rays for imaging atmospheric Cherenkov telescopes. *Astroparticle Physics*, 32: 231–252, December 2009. doi: 10.1016/j.astropartphys.2009.09.001.

[91] R. D. Parsons and J. A. Hinton. A Monte Carlo template based analysis for air-Cherenkov arrays. *Astroparticle Physics*, 56:26–34, April 2014. doi: 10.1016/j.astropartphys.2014.03.002.

[92] R. D. Parsons, M. Gajdus, T. Murach, and for the H. E. S. S. collaboration. HESS II Data Analysis with ImPACT. In *Proceedings of the 34th International Cosmic Ray Conference (ICRC 2015)*, volume ICRC2015, page 826, 2016.

[93] M. Sharma, B. Chinmay, N. Bhatt, et al. Sensitivity estimate of the MACE gamma ray telescope. *Nuclear Instruments and Methods in Physics Research A*, 851:125–131, April 2017. doi: 10.1016/j.nima.2017.01.005.

[94] M. Tluczykont, D. Hampf, D. Horns, et al. The HiSCORE concept for gamma-ray and cosmic-ray astrophysics beyond 10 TeV. *Astroparticle Physics*, 56:42–53, April 2014. doi: 10.1016/j.astropartphys.2014.03.004.

[95] G. Di Sciascio and on behalf of the LHAASO Collaboration. The LHAASO experiment: from Gamma-Ray Astronomy to Cosmic Rays. *ArXiv e-prints*, February 2016.

[96] H.E.S.S. Collaboration, H. Abdalla, A. Abramowski, et al. Gamma-ray blazar spectra with H.E.S.S. II mono analysis: The case of PKS 2155-304 and PG 1553+113. *A&A*, 600:A89, April 2017. doi: 10.1051/0004-6361/201629427.

[97] R. Ganguly, R. S. Lynch, J. C. Charlton, et al. A census of quasar-intrinsic absorption in the Hubble Space Telescope archive: systems from high-resolution echelle spectra. *MNRAS*, 435:1233–1264, October 2013. doi: 10.1093/mnras/stt1366.

[98] H. E. S. S. Collaboration, H. Abdalla, A. Abramowski, et al. Characterizing the γ-ray long-term variability of PKS 2155-304 with H.E.S.S. and Fermi-LAT. *A&A*, 598:A39, January 2017. doi: 10.1051/0004-6361/201629419.

[99] P. M. Chadwick, K. Lyons, T. J. L. McComb, et al. Very High Energy Gamma Rays from PKS 2155-304. *ApJ*, 513:161–167, March 1999. doi: 10.1086/306862.

[100] F. Aharonian, A. G. Akhperjanian, K.-M. Aye, et al. H.E.S.S. observations of PKS 2155-304. *A&A*, 430:865–875, February 2005. doi: 10.1051/0004-6361:20041853.

[101] H.E.S.S. Collaboration, A. Abramowski, F. Acero, et al. VHE γ-ray emission of PKS 2155-304: spectral and temporal variability. *A&A*, 520:A83, September 2010. doi: 10.1051/0004-6361/201014484.

[102] F. Aharonian, A. G. Akhperjanian, A. R. Bazer-Bachi, et al. Evidence for VHE γ-ray emission from the distant BL Lac PG 1553+113. *A&A*, 448:L19–L23, March 2006. doi: 10.1051/0004-6361:200600010.

[103] J. Albert, E. Aliu, H. Anderhub, et al. Detection of Very High Energy Radiation from the BL Lacertae Object PG 1553+113 with the MAGIC Telescope. *ApJ*, 654:L119–L122, January 2007. doi: 10.1086/511384.

[104] A. Abramowski, F. Aharonian, F. Ait Benkhali, et al. The 2012 Flare of PG 1553+113 Seen with H.E.S.S. and Fermi-LAT. *ApJ*, 802:65, March 2015. doi: 10.1088/0004-637X/802/1/65.

[105] C. W. Danforth, B. A. Keeney, J. T. Stocke, J. M. Shull, and Y. Yao. Hubble/COS Observations of the Lyα Forest Toward the BL Lac Object 1ES 1553+113. *ApJ*, 720:976–986, September 2010. doi: 10.1088/0004-637X/720/1/976.

[106] F. Acero, M. Ackermann, M. Ajello, et al. Fermi Large Area Telescope Third Source Catalog. *ApJS*, 218:23, June 2015. doi: 10.1088/0067-0049/218/2/23.

[107] D. Berge, S. Funk, and J. Hinton. Background modelling in very-high-energy γ-ray astronomy. *A&A*, 466:1219–1229, May 2007. doi: 10.1051/0004-6361:20066674.

[108] F. Aharonian, A. G. Akhperjanian, A. R. Bazer-Bachi, et al. Observations of the Crab nebula with HESS. *A&A*, 457:899–915, October 2006. doi: 10.1051/0004-6361:20065351.

[109] K. Bernlöhr. Simulation of imaging atmospheric Cherenkov telescopes with CORSIKA and sim_ telarray. *Astroparticle Physics*, 30:149–158, October 2008. doi: 10.1016/j.astropartphys.2008.07.009.

[110] D. A. Sanchez and C. Deil. Enrico : a Python package to simplify Fermi-LAT analysis. In *Proceedings, 33rd International Cosmic Ray Conference (ICRC2013)*, page 0089, 2013.

[111] F. Acero, M. Ackermann, M. Ajello, et al. Development of the Model of Galactic Interstellar Emission for Standard Point-source Analysis of Fermi Large Area Telescope Data. *ApJS*, 223:26, April 2016. doi: 10.3847/0067-0049/223/2/26.

[112] M. Ackermann, M. Ajello, A. Allafort, et al. The First Fermi-LAT Catalog of Sources above 10 GeV. *ApJS*, 209:34, December 2013. doi: 10.1088/0067-0049/209/2/34.

[113] M. Ackermann, M. Ajello, W. B. Atwood, et al. 2FHL: The Second Catalog of Hard Fermi-LAT Sources. *ApJS*, 222:5, January 2016. doi: 10.3847/0067-0049/222/1/5.

[114] C. Romoli, P. Bordas, C. Mariaud, et al. H.E.S.S. observations of PSR B1259-63 during its 2014 periastron passage. In *Proceedings of the 34th International Cosmic Ray Conference (ICRC 2015)*, volume ICRC2015, page 873, 2016.

[115] P. Bordas, G. Dubus, P. Eger, et al. Observations of Binary Systems with the H.E.S.S. Telescopes. In *Proceedings, 6th International Symposium on High-Energy Gamma-Ray Astronomy (Gamma 2016)*, volume 1792, page 040017, 2017. doi: 10.1063/1.4968921.

[116] S. Johnston, R. N. Manchester, A. G. Lyne, et al. PSR 1259-63 - A binary radio pulsar with a Be star companion. *ApJ*, 387:L37–L41, March 1992. doi: 10.1086/186300.

[117] I. Negueruela, M. Ribó, A. Herrero, et al. Astrophysical Parameters of LS 2883 and Implications for the PSR B1259-63 Gamma-ray Binary. *ApJ*, 732:L11, May 2011. doi: 10.1088/2041-8205/732/1/L11.

[118] M. Chernyakova, A. A. Abdo, A. Neronov, et al. Multiwavelength observations of the binary system PSR B1259-63/LS 2883 around the 2010-2011 periastron passage. *MNRAS*, 439:432–445, March 2014. doi: 10.1093/mnras/stu021.

[119] N. Wex, S. Johnston, R. N. Manchester, et al. Timing models for the long orbital period binary pulsar PSR B1259-63. *MNRAS*, 298:997–1004, August 1998. doi: 10.1046/j.1365-8711.1998.01700.x.

[120] N. Wang, S. Johnston, and R. N. Manchester. 13 years of timing of PSR B1259-63. *MNRAS*, 351:599–606, June 2004. doi: 10.1111/j.1365-2966.2004.07806.x.

[121] F. Aharonian, A. G. Akhperjanian, K.-M. Aye, et al. Discovery of the binary pulsar PSR B1259-63 in very-high-energy gamma rays around periastron with HESS. *A&A*, 442:1–10, October 2005. doi: 10.1051/0004-6361:20052983.

[122] S. Johnston, R. N. Manchester, A. G. Lyne, et al. Radio observations of PSR B1259-63 around periastron. *MNRAS*, 279:1026–1036, April 1996. doi: 10.1093/mnras/279.3.1026.

[123] F. Aharonian, A. G. Akhperjanian, G. Anton, et al. Very high energy γ-ray observations of the binary PSR B1259-63/SS2883 around the 2007 Periastron. *A&A*, 507:389–396, November 2009. doi: 10.1051/0004-6361/200912339.

[124] H.E.S.S. Collaboration, A. Abramowski, F. Acero, et al. H.E.S.S. observations of the binary system PSR B1259-63/LS 2883 around the 2010/2011 periastron passage. *A&A*, 551:A94, March 2013. doi: 10.1051/0004-6361/201220612.

[125] P. H. T. Tam, R. H. H. Huang, J. Takata, et al. Discovery of GeV γ-ray Emission from PSR B1259-63/LS 2883. *ApJ*, 736:L10, July 2011. doi: 10.1088/2041-8205/736/1/L10.

[126] A. A. Abdo, M. Ackermann, M. Ajello, et al. Discovery of High-energy Gamma-ray Emission from the Binary System PSR B1259-63/LS 2883 around Periastron with Fermi. *ApJ*, 736:L11, July 2011. doi: 10.1088/2041-8205/736/1/L11.

[127] M. Chernyakova, A. Neronov, B. van Soelen, et al. Multi-wavelength observations of the binary system PSR B1259-63/LS 2883 around the 2014 periastron passage. *MNRAS*, 454:1358–1370, December 2015. doi: 10.1093/mnras/stv1988.

[128] D. Khangulyan, F. A. Aharonian, S. V. Bogovalov, and M. Ribó. Gamma-Ray Signal from the Pulsar Wind in the Binary Pulsar System PSR B1259-63/LS 2883. *ApJ*, 742:98, December 2011. doi: 10.1088/0004-637X/742/2/98.

[129] D. Khangulyan, F. A. Aharonian, S. V. Bogovalov, and M. Ribó. Post-periastron Gamma-Ray Flare from PSR B1259-63/LS 2883 as a Result of Comptonization of the Cold Pulsar Wind. *ApJ*, 752:L17, June 2012. doi: 10.1088/2041-8205/752/1/L17.

[130] G. A. Caliandro, C. C. Cheung, J. Li, et al. Gamma-Ray Flare Activity from PSR B1259-63 during 2014 Periastron Passage and Comparison to Its 2010 Passage. *ApJ*, 811:68, September 2015. doi: 10.1088/0004-637X/811/1/68.

[131] C. Romoli, P. Bordas, C. Mariaud, and T. Murach. H.E.S.S. II observations of the 2014 periastron passage of PSR B1259−63/LS2883. *PoS*, ICRC2017, 2017.

[132] E. Kafexhiu, C. Romoli, A. M. Taylor, and F. Aharonian. Energetic gamma-ray emission from solar flares. *ArXiv e-prints*, March 2018. submitted to ApJ.

[133] K. Lodders, H. Palme, and H.-P. Gail. Abundances of the Elements in the Solar System. *Landolt Börnstein*, 2009. doi: 10.1007/978-3-540-88055-4_34.

[134] H. Nifenecker and J. A. Pinston. High energy gamma-ray production in nuclear reactions. *Progress in Particle and Nuclear Physics*, 23:271–355, 1989. doi: 10.1016/0146-6410(89)90011-2.

[135] W. Cassing, V. Metag, U. Mosel, and K. Niita. Production of energetic particles in heavy-ion collisions. *Phys. Rep.*, 188:363–449, April 1990. doi: 10.1016/0370-1573(90)90164-W.

[136] Y. Schutz, G. Martínez, F. M. Marqués, et al. Hard photons and neutral pions as probes of hot and dense nuclear matter. *Nuclear Physics A*, 622:404–477, February 1997. doi: 10.1016/S0375-9474(97)00191-7.

[137] P. Grimm and E. Grosse. Pions and hard photons as probes for nucleus-nucleus collisions. *Progress in Particle and Nuclear Physics*, 15:339–351, 1985. doi: 10.1016/0146-6410(85)90073-0.

[138] E. Grosse. Subthreshold pion production in nucleus-nucleus collisions. *Nuclear Physics A*, 447:611–623, January 1986. doi: 10.1016/0375-9474(86)90637-8.

[139] S. Hilaire A.J. Koning and M.C. Duijvestijn. Talys-1.0. pages 211 – 214, April 2007. URL `http://www.talys.eu/`.

[140] R. Ramaty, B. Kozlovsky, and R. E. Lingenfelter. Nuclear gamma-rays from energetic particle interactions. *ApJS*, 40:487–526, July 1979. doi: 10.1086/190596.

[141] R.-z. Yang, E. Kafexhiu, and F. Aharonian. On the shape of the gamma-ray spectrum around the "π^0-bump". *ArXiv e-prints*, March 2018.

[142] E. Kafexhiu. Parametrization of the nucleus-nucleus γ -ray production cross sections below 100 GeV/nucleon: Subthreshold pions and hard photons. *Phys. Rev. C*, 94(6):064603, December 2016. doi: 10.1103/PhysRevC.94.064603.

[143] M. Ackermann, M. Ajello, A. Albert, et al. High-energy Gamma-Ray Emission from Solar Flares: Summary of Fermi Large Area Telescope Detections and Analysis of Two M-class Flares. *ApJ*, 787:15, May 2014. doi: 10.1088/0004-637X/787/1/15.

[144] M. Ajello, A. Albert, A. Allafort, et al. Impulsive and Long Duration High-energy Gamma-Ray Emission from the Very Bright 2012 March 7 Solar Flares. *ApJ*, 789:20, July 2014. doi: 10.1088/0004-637X/789/1/20.

[145] M. Pesce-Rollins, N. Omodei, V. Petrosian, et al. First Detection of ¿100 MeV Gamma-Rays Associated with a Behind-the-limb Solar Flare. *ApJ*, 805:L15, June 2015. doi: 10.1088/2041-8205/805/2/L15.

[146] C. Geyer. *Handbook of Markov Chain Monte Carlo*, chapter 1 - Introduction to MCMC. Chapman & Hall/CRC Handbooks of Modern Statistical Methods. CRC Press, 2011. ISBN 9781420079425.

[147] W. K. Hastings. Monte carlo sampling methods using markov chains and their applications. *Biometrika*, 57(1):97, 1970.

[148] G. A. Barnard and Thomas Bayes. Studies in the History of Probability and Statistics: IX. Thomas Bayes's Essay Towards Solving a Problem in the Doctrine of Chances. *Biometrika*, 45(3/4):293–315, 1958. ISSN 00063444. URL `http://www.jstor.org/stable/2333180`.

[149] D. Foreman-Mackey, D. W. Hogg, D. Lang, and J. Goodman. emcee: The MCMC Hammer. *PASP*, 125:306–312, March 2013. doi: 10.1086/670067.

[150] J. Goodman and J. Weare. Ensemble samplers with affine invariance. *Communications in Applied Mathematics and Computational Science*, 5:65–80, 2010. doi: 10.2140/camcos.2010.5.65.

[151] V. Zabalza. naima: a python package for inference of relativistic particle energy distributions from observed nonthermal spectra. *Proc. of International Cosmic Ray Conference 2015*, page 922, 2015.

[152] R. J. Murphy, C. D. Dermer, and R. Ramaty. High-energy processes in solar flares. *ApJS*, 63:721–748, March 1987. doi: 10.1086/191180.

[153] B. E. Markarian. Galaxies with an Ultraviolet Continuum. *Astrofizika*, 3, 1967.

[154] J. Quinn, C. W. Akerlof, S. Biller, et al. Detection of Gamma Rays with E $>$ 300 GeV from Markarian 501. *ApJ*, 456:L83, January 1996. doi: 10.1086/309878.

[155] F. A. Aharonian, A. G. Akhperjanian, J. A. Barrio, et al. The time averaged TeV energy spectrum of MKN 501 of the extraordinary 1997 outburst as measured with the stereoscopic Cherenkov telescope system of HEGRA. *A&A*, 349:11–28, September 1999.

[156] E. Aliu, S. Archambault, A. Archer, et al. Very high energy outburst of Markarian 501 in May 2009. *A&A*, 594:A76, October 2016. doi: 10.1051/0004-6361/201628744.

[157] G. Cologna, N. Chakraborty, M. Mohamed, et al. Spectral characteristics of Mrk 501 during the 2012 and 2014 flaring states. In *Proceedings, 34th International Cosmic Ray Conference (ICRC 2015)*, volume ICRC2015, page 761, 2016.

[158] J. Albert, E. Aliu, H. Anderhub, et al. Variable Very High Energy γ-Ray Emission from Markarian 501. *ApJ*, 669:862–883, November 2007. doi: 10.1086/521382.

[159] N. Chakraborty, G. Cologna, M. A. Kastendieck, et al. Rapid variability at very high energies in Mrk 501. In *Proceedings, 34th International Cosmic Ray Conference (ICRC 2015): The Hague, The Netherlands*, volume ICRC2015, page 872, 2016.

[160] A. Neronov, D. Semikoz, and A. M. Taylor. Very hard gamma-ray emission from a flare of Mrk 501. *A&A*, 541:A31, May 2012. doi: 10.1051/0004-6361/201117083.

[161] A. Shukla, K. Mannheim, V. R. Chitnis, et al. Detection of Very Hard γ-Ray Spectrum from the TeV Blazar Mrk 501. *ApJ*, 832:177, December 2016. doi: 10.3847/0004-637X/832/2/177.

[162] E. Lefa, F. M. Rieger, and F. Aharonian. Formation of Very Hard Gamma-Ray Spectra of Blazars in Leptonic Models. *ApJ*, 740:64, October 2011. doi: 10.1088/0004-637X/740/2/64.

[163] E. Lefa, F. A. Aharonian, and F. M. Rieger. "Leading Blob" Model in a Stochastic Acceleration Scenario: The Case of the 2009 Flare of Mkn 501. *ApJ*, 743:L19, December 2011. doi: 10.1088/2041-8205/743/1/L19.

[164] G. Cao and J. Wang. The Hadronic Origin of the Hard Gamma-Ray Spectrum from Blazar 1ES 1101-232. *ApJ*, 783:108, March 2014. doi: 10.1088/0004-637X/783/2/108.

[165] A. Shukla, V. R. Chitnis, B. B. Singh, et al. Multi-frequency, Multi-epoch Study of Mrk 501: Hints for a Two-component Nature of the Emission. *ApJ*, 798:2, January 2015. doi: 10.1088/0004-637X/798/1/2.

[166] S. Koyama, M. Kino, M. Giroletti, et al. Discovery of off-axis jet structure of TeV blazar Mrk 501 with mm-VLBI. *A&A*, 586:A113, February 2016. doi: 10.1051/0004-6361/201526541.

[167] N. Gehrels. Confidence limits for small numbers of events in astrophysical data. *ApJ*, 303:336–346, April 1986. doi: 10.1086/164079.

[168] R. Barlow. Asymmetric Statistical Errors. *ArXiv Physics e-prints*, June 2004.

[169] S. Vaughan, R. Edelson, R. S. Warwick, and P. Uttley. On characterizing the variability properties of X-ray light curves from active galaxies. *MNRAS*, 345: 1271–1284, November 2003. doi: 10.1046/j.1365-2966.2003.07042.x.

[170] H. Anderhub, M. Backes, A. Biland, et al. Design and operation of FACT - the first G-APD Cherenkov telescope. *Journal of Instrumentation*, 8:P06008, June 2013. doi: 10.1088/1748-0221/8/06/P06008.

[171] A. Biland, T. Bretz, J. Buß, et al. Calibration and performance of the photon sensor response of FACT – the first G-APD Cherenkov telescope. *Journal of Instrumentation*, 9:P10012, October 2014. doi: 10.1088/1748-0221/9/10/P10012.

[172] C. Romoli, A. M. Taylor, and F. Aharonian. Cut-off characterisation of energy spectra of bright fermi sources: Current instrument limits and future possibilities. *Astroparticle Physics*, 88:38–45, February 2017. doi: 10.1016/j.astropartphys.2016.12.007.

[173] C. M. Bender and S. A. Orszag. *Advanced mathematical methods for scientists and engineers I: asymptotic methods and perturbation theory.* Springer-Verlag, 1999.

[174] Inc. Wolfram Research. Mathematica. Wolfram Research, Inc., 2012. Version 9.0.

[175] V. N. Zirakashvili and F. Aharonian. Analytical solutions for energy spectra of electrons accelerated by nonrelativistic shock-waves in shell type supernova remnants. *A&A*, 465:695–702, April 2007. doi: 10.1051/0004-6361:20066494.

[176] R. Schlickeiser. A viable mechanism to establish relativistic thermal particle distribution functions in cosmic sources. *A&A*, 143:431–434, February 1985.

[177] F. A. Aharonian, A. M. Atoyan, and A. Nahapetian. The possible acceleration mechanism leading to the formation of Maxwell-like spectra of relativistic electrons in turbulent synchrotron sources. *A&A*, 162:L1, July 1986.

[178] Ł. Stawarz and V. Petrosian. On the Momentum Diffusion of Radiating Ultrarelativistic Electrons in a Turbulent Magnetic Field. *ApJ*, 681:1725–1744, July 2008. doi: 10.1086/588813.

[179] K. D. Fritz. Synchrotron emission spectra from shockwaves in active galactic nuclei - an energy and space dependent diffusion coefficient. *A&A*, 214:14–28, April 1989.

[180] E. Lefa, S. R. Kelner, and F. A. Aharonian. On the Spectral Shape of Radiation due to Inverse Compton Scattering Close to the Maximum Cutoff. *ApJ*, 753:176, July 2012. doi: 10.1088/0004-637X/753/2/176.

[181] S. R. Kelner, F. A. Aharonian, and V. V. Bugayov. Energy spectra of gamma rays, electrons, and neutrinos produced at proton-proton interactions in the very high energy regime. *Phys. Rev. D*, 74(3):034018, August 2006. doi: 10.1103/PhysRevD.74.034018.

[182] A. A. Abdo, M. Ackermann, M. Ajello, et al. The Vela Pulsar: Results from the First Year of Fermi LAT Observations. *ApJ*, 713:154–165, April 2010. doi: 10.1088/0004-637X/713/1/154.

[183] A. A. Abdo, M. Ajello, A. Allafort, et al. The Second Fermi Large Area Telescope Catalog of Gamma-Ray Pulsars. *ApJS*, 208:17, October 2013. doi: 10.1088/0067-0049/208/2/17.

[184] S. R. Kelner, A. Y. Prosekin, and F. A. Aharonian. Synchro-Curvature Radiation of Charged Particles in the Strong Curved Magnetic Fields. *AJ*, 149:33, January 2015. doi: 10.1088/0004-6256/149/1/33.

[185] A. A. Abdo, M. Ackermann, M. Ajello, et al. Fermi Gamma-ray Space Telescope Observations of the Gamma-ray Outburst from 3C454.3 in November 2010. *ApJ*, 733:L26, June 2011. doi: 10.1088/2041-8205/733/2/L26.

[186] D. V. Khangulyan, M. V. Barkov, V. Bosch-Ramon, F. A. Aharonian, and A. V. Dorodnitsyn. Star-Jet Interactions and Gamma-Ray Outbursts from 3C454.3. *ApJ*, 774:113, September 2013. doi: 10.1088/0004-637X/774/2/113.

[187] R. C. Hartman, D. L. Bertsch, C. E. Fichtel, et al. Detection of high-energy gamma radiation from quasar 3C 279 by the EGRET telescope on the Compton Gamma Ray Observatory. *ApJ*, 385:L1–L4, January 1992. doi: 10.1086/186263.

[188] C. R. Lynds, A. N. Stockton, and W. C. Livingston. New Spectroscope Observations of Quasi-Stellar Sources. *ApJ*, 142:1667, November 1965. doi: 10.1086/148457.

[189] F. Lucarelli, C. Pittori, F. Verrecchia, et al. AGILE detection of a bright gamma-ray flare from the blazar 3C 279. *The Astronomer's Telegram*, 7631, June 2015.

[190] S. Cutini. Fermi LAT detection of renewed and strong GeV activity from blazar 3C 279. *The Astronomer's Telegram*, 7633, June 2015.

[191] M. Ackermann, R. Anantua, K. Asano, et al. Minute-timescale >100 MeV γ-Ray Variability during the Giant Outburst of Quasar 3C 279 Observed by Fermi-LAT in 2015 June. *ApJ*, 824:L20, June 2016. doi: 10.3847/2041-8205/824/2/L20.

[192] V. S. Paliya. Fermi-Large Area Telescope Observations of the Exceptional Gamma-Ray Flare from 3C 279 in 2015 June. *ApJ*, 808:L48, August 2015. doi: 10.1088/2041-8205/808/2/L48.

[193] C. Pittori, F. Verrecchia, S. Puccetti, M. Perri, and M. Tavani. Update on Swift follow-up observations of the GeV flaring blazar 3C 279. *The Astronomer's Telegram*, 7668, June 2015.

[194] M. Doro and MAGIC Collaboration. Reaching the lowest energy threshold of ground-based Cherenkov telescopes with MAGIC-stereo: A goal achieved. *Nuclear Instruments and Methods in Physics Research A*, 692:201–207, November 2012. doi: 10.1016/j.nima.2011.12.115.

[195] Djannati-Ataï, A. and Giavitto, G. and Holler, M. and Rudak, B. and Venter, C. Probing Vela pulsar down to 20 GeV with H.E.S.S. II observations. *AIP Conf. Proc.*, 1792(1):040028, 2017. doi: 10.1063/1.4968932.

[196] K. Bernlöhr, A. Barnacka, Y. Becherini, et al. Monte Carlo design studies for the Cherenkov Telescope Array. *Astroparticle Physics*, 43:171–188, March 2013. doi: 10.1016/j.astropartphys.2012.10.002.

[197] Tim Adye. Unfolding algorithms and tests using RooUnfold. In *Proceedings of the PHYSTAT 2011 Workshop, CERN, Geneva, Switzerland, January 2011, CERN-2011-006*, pages 313–318, 2011. URL `http://inspirehep.net/record/898599/files/arXiv:1105.1160.pdf`.

[198] R. P. Kraft, D. N. Burrows, and J. A. Nousek. Determination of confidence limits for experiments with low numbers of counts. *ApJ*, 374:344–355, June 1991. doi: 10.1086/170124.

[199] M. Cerruti, M. Böttcher, N. Chakraborty, et al. Target of Opportunity observations of blazars with H.E.S.S. In *Proceedings, 6th International Symposium on*

High-Energy Gamma-Ray Astronomy (Gamma 2016), volume 1792, page 050029, 2017. doi: 10.1063/1.4968975.

[200] Andrew M. Taylor. New developments in AGN gamma-ray astrophysics. *AIP Conf. Proc.*, 1792(1):020016, 2017. doi: 10.1063/1.4968901.

[201] A. Carosi et al. Recent follow-up observations of GRBs in the very high energy band with the MAGIC Telescopes. In *Proceedings of the 34th International Cosmic Ray Conference (ICRC 2015)*, volume ICRC2015, page 809, 2016.

[202] R. Parsons et al. The H.E.S.S. II GRB Program. In *Proceedings of the 34th International Cosmic Ray Conference (ICRC 2015)*, volume ICRC2015, page 853, 2016.

[203] M. Ackermann, M. Ajello, K. Asano, et al. The First Fermi-LAT Gamma-Ray Burst Catalog. *ApJS*, 209:11, November 2013. doi: 10.1088/0067-0049/209/1/11.

[204] M. Ackermann, M. Ajello, K. Asano, et al. Detection of a Spectral Break in the Extra Hard Component of GRB 090926A. *ApJ*, 729:114, March 2011. doi: 10.1088/0004-637X/729/2/114.

[205] R. M. Kulsrud. *Plasma Physics for Astrophysics*, chapter 12. Princeton University Press, 2005.

[206] L. O. Drury. An introduction to the theory of diffusive shock acceleration of energetic particles in tenuous plasmas. *Reports on Progress in Physics*, 46:973–1027, August 1983. doi: 10.1088/0034-4885/46/8/002.

[207] P. A. Becker, T. Le, and C. D. Dermer. Time-dependent Stochastic Particle Acceleration in Astrophysical Plasmas: Exact Solutions Including Momentum-dependent Escape. *ApJ*, 647:539–551, August 2006. doi: 10.1086/505319.

[208] M. Actis, G. Agnetta, F. Aharonian, et al. Design concepts for the Cherenkov Telescope Array CTA: an advanced facility for ground-based high-energy gamma-ray astronomy. *Experimental Astronomy*, 32:193–316, December 2011. doi: 10.1007/s10686-011-9247-0.

[209] J. R. Mattox, D. L. Bertsch, J. Chiang, et al. The Likelihood Analysis of EGRET Data. *ApJ*, 461:396, April 1996. doi: 10.1086/177068.

[210] S. S. Wilks. The large-sample distribution of the likelihood ratio for testing composite hypotheses. *The Annals of Mathematical Statistics*, 9(1):60–62, 1938. ISSN 00034851. URL `http://www.jstor.org/stable/2957648`.

[211] L. Lista, editor. *Statistical Methods for Data Analysis in Particle Physics*, volume 909 of *Lecture Notes in Physics, Berlin Springer Verlag*, 2016. doi: 10.1007/978-3-319-20176-4.

[212] S. Ohm, C. van Eldik, and K. Egberts. γ/hadron separation in very-high-energy γ-ray astronomy using a multivariate analysis method. *Astroparticle Physics*, 31: 383–391, June 2009. doi: 10.1016/j.astropartphys.2009.04.001.

[213] T.-P. Li and Y.-Q. Ma. Analysis methods for results in gamma-ray astronomy. *ApJ*, 272:317–324, September 1983. doi: 10.1086/161295.